Heat and moisture in wooden bearings of monumental buildings

Spierenburg, M.

Award date:
2017

Technische Universiteit
Eindhoven
University of Technology

Heat and moisture in wooden bearings of monumental buildings

Name: Menno Spierenburg
Studentnr.: 0870790
Date: 30-01-2017

Faculty of Architecture, Building and Planning (ABP);
Master Building, Physics and Services (BPS).

Colofon

Document information

Document title:	Graduation project (M3 & M4)
Project title:	Heat and moisture in wooden bearings of monumental buildings
Date:	January 30, 2017

Personal information

Name:	Menno Spierenburg
Mail:	M.spierenburg@student.tue.nl
Studentnr.:	0870790
Master:	Faculty of Architecture, Building and Planning (ABP); Master Building, Physics and Services (BPS).

Graduation committee

Chairman:	dr. ir. H.L. Schellen
Extra supervisors:	dr. ir. A.W.M. van Schijndel ir. R.P. Kramer

Involved organisations

Organisation 1:	University of Technology, Eindhoven

Preface

At the beginning of my graduation project I would like to give my thanks to everyone who helped me and contributed in any way during this challenging journey.

I want to thank my supervisors dr. ir. H.L. Schellen, dr. ir. A.W.M. van Schijndel and ir. R.P. Kramer for giving me the chance to work at this interesting subject. Completing this thesis was a lonely road I needed to take. But as the end neared I was glad to receive your input. After that I knew I was heading in the right direction, which was exactly the inspiration I needed to finish my graduation.

A special thanks goes to Liselotte Apon, my collegue and supervisor at DPA Cauberg-Huygen. You were there at the most lonely part of the road. And while it was pitch dark, you let me see the light at the end of the tunnel. Thanks to your input I got back to the essence of my research.

And I want to give a very special thanks to my parents. Though you couldn't help me with the research and the writing itself, you both were always there to support me. Without judging you listened when I needed it and you gave me all the personal care and space to finish my study career.

Menno Spierenburg, January 2017.

Abstract

Currently insulation has been applied to many buildings. This proves to be a challenge for monumental buildings. When insulation needs to be applied at the interior side of a building, thermal bridges are inevitable. Wooden beam ends beared in the external wall are an example of such a thermal bridge. Adding interior insulation introduces a risk at mould growth and can even lead to deterioration of wood.

In this area several studies, including measurement studies, have already been performed. With the use of simulation models, the risk at deterioration of wooden beams can be analysed in another way. A simulation model made with COMSOL multiphysics that uses the Logarithmic capillary pressure (Lp_c) as moisture potential has already been developed.
In this study the COMSOL model is validated in 1D with Delphin, software that has already been used for simulating similar situations.

A case study from Denmark, that included measurements of a wooden beam end beared into a massive masonry wall, has been used for 2D validation. Therafter different variants are simulated. The variants can be separated into three categories: Indoor climate, insulation type and construction type. For each of these variants the influence at the moisture content inside the wooden beam has been mapped. Also the risk at mould growth and deterioration has been analysed.

Table of contents

Nomenclature

α = adapted wind driven rain coefficient [s/m]
β = thermal expansion coefficient of air = $3.43 \cdot 10^{-3}$ [1/K]
β_e = surface moisture transfer coefficient [kg/m²·s·Pa]
β_i = surface moisture transfer coefficient [kg/m²·s·Pa]
β_a = surface air transfer coefficient [kg/m² ·s·Pa]
δ_p = vapour permeability of material [kg/s·m·Pa]
δ_a = vapour permeability of air [kg/s·m·Pa]
ε = open porosity [-]
ε_s = emissivity exterior surface [-]
ε_{sky} = emissivity sky [-]
ε_g = emissivity ground [-]
η_a = dynamic viscosity of air [kg/m·s]
η_0 = reference value [kg/m·s]
θ = angle between the wind direction and the normal to the wall [°]
θ_v = vertical difference between horizontal plane and examined surface [°]
θ_h = horizontal difference between wind direction and line normal to surface [°]
μ = vapor diffusion resistance factor [-]
μ_{dry} = single dry-cup value of vapor diffusion resistance factor [-]
ψ = Kirchoff's potential [-]

q = thermal flux [J/m²]
g_l = mass flux of liquid water [kg/m²·s]
j_w = water flux (analog to g_{liq}) [kg/m²·s]
g_v = mass flux of vapour (contains both diffusion and advection) [kg/m²·s]
j_v = vapour flux (analog to g_{diff} (diffusion) and g_{adv} (advection)) [kg/m²·s]
j_a = air flux (analog to ($\rho_a \cdot r_a$)) [kg/m²·s]
g_e = flow density [kg/m²·s]

h_v = enthalphy of vapour (analog to the latent and sensible heat carried by moisture) [-]
h_w = enthalphy of liquid water (analog to the latent and sensible heat carried by moisture) [-]

S_h = source term for energy [J/m²]
S_w = source term for moisture [kg/m³·s]

M_v = Molar mass of water vapour [kg/mol]
M_w = Molar mass of water [kg/mol]
M_a = Molar mass of air [kg/mol]

ρ_0 = specific density [kg/m³]
ρ_a = density of dry air [kg/m³]
ρ_v = density of water vapour [kg/m³]
ρ_w = density of the liquid phase (water) [kg/m³]
$\rho_{v,e}$ = density of water vapour outdoor [kg/m³]
$\rho_{v,s}$ = density of water vapour at surface [kg/m³]

p_v = water vapour pressure [Pa]
p_c = capillary pressure [Pa]
p_{sat} = saturation pressure [Pa]
$p_{v,s}$ = water vapour pressure at surface [Pa]
$p_{v,e}$ = water vapour pressure of outdoor air [Pa]
p_0 = standard ambient pressure [Pa]
p_a = ambient air pressure [Pa]
$p_{a,e}$ = air pressure of outdoor air [Pa]
$p_{a,i}$ = air pressure of indoor air [Pa]
$p_{a,s}$ = air pressure at surface [Pa]

ΔP = air pressure difference [Pa]

σ = surface tension [J/m^2]

c_0 = specific heat capacity material [J/(kg·K)]
c_l = specific heat capacity of liquid water [J/(kg·K)]
$c_{p,a}$ = specific heat of dry air [J/kg·K]
$c_{p,l}$ = specific heat of liquid water [J/kg·K]
$c_{p,a+v}$ = specific heat of air and water vapour [J/kg·K]

w = moisture content [kg/m^3]
T = absolute temperature [K]
T_0 = reference temperature [K]
T_{eq} = equivalent outdoor temperature [K]
(combines air temperature, solar radiation and long wave radiation).
T_s = temperature of outdoor surface [K]
T_e = temperature of outdoor air [K]
T_{sky} = sky temperature [K]
T_i = indoor temperature [K]
T_{surr} = Temperature of surrounding surfaces [K]

h_i = heat transfer coefficient indoor [W/m^2·K]
h_e = heat transfer coefficient outdoor [W/m^2·K]
$h_{c,i}$ = convective heat transfer coefficient [W/m^2·K]
$h_{r,e}$ = radiative heat transfer coefficient [W/m^2·K]

D_v = vapour diffusion coefficient in air [m^2/s]
k_l = liquid permeability of the material [s]
k_a = air permeability of the material [kg/m·s·Pa]

R_v = gas constant for water vapour [J/kg·K]
R = rain at surface [kg/m^2·s]
R_{hour} = hourly rainfall total [mm]
R_h = rain through a horizontal plane [kg/m^2·s]
R_{wdr} = wind-driven rain [kg/m^2·s]

$R_{s,e}$ = surface resistance [m^2·K/W]
λ = thermal conductivity [W/(m·K)]
L_v = enthalpy of evaporation/condensation (latent heat) [J/kg]
r_a = air flow rate [m/s]
σ = Stefan-Bolzmann constant [W/m^2·K]
r = radius [m]
V_{loc} = local wind velocity at 0.3 m distance from the building wall external surface [m/s]
κ = wind driven rain coefficient [s/m]
U_{10} = reference hourly mean wind speed [m/s]
N = years of measurement [years]
m_a = Map airfield index [-]
m_s = Map spell index [-]
C_r = roughness coefficient [-]
C_t = topography coefficient [-]
O = obstruction factor [-]
W = wall factor [-]
n = vector normal to surface
g = acceleration due to gravity = 9.81 [m/s^2]
S = effective temperature (Sutherland constant) [K]
I_g = global solar irradiation [W/m^2]
α_{sol} = solar absorptance surface [-]
I_{lw} = long wave irradiation [W/m^2]
h = height of the building [m]

1 Introduction

Applying thermal insulation to building envelopes is common for new built buildings. Old buildings built in the Netherlands before 1950, however, are most certainly not applied with thermal insulation. This also holds for monumental buildings in the Netherlands.
There is a risk of permanently damaging a monumental building when applying thermal insulation in a wrong way. Therefore studies are performed to see whether thermal insulation can be applied without damaging the building [Gnoth, S. 2005][Holle, H.J. 2009][Stopp, H. 2010][Strangfeld, et al., 2011][Grobbauer & Ruisinger, 2012][Kehl, D. 2012][Morelli & Svendsen, 2012][Guizzardi, M. 2015a].
[Kehl, D. 2013] describe that it's expected that the connection of wooden beams to stone walls is critical. A high moisture content is expected, certainly when insulation is applied at the interior. The results show that this detail isn't critical for buildings with external walls that have a repellant plaster or coating. For bare brick walls, however, this is indeed a critical detail.
In the Netherlands bare brick walls are common. The connection of wooden beams to stone walls are present in most monumental buildings. Wooden beams are part of the contruction, either as part of the floor or as part of the roof construction. It is only after 1921 that concrete is being used as replacement for wood in the construction of floors and roof constructions and only on a small scale.
The hygrothermal behaviour of these details can be analysed experimentaly by measuring an existing situation. However, it's also possible to use simulation software to predict the hygrothermal behaviour [Janetti, Ochs & Feist, 2011].
In the simulation software a coupling of moisture and heat is made. The moisture part can be simulated with different potentials: p_c (capillary pressure), RH (relative humidity), w (water content) and Lp_c (Logarithmic capillary pressure). Each of the potentials has its own advantages and disadvantages. [Portal, N.W, 2011]describe Lp_c is the most suitable method for extreme situations at the boundaries. Due to this paper, modeling with Lp_c as moisture potential continued [Uittenbosch, S. 2012].
In a comparison study between moisture potentials [Janssen, H. 2014] it is shown that Lp_c has worse results for near-saturation conditions, when compared to p_c and RH.

2 Objectives

2.1 Research aim

The goal of this research is to calculate the heat and moisture development at the wooden beam end within a monumental building. In the first place this will provide more knowledge about that specific detail. Eventually that may contribute into preserving wooden beams of monumental buildings in the future. Second, the calculation itself may be of great scientific value. The calculations will be made in a state of the art simulation model. By adding more detail to this model, and by making use of different simulation software, more sophisticated models can be developed for future use.

2.2 Research questions

How can wooden beam ends be preserved with the use of HAM simulations, while insulating a monumental building?
- When will deterioration of wood take place?
- What is the experience from earlier renovations?
- In which way is insulating possible without causing deterioration of wooden beam ends?

- What are the differences between moisture potentials?
- How accurate is a COMSOL model using Logarithmic capillary pressure as moisture potential?
- What are the possible improvements for this COMSOL model?

3 Methodology

3.1 Literature study

The starting point of the research is a literature study. With the literature study knowledge from former research is gained. However, mapping the physical phenomena that occur or influence the research is also important. With that the limitation of other research can be determined and own research can be made as complete as possible.
The literature study can be seperated in two parts. The first part is about the physical phenomena, while the second part contains former research. The physichal phenomena will be searched in both Dutch and English. The former research will be searched in Dutch, English and German. Dutch is the native language of the researcher. Including the Dutch language creates the ability to include former research of the TU Eindhoven, which is written in Dutch. It is expected that similar research is performed in Germany, therefore German literature is also included to the search.

3.2 Simulations

The first simulations are made to control if the model is build in a right way. At first modeling will be completed in COMSOL multiphysics, using the model setup by Uittenbosch, S. [2012] according the step-by-step guidance written by Goesten, S. [2016].
These models will also be made in Delphin 5.8.3. This software is especially developed to solve coupled Heat, Air and Moisture (HAM) transport models. In multiple studies Delphin has been used as simulating software. Delphin makes use of a different moisture potential than the COMSOL models chosen by Uittenbosch S. [2012].
It is to be discovered if the moisture potential causes large differences and if there are other differences noticable between COMSOL and Delphin.
When modeling is familiar to the researcher, more advanced simulations are made containing 2D details of the connection between wooden beams and exterior walls. Multiple models compared with existing situations are simulated.

Table 3.1 Keywords used in the literature review

English	Dutch	German
Wooden beam ends	Houten balkoplegging/ Balkkoppen	Holzbalkenkopf
Moisture	Vocht	Feuchte
Comsol - Delphin	-	-
Deterioration	Houtrot	Fäule
Wooden beams	Houten balken	Holzbalken
-	-	Holzbalkendecke
Internal insulation	Inwendige isolatie	Innendämmung
Logarithmic capillary pressure	-	-
Moisture potential	-	-
Hysteresis	-	-
Adsorption/desorption	-	-
Wind-driven-rain	-	-

4 HAM aspects wood

4.1 Application of wood in buildings

In the built environment wood has many uses. It is often used as cladding, both for indoor and outdoor use. Used as part of the building envelope, for instance as window frame or roof decking. And it's used as part of the supportive structure, for instance as foundation poles, floor beams, columns and rafters.

Bonnema, T.J. [1960] describes the use of wooden beams in buildings and their funtionality:
- Wooden beams act as horizontal separation between spaces;
- Forces are led through the beams towards their bearing which is usually a vertical wall;
- Beams are coupled to the walls and reduce the buckling length of the walls.

Spruce, fir and oak are three commonly used wood types in the built environment [Bonnema, T.J. 1960].

Wood that has direct contact to the outdoor environment is often protected with a coating, like paint. The coating protects the wood against moisture. However, wood used in the structure of a building is often unprotected.
Most critical part for this unprotected wood is where materials meet and a transition between indoor climate and outdoor climate occurs. For wooden beams this critical part is positioned at the bearings. In order to transfer the forces to the rest of the structure, wooden beams are always supported by other materials. Some of these materials are wood and metal, but in the Netherlands a connection to stone is common (see figure 4.1). There the wooden beam ends are in contact with the vertical wall.

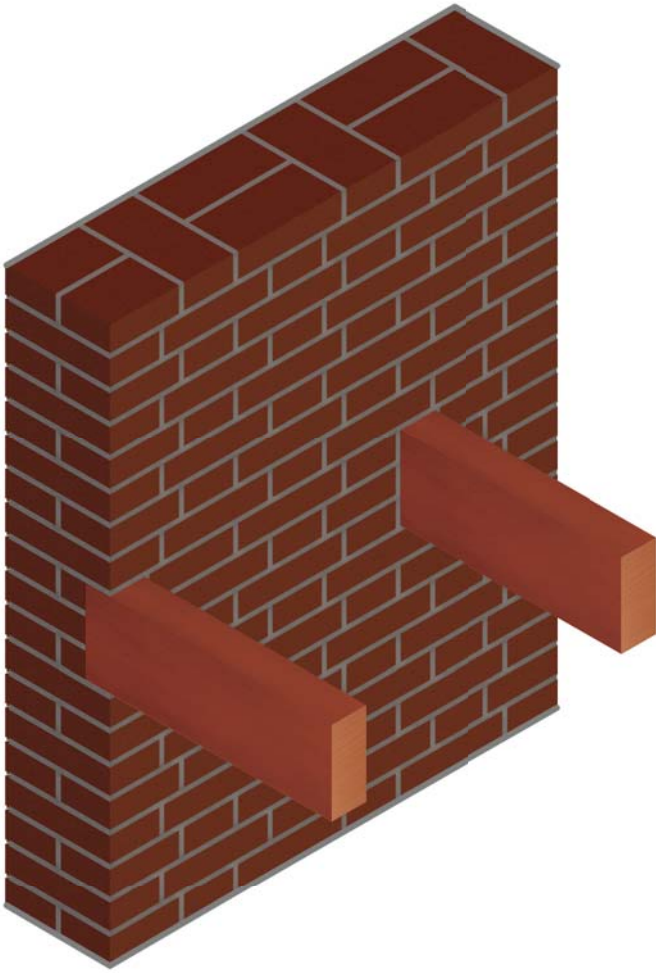

Figure 4.1 Isometric projection of a masonry wall with wooden beams supported by the wall.

4.1.1 Original contruction

In old buildings - with massive walls - the wall has direct contact with both the indoor and outdoor environment. Moisture penetration throught these massive walls is a well known phenomena that can lead to uncomfortable or even unhealthy situations at the interoir side of the wall.

The situation of figure 4.1 can lead to desintegration of wood. A practical example of this situation is visible in figure 4.2, where the wooden beam end desintegrated. Only the part that isn't connected to the wall remained.
In order to prevent this from happening, different measures could be taken. Using primer to protect the beam ends is a common solution. Other

Figure 4.2 Wooden beam end (bottom) as part of the internal construction (top) of a church in Beusichem. The end desintegrated and isn't connected to the wall anymore.

measures are the addition of an air cavity, placement of hardwood or a hardstone material underneath the beam ends. Or connecting the beam to the outdoor environment while protecting it from the rain [Cestari, C.B. 2001][Nespoli, L. 2013a][Janetti, M.B. 2012].

Figure 4.3 shows a few possible connections of wooden beam ends to masonry. The top left is a common construction in the Netherlands for old buildings. The most recent buildings that still have wooden beams, are built with a cavity wall which is visualized in the bottom right. The cavity prevents moisture from penetrating the whole structure.
In monumental buildings a cavity wall is uncommon and one of the other possibilities are more likely to occur.

Not in all monumental buildings a situation is present like the one in figure 4.2. This situation mostly prevails when there is a leakage, or when there is a high moisture load due to wind-driven rain whether or not combined with a low evaporation rate, i.e. when the wall is positioned at the north [Guizzardi, M. 2015a].
In all other situations where the wooden beam ends are still in good condition, it is to be expected that the beam ends will remain that way.
Only when the hygric properties of the wall are changed, a critical situation in terms of moisture loads can occur.

4.1.2 Insulated construction

Recently many building envelopes receive an additional insulation layer. The added insulation decreases the thermal conductivity of the structure and reduces energy losses.
Logically this also has an effect at the hygric properties of the wall.

The position of the insulation layer is crucial to determine if a construction remains safe. Within the insulation layer a temperature step between the interior and exterior exists. Applying the insulation at the exterior is the best solution. The whole construction is then exposed to the indoor climate and protected against moisture entering from the outside.
For most monumental buildings it is not possible to apply insulation at the exterior. In case of a massive wall, when no cavity is present, insulation at the interior is the remaining option.
Insulating at the inside introduces moisture risks. Main contributor of the moisture risk is the convective flux. Small cracks or joints between the

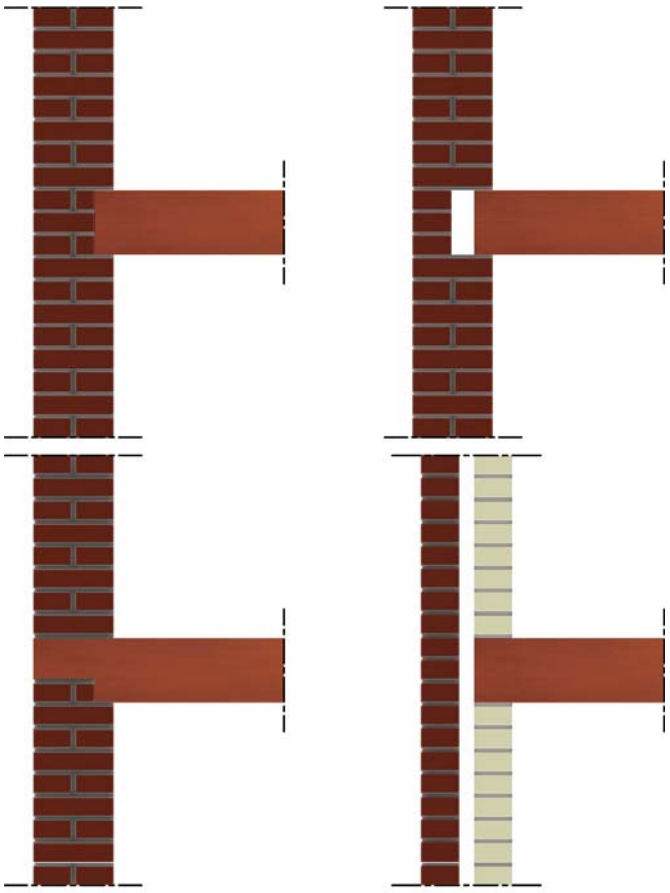

Figure 4.3 Connection of wood to masonry. With a standard situation (top left), with a cavity (top right), connected to the outdoor environment (bottom left), completely seperated from the outdoor environment with a cavity wall (bottom right).

insulation material or insulation that has been badly applied to the wall can cause these convective fluxes [Borsch-Laaks, R. 2006][Borsch-Laaks, R. 2009][Borsch-Laaks, R. 2010].
A solution to this problem is to apply a vapour barrier - thin foil - at the inside. Borsch-Laaks [2009] also proposes internal insulation with a double layer of OSB and plasterboard (without vapour barrier). The connection to the wooden beam is critical in this case. Since an opening at the connection between the insulation and the wooden beam can cause warm humid air to enter the structure and condensate at the surface.

Another solution to reduce the moisture risk is to enlarge the thermal bridge with a gap of 200mm around the wooden beam [Morelli, M. 2010]. Also active heating near the wooden beam or passive heating with a conductive rod inside the beam - the rod heats up due to it's connection to the interior - prove to be viable solutions [Gnoth, et al. 2005].

While there are several solutions to reduce the risk, the chance at deterioration isn't excluded. Since this depends at many factors like the climate and the construction.

4.2 Properties wood

As mentioned before, different types of wood are used in the build environment. Each wood type has different properties regarding strength, weigth, moisture content and insulation.

4.2.1 The moisture content

One of the important properties in HAM simulations is the moisture content. For various porous materials - wood is such a material - it is known that the moisture content inside the material is related to the surrounding climate.
In figure 4.4 the moisture content inside a porous material is visualized. Relative humidity is the dependant variable in this figure. However, also temperature has influence at the moisture content inside the material.

In a hypothetic situation where the climate is assumed stable, the moisture content reaches an equilibrium. Which is convenient for measurements and the determination of the material properties, since stable conditions can be created inside a climate chamber and using salts respectively [Bratasz, L. 2011]. In reality this equilibrium state won't be achieved, due to the constantly changing environment.

With an equal temperature and relative humidity, this equilibrium moisture content (EMC) still can differ depending on the history of the moisture content.
There is a difference in EMC between desorption (drying) and adsorption (moistening). In figure 4.5 the desorption and adsorption curve are visualised. The desorption curve is obtained by measuring the drying process starting at fully saturated condition. The adsorption curve is obtained by measuring the moistening process starting at completely dry condition.
In the building practice a completely dry condition and fully saturated condition won't be present, since these conditions are acquired mechanically. Therefore the real EMC will remain between the adsorption and desorption curve [Engelund, E.T. 2011].
The difference between drying and wetting is called 'hysteresis'. The existence of this phenomena has been proved by many authors. However, the explanation about hysteresis and how it occurs is not consistent [Engelund, E.T. 2013].

A frequent used explanation for hysteresis is the 'ink bottle' effect together with the 'raindroplet' effect (see figure 4.6).

The essence of both effects is that the nano pores (the pores smaller than the characteristic pores) and the boundaries of the cell walls form a resistance. This results in a local equilibrium state that differs depending at the history of the moisture.

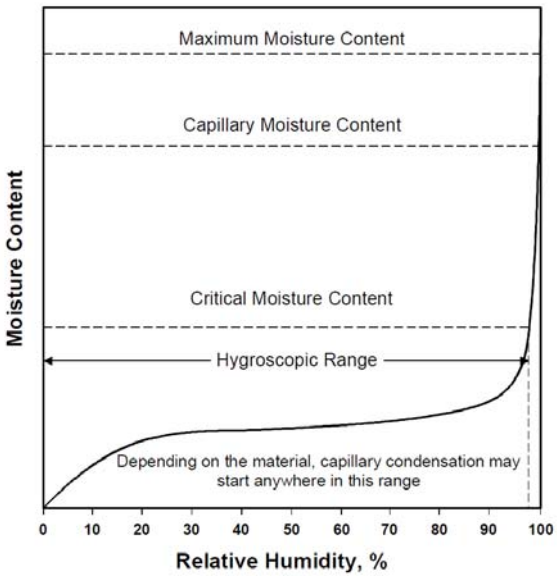

Figure 4.4 The moisture content for a porous material following the sorption isotherm [Vinha, J. 2007].

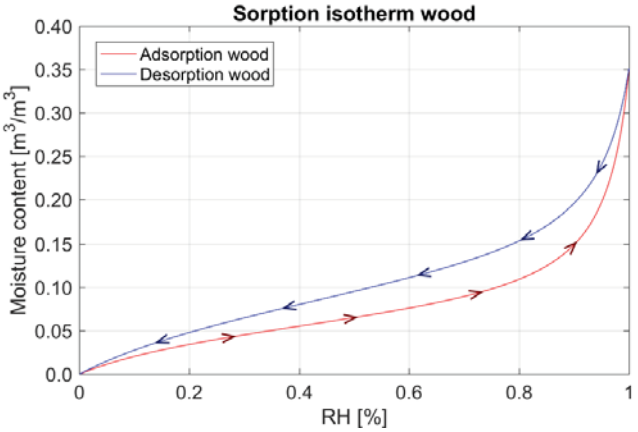

Figure 4.5 The adsorption (red) and desorption (blue) curve of a wooden material. The real equilibrium moisture content (EMC) will be between these curves.

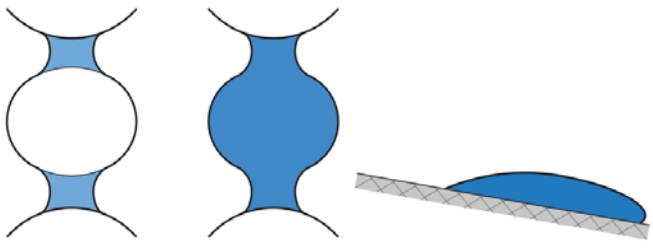

Figure 4.6 The equilibrium moisture content is different for adsorption (left) and desorption (middle) here explained with the ink-bottle effect and the raindroplet effect (right).

4.2.2 Deformation of wood

Wood can be deformed in various ways. In this part only deformation related to moisture is described. Moisture itself doesn't cause damage to wood. Rotting causes the wood to degrade and it's the wood destroying fungi that eventually uses the wood as a nutrient. When the decay continues, wood loses it's mass and with that also it's strength. Different rot types - brown rot, white rot and soft rot - can occur.

Not al fungi are able to cause decay of wood, but they do prepare paths for the wood destroying fungi.

4.2.3 Safety threshold moisture in wood

Moisture needs to be present in order for the wood destroying fungi to grow. In literature different thresholds are mentioned. Thresholds for the wood to be safe and thresholds that determine if mould growth is possible.

There's a commonly used static treshold with a moisture content of 20% for the wood to be safe [Guizzardi, 2015b].
Both Guizzardi [2015b] and Kehl, D. [2013] mention that the static threshold of 20% is not always suitable to determine if mould growth occurs. Due to unhomogeneous distribtution of the moisture in wood, also at a lower moisture content fungi can grow.

Adan and Samson [2011], describe that the risk of fungal growth increases when the moisture content is above saturation point and in the order of 25-30%.
Viitanen H. et al. [2010b] confirms 25-30% moisture content is the ideal condition for decay fungi.
Viitanen H. et al. [2010a] and Adan and Samson [2011] both describe that local mould growth might already prevail before the mentioned threshold.
Guizzardi, [2015b] mentions that localized fungi may prevail at a moisture content of 20-27%.

Relative humidity values of 80-95% (depending at temperature) are required for mould growth.

To reach a moisture content between 25-30%, a high relative humidity between 95-99% is required. And these humidity levels must be maintained for weeks to several months depending at the temperature.

Viitanen performed measurements and concluded that when temperatures are ≥0°C and relative humidity is ≥95% decay is possible.

5 Heat, Air and Moisture (HAM) transport

In [Goesten, S. 2016] three transport mechanisms, Heat, Air and Moisture (HAM), are elucidated. Most equations origin from [Uittenbosch, S. 2012] where a start has been made with creating the HAM model. Both describe basic balance equations and more extensively the logarithmic capillary pressure (Lp_c) as moisture potential.
[Goesten, S. 2016] describes that his model still has room for improvement. To achieve this improvement, the equations from [Uittenbosch, S. 2012] and [Goesten, S. 2016] are compared to equations mentioned in the literature. Assumptions or simplifications that significantly affect the outcome of the model can be found through this comparison.

In this chapter the HAM equations are devided in three parts; Heat, Moisture (where the convective transfer is included) and Air.
- Chapter 5.1 describes the balance equations, which is the starting point for all the equations;
- Chapter 5.2 describes the moisture equations from literature, with 5.2.1 and 5.2.2 the moisture fluxes inside a material and 5.2.3 and 5.2.4 the moisture boundary conditions;
- Chapter 5.3 describes the heat equations from literature, with 5.3.1 and 5.3.2 the heat fluxes inside a material and 5.3.3 and 5.3.4 the heat boundary conditions;
- Chapter 5.4 describes the air transfer equations from literature, with 5.4.1 the air fluxes inside a material and 5.4.2 the air boundary conditions.
- Chapter 5.5 describes the applied potentials, and the equations applied in the software used.

In this research different software is used to perform simulations with: COMSOL Multiphysics 5.0 (COMSOL) and Delphin 5.8 (Delphin). In Delphin the vapour pressure (p_v) and capillary pressure (p_c) are used as driving moisture potential. For the COMSOL the work of [Goesten, S. 2016] is continued and therefore the logarithmic capillary pressure (Lp_c) is used as driving moisture potential.

5.1 Balance equations

The HAM transport mechanisms can be described through a set of equations. They originate from the basic principle that there is a balance in energy and in moisture. One form of the balance equations as depicted by Janetti, M.B. [2016]:

$$\frac{\partial H}{\partial t} = -\nabla \cdot \left(q + h_v j_v + h_w j_w \right) + S_h$$
$$\frac{\partial u}{\partial t} = -\nabla \cdot \left(j_w + j_v \right) + S_w \qquad (1.1)$$
$$\frac{\partial \rho_a}{\partial t} = -\nabla \cdot \left(j_a \right)$$

Depending on the source, the balance equations can have different appearances. Another form is depicted by Belleudy, C. [2015]:

$$\frac{\partial E}{\partial t} = -\nabla \cdot \left(q_{cond} + q_{conv} + q_{moist} \right)$$
$$\frac{\partial w}{\partial t} = -\nabla \cdot \left(g_{diff} + g_{adv} + g_{liq} \right) \qquad (1.2)$$
$$\varepsilon \frac{\partial \rho_a}{\partial t} = -\nabla \cdot \left(\rho_a \cdot r_a \right)$$

q = thermal flux [J/m^2]
h_v = enthalphy of vapour [-] analog to the latent and sensible heat carried by moisture
j_v = vapour flux [kg/m^2·s] analog to g_{diff} (diffusion) and g_{adv} (advection)
h_w = enthalphy of liquid water [-] analog to the latent and sensible heat carried by moisture
j_w = water flux [kg/m^2·s] analog to g_{liq}
j_a = air flux [kg/m^2·s] analog to ($\rho_a \cdot r_a$)
ε = open porosity [-]
S_h = source term for energy [J/m^2]
S_w = source term for moisture [kg/m^3·s]

The source terms for energy and moisture are left out of equation 1.2 [Janetti, M.B. 2016][Belleudy, C. 2015].

5.2 Moisture

As mentioned in the balance equations, moisture transfer consists of two physical phenomena, the flux of vapour and the flux of liquid water respectively. According to Belleudy, C. [2015] is it theoretically also possible to separate the moisture transfer into three parts, which is visible in equation 1.2. There the vapour flux is separated into moisture buildup inside the material and moisture present in air [Belleudy, C. 2015].
To compare the different formulas from the literature, the distinction between vapour and liquid has been made in the paragraph below [Berger, J. 2014] [Hagentoft, C.E. 2004]. In reality, however, it isn't possible to separate the moisture transport, since it's a combined process where strict boundaries between the different physical phenomena don't exist [Hagentoft, C.E. 2001].

The moisture part of equation 1.2 can be simplified into the following form [Berger, J. 2014][Hagentoft, C.E. 2004]:

$$\frac{\partial w}{\partial t} = -\nabla \cdot \left(g_v + g_l \right) \qquad (1.3)$$

w = moisture content [kg/m^3]
g_v = mass flux of vapour [kg/m^2·s] (contains both diffusion and advection)
g_l = mass flux of liquid water [kg/m^2·s]

5.2.1 Vapour flux

The vapour flux can be depicted with Fick's law [Berger, J. 2014][Hens, H.L.S.C. 2015][Portal, N.W. 2011]:

$$g_v = -\delta_p \left(w \right) \cdot \nabla p_v + r_a \cdot \nabla \rho_v \qquad (1.4)$$

δ_p = vapour permeability of material [kg/s·m·Pa]
w = moisture content [kg/m^3]
p_v = partial water vapour pressure [Pa]
r_a = air flow rate [m/s]
ρ_v = water vapour density [kg/m^3]

Vapour permeability

According to [Goesten, S. 2016] the vapour permeability of the material can be calculated with the vapour permeability of air (δ_a) and the vapour diffusion resistance factor (μ), which is material dependent:

$$\delta_p = \frac{\delta_a}{\mu} \qquad (1.5a)$$

δ_p = vapour permeability of the material [kg/s·m·Pa]
δ_a = vapour permeability of air [kg/s·m·Pa]
μ = vapour diffusion resistance factor [-]

[Hens, H.L.S.C. 2015] mentions that the calculated vapour diffusion with the equation above is a simplification of the reality. Influencing factors not shown in this equation are the moisture content and to some extent the temperature. Goesten, S. [2016] didn't expatiate on the vapour diffusion resistance factor, so the statement by [Hens, H.L.S.C. 2015] only holds when μ is assumed to be a single value [Wit, M. 2009].
[Janetti, M.B. 2016] emphasizes this, by stating that the water flux increases with increasing water content. In other words, the vapour diffusion resistance factor (μ) depends at the moisture flux.
[Hagentoft, C.E. 2002] and [Li, Q. 2009] describe an extensive formula to calculate the vapour diffusion:

$$\delta_p = \frac{\delta_a}{\mu_{dry}} \frac{1 - \frac{w}{w_{sat}}}{\left(1-\psi\right)\left(1-\frac{w}{w_{sat}}\right)^2 + \psi)} \qquad (1.5b)$$

μ_{dry} = single dry-cup value of vapour diffusion resistance factor [-]
ψ = Kirchoff's potential [-]

[Goesten, S. 2016] estimates the vapor permeability of air (δ_a) as a single value $1.8 \cdot 10^{-10}$ [s]. [Li, Q. 2009] includes a temperature dependency to estimate δ_a. However, [Renato, P. 2013] and [Börjesson, F. 2013] describe that δ_a can be calculated with the following formula:

$$\delta_a = \frac{D_v}{R_v T} \qquad (1.6)$$

D_v = vapour diffusion coefficient in air [m^2/s]
R_v = gas constant for water vapour [J/kg·K]
T = absolute temperature [K]

When equation 1.4-1.6 are combined, the following equation is obtained:

$$g_v = -\frac{1}{\mu} \frac{D_v}{R_v T} \cdot \nabla p_v + r_a \cdot \nabla \rho_v \qquad (1.7)$$

Here μ is a function depending at the moisture content as described in equation 1.5a & 1.5b.

Partial vapour pressure

The vapour pressure can be determined according Kelvin's law. This law describes the relation between vapour and liquid [Berger, J. 2014][Wit, M. 2009].

$$p_v = p_{sat} \cdot \exp\left(\frac{p_c}{\rho_w R_v T}\right) \quad (1.8)$$

p_{sat} = saturation pressure [Pa]
p_c = capillary pressure [Pa]
ρ_w = density of the liquid phase (water) [kg/m^3]
R_v = gas constant for water vapour [J/kg·K]

The vapor diffusion coefficient in air (D_v) can be calculated with an empirical function. Originally the function was created by Schirmer. Currently five different empirical functions are available in literature [Ochs, F. 2008][VDI Heat Atlas, 2012]. When the temperature remains < 50°C the results of these empirical functions don't show significant differences, therefore all functions can be applied in the build environment [Ochs, F. 2008].
Both [Renato, P. 2013] and [Börjessson, F. 2013] use the simplified function from Schirmer:

$$D_v = 2.31 \cdot 10^{-5} \frac{p_0}{p_a}\left(\frac{T}{273}\right)^{1,81} \quad (1.9)$$

p_0 = Standard ambient pressure [Pa]
p_a = Ambient air pressure [Pa]

[Janetti, M.B. 2011] describes that air pressure differences have negligible effect at the mass transfer. Some authors decided to use a single-value for D_v instead of an empirical function [Janetti, M.B. 2016][Goesten, S. 2016][Li, Q. 2009].

5.2.2 Liquid transport

Liquid transport needs a driving force. This force can either be capillary, gravitational or a difference in pressure. It is possible to determine the capillary force and the gravitational force with Darcy's law. The equation used by [Goesten, S. 2016] (equation 1.10a) originates from [Wit, M. 2009]. [Goesten, S. 2016] mentions that the use of this equation and especially the gravitational part lead to strange simulation results. [Tammes, E. & Vos, B, 1986], mentions that the gravitational force only applies to a situation with vertical suction. For instance calculating a rising front at a basement or wall that is in contact with groundwater.

$$g_l = -k_l(w) \cdot (\nabla p_c + \rho_w \cdot g \cdot z) \quad (1.10a)$$

If vertical suction is not present, the gravitational part can be left out of equation 1.10a. Then the following equation is obtained [Berger, J. 2014] [Delgado, J.M.P.Q. 2013][Hagentoft, C.E. 2004]:

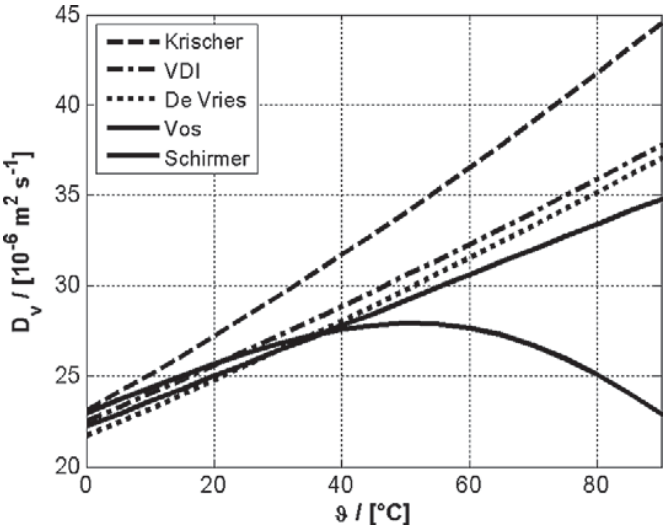

Figure 5.1 Vapor diffusion coefficient as a function of temperature according to different authors [Ochs, F. 2008].

$$g_l = -k_l(w) \cdot \nabla p_c \quad (1.10b)$$

k_l = liquid permeability [s]
w = moisture content [kg/m^3]
p_c = capillary pressure [Pa]

The capillary pressure can be determined using equation 1.8 in a rewritten form. However it is also possible to calculate the capillary pressure according the Young-Laplace's law [Berger, J. 2014]:

$$p_c = -\frac{2\sigma\cos\theta}{r} \quad (1.11)$$

θ = contact angle [°]
σ = surface tension [J/m^2]
r = radius [m]

5.2.3 External boundary conditions

Previous equations describe the behaviour of moisture inside porous materials. In some equations the influence of the environment outside the materials is more or less included. However, an equation solely describing transfer of moisture at the boundaries of the material hasn't been mentioned before. These boundary conditions are of great importance, since moisture entering and leaving the material determines the total amount of moisture inside the material.

The following equation is used to calculate the transfer of vapour [Vinha, J. 2007][Santos, G.H. 2009][Portal, N.W. 2011][Vereecken, E. 2015] [Delgado, J.M.P.Q. 2015]:

$$g_e = \beta_e(p_{v,e} - p_{v,s}) \quad (1.12a)$$

g_e = flow density [kg/m²·s]
β_e = surface moisture transfer coefficient [kg/m²·s·Pa]
$p_{v,s}$ = water vapour concentration air at surface [Pa]
$p_{v,e}$ = water vapour concentration in ambient air [Pa]

In equation 1.12a, the contribution of precipitation to the transfer of mass is left out. This parameter is mentioned by [Janssen, H. 2007] and [Li, Q. 2009], resulting in the following equation:

$$g_e = \beta_e \left(p_{v,e} - p_{v,s} \right) + R \qquad (1.12b)$$

R = rain at surface [kg/m²·s]

In equation 1.12b the air flux and the direction of the flux aren't included. When the air is entering the structure equation 1.12c applies. When the air is exiting the structure equation 1.12d applies [Hagentoft, C.E. 2004]:

$$g_e = \beta_e \left(p_{v,e} - p_{v,s} \right) + r_a \cdot \rho_v + R \qquad (1.12c)$$

$$g_e = \beta_e \left(p_{v,e} - p_{v,s} \right) + r_a \cdot \rho_{v,s} \qquad (1.12d)$$

r_a = air flow rate [m/s]
$\rho_{v,e}$ = density of water vapour outdoor [kg/m³]
$\rho_{v,s}$ = density of water vapour at surface [kg/m³]

The surface moisture transfer coefficient (β) is difficult to determine [Janssen, H. 2007]. Therefore it can be calculated according the Lewis analogy, which describes the relation between the heat and moisture transfer coefficient [Janssen, H. 2007][Li, Q, 2009][Vereecken, E. 2015][Goesten, S. 2016]:

$$\beta_e = 7.7 \cdot 10^{-9} \cdot h_{c,e} \qquad (1.13)$$

$h_{c,e}$ = convective heat transfer coefficient [W/m²·K]

According to Vereecken, E. [2015] the convective heat transfer $h_{c,e}$ is a variable depending at the air velocity. And therefore strong related to the effect of wind driven rain. In chapter 5.3.4 the convective heat transfer will be elaborated.

At chapter 5.3.3 the calculation of the air flow rate (r_a) will be further elaborated.

To calculate the humidity by volume (ρ_v) or the mass fraction of water in air, the ratio between molar masses of water vapour, water and air should be calculated first [Janetti, M.B. 2016]:

$$X = \frac{M_v + M_w}{M_a} \qquad (1.14a)$$

$$X_v = \frac{M_v}{M_a} \qquad (1.14b)$$

M_v = Molar mass of water vapour [kg/mol]
M_w = Molar mass of water [kg/mol]
M_a = Molar mass of air [kg/mol]

Equation 1.14a is used when liquid water is present. Equation 1.14b can be used in the hygroscopic range, where liquid water is absent.

The ratio of the molar masses are combined with the ratio of water vapour and air pressure resulting in the following equation [Janetti, M.B. 2016]:

$$\rho_v = \frac{M_v}{M_a} \cdot \frac{p_v}{p_a} \qquad (1.15)$$

With M_v = 0.018; M_a = 0.029 and the p_a at 20°C with an absolute pressure of 1 atm = 101325. Equation 1.15 results in the following [Wit, M. 2009][Janetti, M.B. 2016]:

$$\rho_v = \frac{0.018}{0.029} \cdot \frac{p_v}{101325} = 0.6125 \cdot 10^{-5} \cdot p_v$$

The precipation at a surface (R) depends of two components. The amount of rain coming down at a horizontal surface and the amount of rain that experiences a horizontal displacement caused by wind [Janssen, H. 2007]:

$$R = R_h \cdot \cos\left(\theta_v\right) + R_{wdr} \qquad (1.16)$$

R_h = rain through a horizontal plane [kg/m²·s]
R_{wdr} = wind-driven rain [kg/m²·s]
θ_v = vertical difference between horizontal plane and examined surface [°]

Data about the rain through a horizontal plane can be obtained from measurements at different meteorological stations.
In The Netherlands daily precipitation measurements are performed at 325 locations [KNMI, 2000]. These measurements form a fine grid that provides information about the local differences. Local differences can be significant as can be seen in figure 4.1. However, to calculate the wind driven rain, the daily interval is too course. Preferably this data is only used if accurate data isn't available [Rhydock, J.P. 2005].
In order to calculate the wind driven rain, hourly data is needed [Ge, H., et al. 2009][Blocken, et al. 2004]. It is even preferred to use measurement data with a 10-minute interval, however these measurements aren't widely available [Blocken, et al. 2007].

The royal Dutch meteorological institute (KNMI) provides hourly data from 35 weather stations (of which 32 stations measure both wind and precipitation). These stations are distributed in such a way, that values of wind speed can be calculated for the whole country through interpolation with an error margin of 10% [KNMI, 2000]. The position of the 32 weather stations is visualized in figure 5.2.

[Goesten, S. 2016] uses the following formula from [Blocken, et al. 2004] to calculate the wind driven rain:

$$R_{wdr} = \kappa \cdot U \cdot R_h \approx \kappa \cdot U \cdot R_h \qquad (1.17)$$

κ = wind driven rain coefficient [s/m]

For the equation 1.17, Blocken, et al. [2004] mentions that a value of 0.222 is a frequently used average for the WDR coefficient (κ), based at empirical relationships.
Wind driven rain depends at the local situation [Blocken, et al. 2004]. Surrounding buildings can influence the wind driven rain, but also less rigid objects like trees are causing an obstruction [Blocken, B. and Carmeliet, J. 2005].
It should be noted that equation 1.17 is only applicable for free field conditions, due to the local environment that isn't specified within the equation.

The following equation does take local phenomena into account [Blocken, et al. 2004][Janssen, H. 2007]:

$$R_{wdr} = \alpha \cdot U \cdot R_h \cos(\theta_h) \qquad (1.18)$$

α = adapted wind driven rain coefficient [s/m]
θ_h = Horizontal difference between wind direction and line normal to surface [°]

In the parameter α all local phenomena are represented. Computational Fluid Dynamics (CFD) is needed in order to determine the value for α. With CFD the windflow patterns around the building are calculated, raindrop trajectories are added to this model and eventually catch ratios are obtained for different raindrop sizes. The catch ratios are combined in a spectrum. Using the spectrum, wind driven rain can be calculated for rain events with different heaviness [Blocken, et al. 2004].
The CFD calculation method is constantly being optimized. Currently state-of-the-art models make use of an Eulerian multiphase model (EM). Models using EM replace the extensive work of calculating the raindrop trajectories for each droplet and size. Which allows the model to be combined with transient calculations of the wind pattern. As a result even turbulent situations can be calculated [Kubilay, et al. 2013].
CFD calculations are beyond the limits of this research. There are semi-emperical methods which will be used to give an indication of the precipitation.

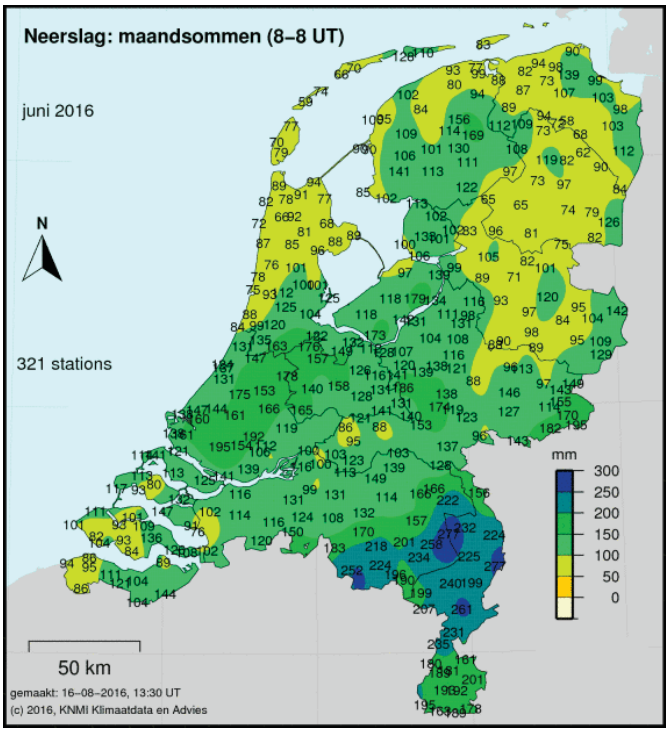

Figure 5.2 Precipitation in June 2016 measured at local weather stations of the KNMI [KNMI, 2016].

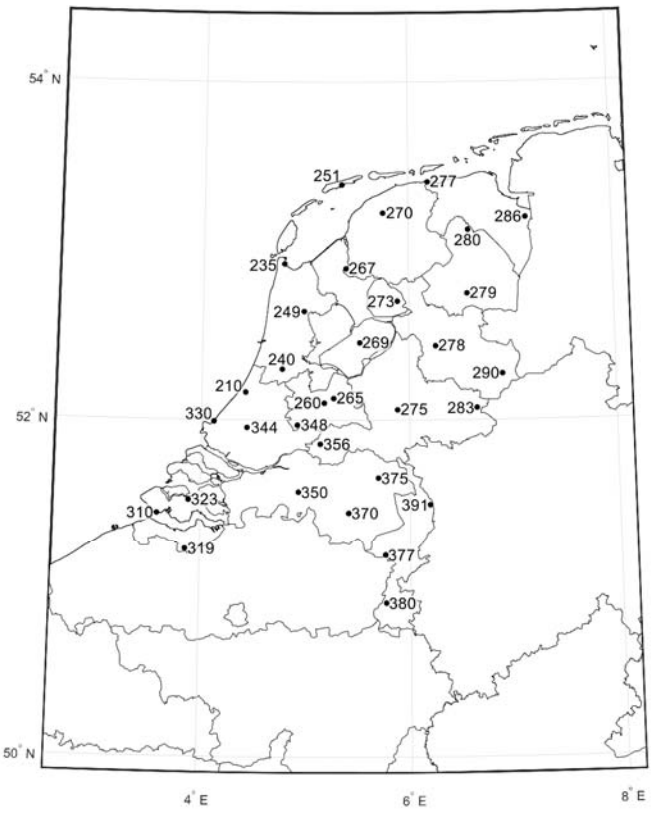

Figure 5.3 Position of the 32 weatherstations where both wind and precipitation measurements are performed. The numbers for each station are determined by the KNMI.

In the EN-ISO 15927-3:2009 a method is described to estimate wind-driven rain based at meteorological measurements (calculations from this standard are similar to those mentioned in the NEN 13013-3:1997). The airfield annual index (I_a) describes the annual precipation at a wall in l/m^2 (equation 1.19). The airfield spell index (I_s) is used to determine the worst spell that occurs within a 3 year timeframe (equation 1.20) [Blocken et al. 2010][NEN 13013-3:1997]:

$$I_a = \frac{2}{9}\frac{\sum U_{10} \cdot R_{hour}^{\frac{8}{9}} \cdot \cos\theta}{N} \quad (1.19)$$

$$I_s = \frac{2}{9}\sum U_{10} \cdot R_{hour}^{\frac{8}{9}} \cdot \cos\theta \quad (1.20)$$

U_{10} = reference hourly mean wind speed [m/s]
R_{hour} = hourly rainfall total [mm]
N = years of measurement [years]
θ = angle between the wind direction and the normal to the wall [°]

[Smith, et. al. 2012] leaves cos θ out of equation 1.19 and 1.20. With that the wind driven rain is calculated for a surface that is always perpendicular to the wind. On one hand Smith, et al. [2012] uses this adaption to calculate the worst case scenario. In this worst case, future changes in wind direction are taken into account. On the other hand Smith, et al. [2012] also says the following based at [Blocken and Carmeliet, 2006]: "*the cosine projection had a propensity to overestimate the catch ratio*". In other words, the cosine projection decreases the accuracy of the results.
I_a and I_s can be transformed to map values to improve the readability. With the following equations [NEN 13013-3:1997]:

$$m_a = 6 + 19.93 \cdot \log 10\left(\frac{I_a}{200}\right) \quad (1.21)$$

$$m_s = 10 + 19.93 \cdot \log 10\left(\frac{I_s}{20}\right) \quad (1.22)$$

m_a = Map airfield index [-]
m_s = Map spell index [-]

Figure 5.4 shows the airfield anual index with the adaption of Smith et al. [2012] for The Netherlands. The results are based at the hourly measurements of 32 meteorological stations. The calculations are made with Matlab 2016a and use adapted models from [Schie, F. 2013] and [Steen, J.M., & Schijndel, A.W.M., 2015]. The model is only accurate between the meteorological stations, outside these limits the values are extrapolated and can give deformed results [Schie, F. 2013].

The map shows high wind driven rain load near the coast of The Netherlands. More land inward the amount of wind driven rain reduces.
For a few meteorological stations a wind rose is produced, which is visible in figure 5.6. The south-west direction is the most prevailing wind direction in the Netherlands, but the wind in not exclusively coming from this direction. Figure 5.6 shows that the south-west wind direction is more dominant land inward. Especially near the coastal areas where the highest WDR loads occur, the wind direction is more equally divided.

Calculating the WDR with equation 1.19 and 1.20 has the same limitation as described for equation 1.17, since the same WDR coefficient of 0.222 (here depicted as 2/9) and the same exponent of 0.88 (here depicted as 8/9) are used. However, the standard makes use of a second equation to transform the airfield indices into a wall index, where the local effects are taken into account.

$$I_{wa} = I_a \cdot C_r \cdot C_t \cdot O \cdot W \quad (1.23)$$

$$I_{ws} = I_s \cdot C_r \cdot C_t \cdot O \cdot W \quad (1.24)$$

C_r = roughness coefficient [-]
C_t = topography coefficient [-]
O = obstruction factor [-]
W = wall factor [-]

The coefficients and the factors from equation 1.23 and 1.24 can be determined with tables described in the EN-ISO standard. These tables can be found in Appendix I [Blocken et al. 2010].

Estimating the amount of rain at a wall using measurements of the meteorological stations is one step into calculating the boundary conditions. The following step is to calculate how much of the rain at the surface is absorbed by the material. [Goesten, S. 2016] assumed that all the rain that has contact with the surface is absorbed by the material. In most cases this will lead to an overestimation of the rain entering the material.

The amount of moisture entering, depends at the moisture capacity of the material. When the material is saturated the remaining moisture will run off, resulting in a thin film at the surface. Some materials with a high porosity, like bricks and mortar are able to absorb all the moisture during a rain event according [Brande, T. 2013]. This assumption should be handled with care, because [Goethem, S. 2014] proved that this statement only holds for buildings with a low exposure rate. Run-off occurs more frequently in the winter when masonry

already contains high amounts of moisture and it occurs at buildings with a high exposure rate (when located in coastal or suburban areas).

At the moment the material is saturated and a film has formed, the pressure difference between the environment and the material (calculated with equation 1.12) immediately drops to 0 Pa [Janssen, H. 2007][Abuku, M. 2009][Brande, T. 2013] [Delgado, J.M.P.Q. 2013].
While the water film is present, the following equation applies:

$$g_l = \min\left(g_e, k_l \frac{\partial p_c}{\partial n} \right) \quad (1.25)$$

n = vector normal to surface
g_l = mass flux of liquid water [kg/m²·s]

g_e is a term known from equation 1.12 and the term $k_l \cdot p_c$ is known from equation 1.10. The term with the lowest value will determine the boundary flux at the construction.

With equation 1.25, it is important to determine precisely how long the water film is present. Brande, T. [2013] describes a run-off model. With the model it is found that the water film doesn't immediately disappear after a rain event at a concrete wall. Instead the thickness of the film steadily decreases due to evaporation.
The run-off model has two effects. At first, the calculated film can reach unsaturated parts where the moisture can be absorbed, resulting in an increase of the total moisture content in the material. And secondly evaporation of moisture inside the material can't take place while the film is present at the surface, resulting in a remaining high moisture content in the material.

5.2.4 Internal boundary conditions

The internal conditions at the boundaries are less complex than the external conditions, since rain isn't present [Vinha, J. 2007][Santos, G.H. 2009][Li, Q. 2009][Portal, N.W. 2011][Vereecken, E. 2015] [Delgado, J.M.P.Q. 2015]. Similar to equation 1.12 the internal boundary conditions can be calculated with the following equation:

$$g_i = \beta_i \left(p_{v,i} - p_{v,s} \right) \quad (1.26a)$$

β_i = surface moisture transfer coefficient [kg/m²·s·Pa]

At the internal boundary the air flux also needs to be added [Hagentoft, C.E. 2004]. Resulting in equation 1.26b when air enters the structure and in equation 1.26c in case air exits the structure.

$$g_i = \beta_i \left(p_{v,e} - p_{v,s} \right) + r_a \cdot \rho_v \quad (1.26b)$$

$$g_i = \beta_i \left(p_{v,i} - p_{v,s} \right) + r_a \cdot \rho_{v,s} \quad (1.26c)$$

The indoor surface transfer coefficient can be calculated according the Lewis analogy [Li, Q. 2009] with the following equation:

$$\beta_i = 7.7 \cdot 10^{-9} \cdot h_{c,i} \quad (1.27)$$

$h_{c,i}$ = convective heat transfer coefficient [W/m²·K]

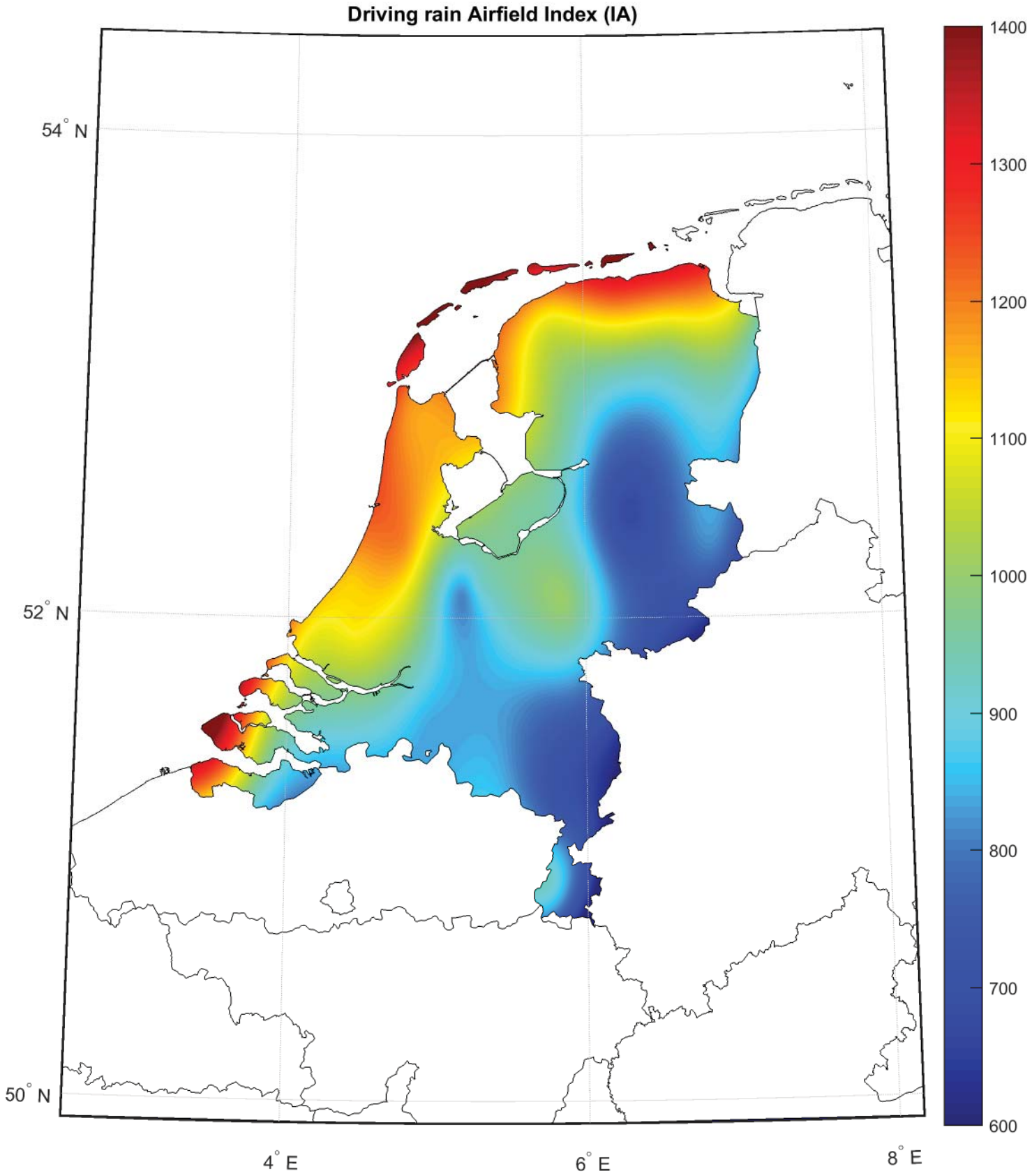

Figure 5.4 Airfield anual index for the Netherlands. Based at hourly measurement data from 1986 to 2016. The data was available for 32 meteorological stations of the KNMI. With the wind-driven rain values are in L/m².

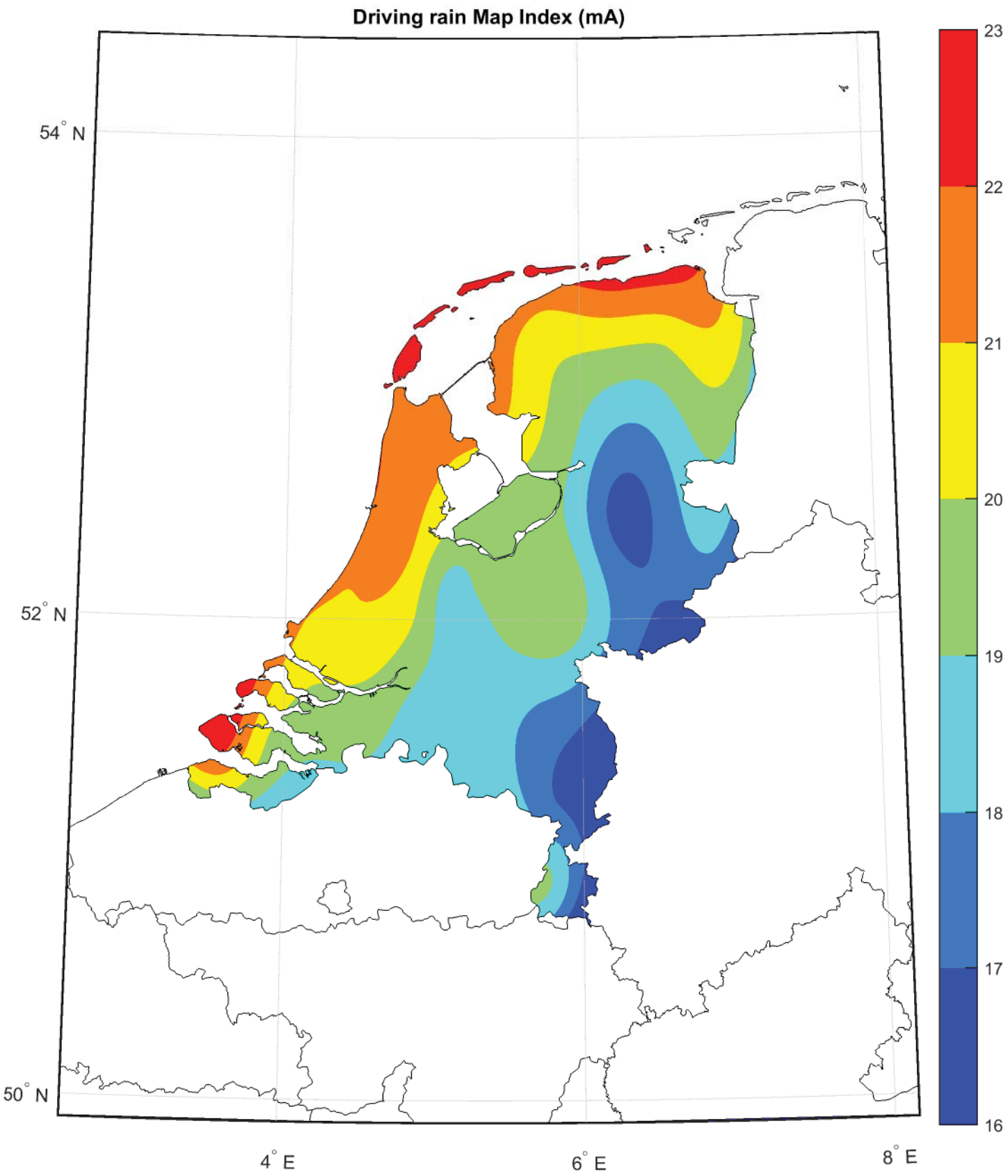

Figure 5.5 Airfield map index for the Netherlands. Based at the spell index from figure 5.4.

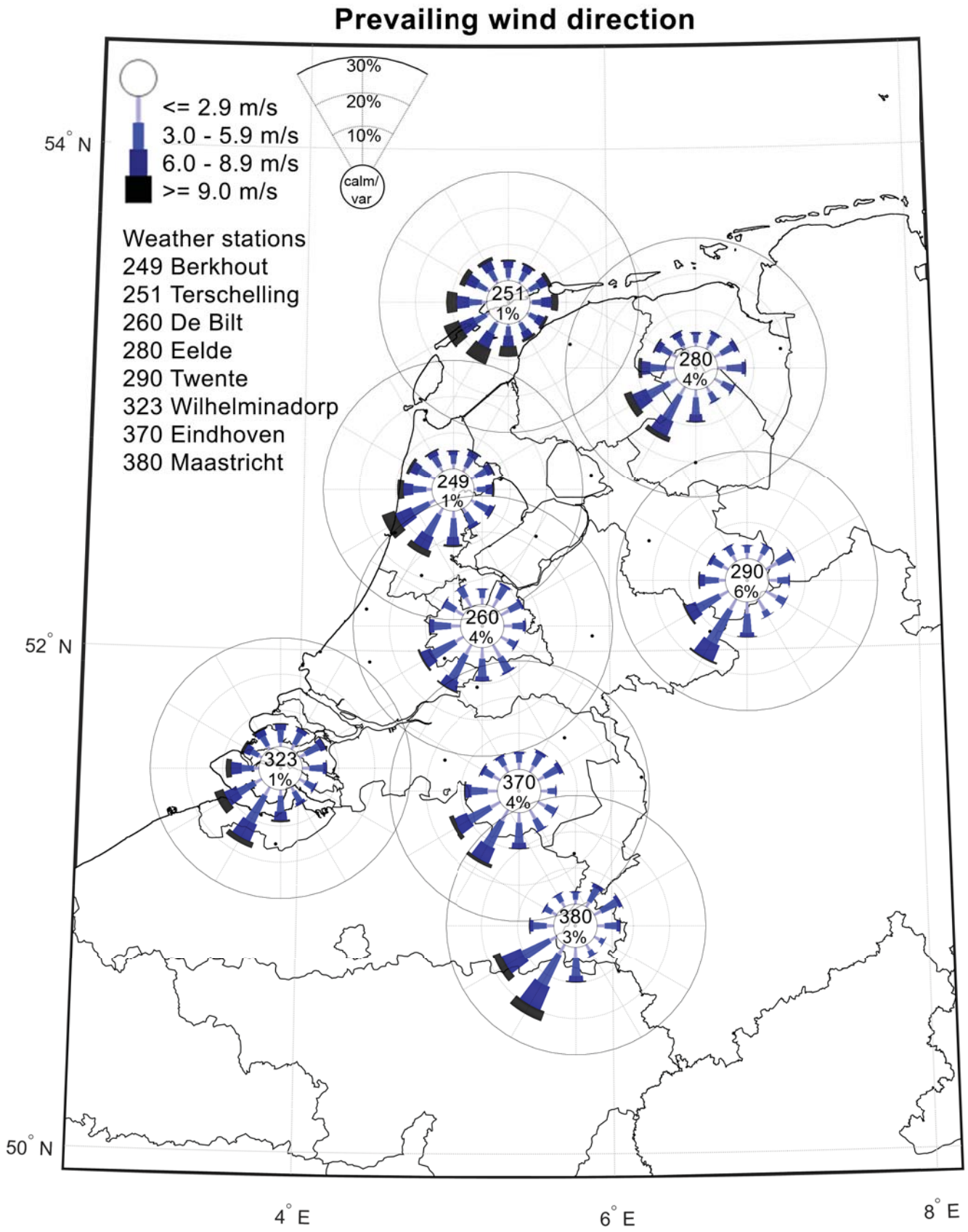

Figure 5.6 Prevailing wind direction for 8 different meteorological stations, extracted from the data that is used to produce figure 5.4. The wind rose is divided into 12 directions. The length of each array defines the time wind is coming from that direction. The different colors define the wind speed. The inner circle contains the number of the station and the amount of time wind is calm or variable expressed in percentage.

5.3 Heat

Heat is analog to the kinetic energy of molecules [Goesten, S. 2016]. In other words, at higher temperatures more kinetic energy is present. The heat transfer can be calculated by applying the energy balance. The total amount of energy consists of conduction and convection [Berger, J. 2014] [Hagentoft, C.E. 2004]. However, it's also possible to divide the energy balance into three parts, which is visible in equation 1.2. Then the convective heat is separated into heat from a dry air flow and heat from the liquid and vapour [Belleudy, C. 2015].

The heat part of equation 1.2 can be simplified into the following form [Berger, J. 2014]:

$$\frac{\partial E}{\partial t} = -\nabla \cdot \left(q_{cond} + q_{conv} \right) \qquad (1.28)$$

5.3.1 Internal energy and driving rain

The internal energy within a material - which is the left part of equation 1.28 - is present in three different forms. Energy of the dry material; energy as a combination where both air and water vapour are present; and energy from water in liquid form.
The combination of air and water vapour is also known as the gaseous phase and is often neglected. Instead the gaseous phase can be split into two parts. Then the calculation only consists of energy from the dry material and energy from the liquid [Hagentoft, C.E. 2004][Berger, J. 2014][Li, Q. 2009]:

$$\frac{\partial E}{\partial t} = \left(c_0 \rho_0 + c_l w \right) \cdot \frac{\partial T}{\partial t} + c_l T \cdot \frac{\partial w}{\partial t} \qquad (1.29)$$

c_0 = specific heat capacity material [J/(kg·K)]
ρ_0 = specific density [kg/m^3]
c_l = specific heat capacity of liquid water [J/(kg·K)]
w = moisture content [kg/m^3]

In equation 1.29 the term $c_l T \cdot \frac{\partial w}{\partial t}$ represents driving rain [Berger, J. 2014]. Other variations of this term are possible, depending on the moisture potential used.
[Vereecken, E. 2015] uses the term $\left(c_l T \cdot \frac{\partial w}{\partial \rho_c} \right) \cdot \frac{\partial \rho_c}{\partial t}$ with capillary pressure (ρ_c) as potential.
The differences between moisture potentials and the advantages of each potential are described more thoroughly at chapter 5.5.1 Heat and moisture potentials.

5.3.2 Conductive heat

As mentioned before, one part of the energy balance equation consists of conductive heat. Conductive heat is determined by the temperature gradient [Berger, J. 2014][Hagentoft, C.E. 2004] [Delgado, J.M.P.Q. 2013]. Following Fourier's law the following equation can be used to determine conductive heat:

$$q_{cond} = -\lambda \left(w \right) \cdot \nabla T \qquad (1.30)$$

λ(w) = thermal conductivity [W/(m·K)]

There is a difference in thermal conductivity depending at the type of material. Isotropic materials have an equal thermal conductivity in all directions of the material. Anisotropic materials like wood have thermal conductivity values that can differ depending at the direction of the heat flow [Vinha, J. 2007].
The thermal conductivity depends on the relative humidty and with that the moisture content inside the material. Also the temperature of the material influences the thermal conductivity [Hagentoft, C.E. 2004][Renato, P. 2013]. More specific Vinha, J. [2007] mentions '*The thermal conductivity of materials increases as temperature and relative humidity rise.'*

5.3.3 Convective heat

Convective heat is also represented in the energy balance equation. Convective heat transfer consists of three flow mechanisms: the liquid flow and vapour flow - both influenced by moisture - and the dry air flow, which is only influenced by air transfer [Li, Q. 2009][Santos, G.H. 2009].
When the liquid flow, vapour flow and dry air flow are combined the following equation is obtained:

$$q_{conv} = \underbrace{L_v \cdot \nabla \left(\delta_p \nabla p_v \right)}_{\textit{liquid flow}} \underbrace{- L_v \cdot r_a \cdot \rho_v}_{\textit{vapour flow}} \underbrace{- r_a \cdot \rho_a \cdot c_{p,a} \cdot \nabla T}_{\textit{dry air flow}} \qquad (1.31)$$

L_v = enthalpy of evaporation/condensation (latent heat) [J/kg]
ρ_v = water vapour density [kg/m^3]
p_v = water vapour pressure [Pa]
δ_p = vapour permeability of the material [kg/m·s·Pa]
r_a = air flow rate [m/s]
ρ_a = density of dry air [kg/m^3]
$c_{p,a}$ = specific heat of dry air [J/kg·K]

As mentioned before, Belleudy, C. [2015] separated the energy balance into three different parts (equation 1.2). The liquid and vapour flow as mentioned in equation 1.31 represent q_{moist} from equation 1.2 and the dry airflow as mentioned in equation 1.31 represents q_{conv} from equation 1.2.

Darcy's law which is used to determine the liquid transport also applies to air transport [Li, Q. 2009] [Belleudy, C. 2015]. This results in the following equation:

$$r_a = -\frac{k_a}{\eta_a} \cdot \left(\nabla p_a + g \cdot \beta \cdot \rho_a \cdot \left(T - T_0 \right) \right) \qquad (1.32a)$$

k_a = air permeability of the material [kg/m·s·Pa]
η_a = dynamic viscosity of air [kg/m·s]
p_a = ambient air pressure [Pa]
β = thermal expansion coefficient of air = $3.43 \cdot 10^{-3}$ [1/K]
g = acceleration due to gravity = 9.81 [m/s^2]
T_0 = reference temperature [K]

The influence of gravity at this equation is debatable. Therefore it can also be left out of the equation [Vinha, J. 2007][Santos, G.H. 2009]. Equation 1.32a then changes to the following equation:

$$r_a = -\frac{k_a}{\eta_a} \cdot \left(\nabla p_a \right) \qquad (1.32b)$$

The dynamic viscosity of air can be calculated with several equations. Sutherland's law is considered to be an accurate method to define the viscosity of air [Fluent Inc, 2006]:

$$\eta_a = \eta_0 \frac{T_0 + S}{T + S} \cdot \left(\frac{T}{T_0} \right)^{3/2} \qquad (1.33)$$

η_0 = reference value [kg/m·s]
S = effective temperature (Sutherland constant) [K]
T_0 = reference temperature [K]

With $\eta_0 = 1.716 \times 10^{-5}$; $T_0 = 273.11$ and $S = 110.56$. Equation 1.33 results in the following equation:

$$\eta_a = 1.716 \cdot 10^{-5} \cdot \frac{273.11 + 110.56}{T + 110.56} \cdot \left(\frac{T}{273.11} \right)^{3/2}$$

The power law is another method to calculate the dynamic viscosity of air. However, it is less accurate than Sutherland's law.

$$\eta_a = \eta_0 \cdot \left(\frac{T}{T_0} \right)^n \qquad (1.34)$$

With $\eta_0 = 1.716 \times 10^{-5}$; $T_0 = 273.11$ and $n = 2/3$. Equation 1.34 results in the following equation:

$$\eta_a = 1.716 \cdot 10^{-5} \cdot \left(\frac{T}{273} \right)^{2/3}$$

5.3.4 External boundary conditions

Both heat transfer and moisture transfer in building constructions depend at the internal conditions and the conditions at the environment around the material.
Aside from the similarities there are also differences. Commonly moisture transfer through a construction is a process of weeks or months. Heat transfer through the same construction however, is commonly a process of hours or days. The difference in duration of these processes is important.
Daily temperature fluctuations reach further into the construction than daily moisture fluctuations. However, a change in temperature also affects the relative moisture levels in the materials [Woloszyn, M. 2008]. In other words, internal or external condensation can occur due to temperature changes. Even when the moisture levels in the material are unchanged.

It is possible to calculate the boundary conditions for heat using different equations. In this study the equation from [Li, Q. 2009] is used as a starting point:

(1.35a)

$$q_e = \underbrace{h_e \cdot \left(T^{eq} - T_s \right)}_{\text{heat from air \& radiation}} + \underbrace{L_v \cdot \beta_e \cdot \left(p_{v,e} - p_{v,s} \right)}_{\text{latent heat}} + \underbrace{g_l \cdot c_l \cdot T_e}_{\text{heat from rain}}$$

β_e = surface moisture transfer coefficient [kg/m^2·s·Pa]
$p_{v,e}$ = water vapour pressure of outdoor air [Pa]
$p_{v,s}$ = water vapour pressure at surface [Pa]
g_l = mass flux of liquid water [kg/m^2·s]
$c_{p,l}$ = specific heat of liquid water [J/kg·K]
h_e = heat transfer coefficient outdoor [W/m^2·K]
T_{eq} = equivalent exterior temperature [K] (combines air temperature, solar radiation and long wave radiation).
T_s = temperature of surface [K]
T_e = temperature of outdoor air [K]

[Li, Q. 2009] describes the external boundary conditions for heat to exist out of three parts. Heat coming from the air and radiation, latent heat that is related to moisture that evaporates/condensates and heat coming from precipitation.
Equation 1.35a shows many similarities to that of [Hagentoft, C.E. 2004]. However the heat coming from airflux seems to be missing. Similar to the moisture boundary conditions there are two additions possible, depending at the direction of the airflux.

When air is entering the structure equation 1.35b applies. If the air exits the structure equation 1.35c applies.

$$q_e = h_e \cdot \left(T_{eq} - T_s\right) + r_a \cdot \rho_a \cdot c_{p,a+v} \cdot T_e + L_v \cdot \left(\beta_e \cdot \left(p_{v,e} - p_{v,s}\right) + r_a \cdot \rho_v\right) + g_l \cdot c_l \cdot T_e \quad (1.35b)$$

$$q_e = h_e \cdot \left(T_{eq} - T_s\right) + r_a \cdot \rho_a \cdot c_{p,a+v} \cdot T_s + L_v \cdot \left(\beta_e \cdot \left(p_{v,e} - p_{v,s}\right) + r_a \cdot \rho_{v,s}\right) \quad (1.35c)$$

r_a = air flow rate [m/s]
ρ_a = density of dry air [kg/m^3]
$c_{p,a+v}$ = specific heat of air and water vapour [J/kg·K]
T_e = temperature of outdoor air [K]

In equation 1.35 it is assumed that the temperature of the rain droplets is equal to that of the exterior air. This assumption is debatable [Janssen, 2007], however, Janssen also refers to his thesis from 2002 in which he demonstrated that including the actual temperature of rain *"had practically no effect on surface temperature."*
The heat transfer coefficient (h_e) from equation 1.35 consists of both the convective ($h_{c,e}$) and the longwave radiative part ($h_{r,e}$) [Hagentoft, C.E. 2004]. It is possible to decouple both, but this also requires changes to equation 1.31 [Janssen, H. 2007] [Abuku, M. 2009][Delgado, J.M.P.Q. 2013].

The radiative heat transfer coefficient of the wall depends at the longwave radiation coming from the sky and the ground [Aelenei and Henriques, 2008] and can be calculated with the following equation:

$$h_{r,e} = \varepsilon_s \cdot \sigma \cdot \left[T_s^4 + \left(0.5 \cdot \varepsilon_g - 1\right) \cdot \varepsilon_{sky} \cdot T_e^4 - 0.5 \cdot \varepsilon_g \cdot T_g \right. \quad (1.36)$$

ε_s = emissivity exterior surface [-]
ε_{sky} = emissivity sky [-]
ε_g = emissivity ground [-]

The other variable that defines the heat transfer near the surface, is the convective heat transfer coefficient ($h_{c,e}$). $h_{c,e}$ depends at the wind speed and the wind direction around the structure. [Vereecken, E. 2015] and [Janssen, H. 2007] use the following equations:

$$h_{c,e} = 1.7 \cdot V_{loc} + 5.1 \quad (1.37)$$

V_{loc} = local wind velocity at 0.3 m distance from the building wall external surface [m/s]

$$V_{loc} = 1.8 \cdot U_{10} + 0.2 \quad \text{(windward)} \quad (1.38)$$

$$V_{loc} = 0.2 \cdot U_{10} + 1.7 \quad \text{(leeward)} \quad (1.39)$$

U_{10} = wind-free stream velocity measured at a height of 10 m above the building roof [m/s]

The equations above are one of many ways to calculate $h_{c,e}$, since there is no consistency within literature on how to calculate this variable [Janssen, H. 2007][Defraeye, T. 2011][Delgado, J.M.P.Q. 2013].
Convective heat transfer not only affects the heat entering a construction, but is also related to the moisture transfer, due to the Lewis relation mentioned in chapter 5.2.3.
The coupling of convective heat transfer and the wind speed around a building causes an uncertainty which is similar to that of the wind-driven-rain calculation. The uncertainty is caused by absence of the local airflow patterns, terrain roughness and the roughness of the façade in equations 1.37 - 1.39. Possible errors that may occur due to this uncertainty are reason to either make use of CFD [Defraeye, T. 2011] or a single-value for both $h_{c,e}$ and β_e [Abuku, M. 2009]. For h_e also a single-value can be used [Hagentoft, C.E. 2004][Vinha, J. 2007] [Janetti, M.B. 2011][Harrestrup, M. 2016].

The equivalent temperature can be calculated with the following equation [Hagentoft, C.E. 2012]:

$$T_{eq} = T_e + R_{s,e} \cdot \left(I_g \cdot \alpha_{sol} + h_{r,e} \cdot \left(T_{sky} - T_e\right)\right) \quad (1.40)$$

$R_{s,e}$ = surface resistance [m^2·K/W]
I_g = global solar irradiation [W/m^2]
α_{sol} = solar absorptance surface [-]
$h_{r,e}$ = radiative heat transfer coefficient [W/m^2·K]
T_{sky} = sky temperature [K]

The sky temperature can be calculated with the following equation [Aelenei and Henriques, 2008] [Hagentoft, C.E. 2012]:

$$T_{sky} = \sqrt[4]{\frac{I_{lw}}{\sigma}} \cdot \quad (1.41)$$

σ = Stefan-Bolzmann constant
I_{lw} = long wave irradiation [W/m^2]

5.3.5 Internal boundary conditions

The analogy between the moisture boundary conditions and the heat boundary conditions also apply to the internal conditions. The equation to calculate the internal boundary conditions is less complex than the equation of the external boundary conditions, due to the precipitation term that is left out and the indoor air temperature (T_i) that replaces the T^{eq} term [Li, Q. 2009].

$$q_i = h_i \cdot \left(T_i - T_s\right) + L_v \cdot \beta_i \cdot \left(p_{v,i} - p_{v,s}\right) \quad (1.42a)$$

h_i = heat transfer coefficient of interiour [W/m²·K]
T_i = interiour temperature [K]

At the internal boundary the air flux also needs to be added [Hagentoft, C.E. 2004]. Resulting in equation 1.24b when air enters the structure and in equation 1.24c in case air exits the structure.

$$q_i = h_i \cdot (T_i - T_s) + r_a \cdot \rho_a \cdot c_{p,a+v} \cdot T_i + L_v \cdot (\beta_i \cdot (p_{v,i} - p_{v,s}) + r_a \cdot \rho_v) \quad (1.42b)$$

$$q_i = h_i \cdot (T_i - T_s) + r_a \cdot \rho_a \cdot c_{p,a+v} \cdot T_s + L_v \cdot (\beta_i \cdot (p_{v,i} - p_{v,s}) + r_a \cdot \rho_{v,s}) \quad (1.42c)$$

The heat transfer coefficient (h_i) from equation 1.42 consists of both the convective ($h_{c,i}$) and the radiative part ($h_{r,i}$) [Hagentoft, C.E. 2004]. $h_{r,i}$ can be calculated with 1.36, but that equation is specified to the external boundary. [Vinha, J. 2007] provides an equation that is more useful for the internal radiation coefficient:

$$h_{r,i} = \varepsilon \cdot \sigma \cdot (T_s + T_{surr}) \cdot (T_s^2 + T_{surr}^2) \approx 4 \cdot \varepsilon \cdot \sigma \cdot \left(\frac{T_s + T_{surr}}{2}\right)^3 \quad (1.43)$$

T_{surr} = Temperature of surrounding surfaces [K]

$h_{c,i}$ can be calculated with the following equation [Hagentoft, C.E. 2001]:

$$h_{c,i} = 2 \cdot |T_i - T_s|^{1/4} \quad (1.44)$$

The equation above is one way to calculate $h_{c,i}$, but again there is no consistency in literature for the calculation of the convective heat transfer [Delgado, J.M.P.Q. 2013]. CFD could be a solution to calculate the exact value for $h_{c,i}$. However, the use of a single-value is also common [Hagentoft, C.E. 2004][Vinha, J. 2007][Janetti, M.B. 2011][Vereecken, E. 2015] [Harrestrup, M. 2016].

5.4 Air

Different equations regarding the convective transfer of heat and moisture are also related to air. These are already mentioned in the previous paragraphs. Only the dry air flux remains.

5.4.1 Air flux

The air flux mentioned in the balance equation (equation 1.2) can be simplified for the built environment, due to the low air flow that is present and the incompressability of the air flow [Belleudy, C. 2015][Janetti, M.B. 2016]:

$$\nabla \cdot r_a = 0 \quad (1.45)$$

With this simplification the air flow (as described in equation 1.31) represents the complete airflux.

The air pressure difference can be measured. However when no measurements are available an estimate can calculated based at the stack-effect (temperature driven air pressure difference) [Kehl, D. 2013]:

$$\Delta P = \rho_a \cdot \frac{T_e - T_i}{T_i} \cdot g \cdot \frac{h}{2} \quad (1.46)$$

ΔP = air pressure difference [Pa]
ρ_a = density of dry air [kg/m³]
g = gravity
h = height of the building [m]

5.4.2 Boundary conditions

The air flow conditions at the internal (equation 1.47) and external (equation 1.48) boundaries show similarities to the boundary conditions for vapour pressure [Belleudy, C. 2015]:

$$g_{a,e} = \beta_a (p_{a,e} - p_{a,s}) \quad (1.47)$$

$$g_{a,i} = \beta_a (p_{a,i} - p_{a,s}) \quad (1.48)$$

β_a = surface air transfer coefficient [kg/m²·s·Pa]
$p_{a,e}$ = air pressure of outdoor air [Pa]
$p_{a,i}$ = air pressure of indoor air [Pa]
$p_{a,s}$ = air pressure at surface [Pa]

5.5 Software application

5.5.1 Moisture potential

There are different moisture potentials that can be used in the moisture balance equation. Some examples are: Capillary pressure (p_c); Moisture content (w); absolute humidity (ω); relative humidity (φ) and Vapour pressure (p). The decision which potential should be used is important, since each potential is advantageous in a different situation.

In the built environment constructions are usually made from a combination of materials. Some moisture potentials, like the moisture content (w), have difficulties with calculating moisture at the interface of materials. While other potentials, like vapour pressure (p) and relative humidity (φ), assume continuity at the interface [Tariku, F. 2010] [Belleudy, C. 2015].

With relative humidity as moisture potential, the moisture retention curve $w(\varphi)$ is continuous at the interface. Therefore it can be used as a true potential for the vapour and capillary transport when measuring the moisture retention curve of a material [Nespoli, L. 2013a].

The true moisture potential for vapour transport is vapour pressure (p). For liquid transport the true moisture potential is capillary pressure (p_c) [Vinha, J. 2007][Wit, M. 2009][Nespoli, L. 2013a][Janssen, H. 2014].

In this research Lp_c (logarithmic capillary pressure) is used as the moisture potential. This moisture potential has been chosen by Uittenbosch, S. [2012] in favor of other moisture potentials. This decision is based at research from Portal, N.W. et al. [2011]. According to Portal, N.W. et al. [2011] a better numerical stability is acquired when Lp_c is chosen as moisture potential. Especially when extreme conditions at the boundaries are present, i.e. fluctuations regarding rain. This statement is repeated by Portal, N.W. et al. [2013].

[Janssen, H. 2014] compares three different potentials, capillary pressure (p_c); relative humidity (φ) and $-\log 10$(capillary pressure) Lp_c. Which relate to each other as follows:

$$\frac{\partial w}{\partial p_c}\cdot\frac{\partial p_c}{\partial t}=\nabla\cdot\left[\left(k_l+\delta_p\cdot p_{sat}\cdot\frac{\partial\varphi}{\partial p_c}\right)\cdot\nabla p_c\right]$$

$$\frac{\partial w}{\partial p_c}\cdot\frac{\partial p_c}{\partial\varphi}\cdot\frac{\partial\varphi}{\partial t}=\nabla\cdot\left[\left(k_l\cdot\frac{\partial p_c}{\partial\varphi}+\delta_p\cdot p_{sat}\right)\cdot\nabla\varphi\right]$$

$$-p_c\cdot\ln(10)\cdot\frac{\partial w}{\partial p_c}\frac{\partial Lp_c}{\partial t}=$$

$$\nabla\left[-p_c\cdot\ln(10)\cdot\left(k_l+\delta_p\cdot p_{sat}\cdot\frac{\partial\varphi}{\partial p_c}\right)\cdot\nabla Lp_c\right]$$

Janssen, H. [2014] found that numerical instability is not an issue for all three potentials. Which makes the argument to choose for Lp_c by Uittenbosch, S. [2012] invalid. [Janssen, H. 2014] does advocate the Lp_c in terms of numerical efficiency in the hygroscopic region. In the near saturation region φ and p_c are in favor when it comes to numerical efficiency.

Goesten, S. [2016] continued the work of Uittenbosch, S. [2012] and showed that the simulations with Lp_c as moisture potential produced trustworthy results for all the HAMSTAD benchmarks. Which is confirmed by Schijndel, A.W.M. [2016].

5.5.2 Comsol

In COMSOL there are two different models (see figure 5.7). The model with a seperate convective flux, where Heat, Air and Moisture transfer are implemented in COMSOL using two PDE coefficients. The first PDE contains the heat and moisture flux, the second PDE contains the air flux. The model with an implemented convective flux, where the PDE coefficient calculating the air flux is removed and the air transfer is implemented into the boundary equations of heat and moisture.

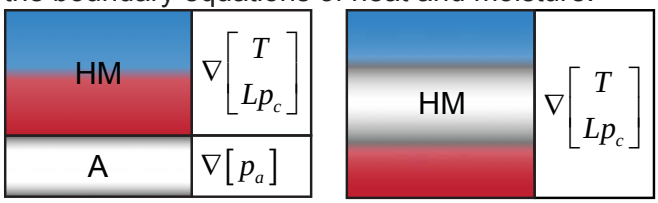

Figure 5.7 The two different models possible in COMSOL. left: the model with seperate convective flux (consists of two PDE coefficients). right: the model with implemented convective flux (single PDE coefficient).

In appendix II the Lp_c moisture potential is implemented into the balance equations. Below the balance equation for heat and moisture are rewritten into the correct form that can be applied to COMSOL. These equations are based at work of [Janetti, M.B. 2012] and [Goesten, S. 2016].

Heat and Moisture

The equation for heat transfer and temperature change in the material is:

$$\left(\rho\cdot c+c_l\cdot w\right)\frac{\partial T}{\partial t}=\left(\nabla\lambda+L_v\cdot\right. \qquad (1.49)$$

$$\left.\left(\nabla\delta_p-r_a\cdot\rho_v\right)\cdot\varphi\cdot\frac{\partial p_{sat}}{\partial T}-r_a\cdot\rho_a\cdot c_{pa}\right)\cdot\nabla T+$$

$$L_v\cdot\left(\nabla\delta_p+r_a\cdot\rho_v\right)\cdot p_{sat(T)}\cdot\frac{\varphi}{\rho_w\cdot R_v\cdot T}\cdot\frac{\partial p_c}{\partial Lp_c}\cdot\nabla Lp_c$$

The equation for moisture transfer and moisture storage is:

$$\frac{\partial w}{\partial p_c}\cdot\frac{\partial p_c}{\partial Lp_c}\cdot\frac{\partial Lp_c}{\partial t}= \tag{1.50}$$

$$\left(\nabla\delta_p - r_a\cdot\rho_v\right)\cdot\varphi\cdot\frac{\partial p_{sat}}{\partial T}\cdot\nabla T+\left(\left(\left(-\nabla\delta_p + r_a\cdot\rho_v\right)\cdot p_{sat(T)}\cdot\frac{\varphi}{\rho_w\cdot R_v\cdot T}\cdot\frac{\partial p_c}{\partial Lp_c}\right)-\nabla k_l\cdot\frac{\partial p_c}{\partial Lp_c}\right)\nabla Lp_c$$

ρ = specific density [kg/m³]
ρ_v = density of water vapour [kg/m³]
ρ_w = density of water [kg/m³]
c = specific heat capacity of the material [J/(kg·K)]
c_l = specific heat capacity of water [J/(kg·K)]
c_p = specific heat capacity of air [J/(kg·K)]
w = moisture content [kg/m³]
T = absolute temperature [K]
t = time [s]
λ = thermal conductivity [W/(m·K)]
L_v = latent heat of evaporation [J/kg]
δ_a = water vapor permeability of air [s]
μ = water vapor resistance factor [-]
r_a = air flux through the material [kg/(m²·s)]
φ = relative humidity [-]
p_{sat} = saturation pressure [Pa]
R_v = gas constant of water [J/(kg·K)]
p_c = capillary pressure [Pa]
Lp_c = logarithmic capillary pressure [Pa]
k_l = moisture permeability [kg/(s·m·Pa)]

Equations (1.49 and 1.50) combined in matrix form:

$$\begin{bmatrix}\left(\rho\cdot c + c_l\cdot w\right) & 0\\ 0 & \frac{\partial w}{\partial p_c}\cdot\frac{\partial p_c}{\partial Lp_c}\end{bmatrix}\cdot\begin{bmatrix}\frac{\partial T}{\partial t}\\ \frac{\partial Lp_c}{\partial t}\end{bmatrix}=$$

$$\left(\nabla\cdot\begin{bmatrix}\lambda + L_v\cdot\delta_p\cdot\varphi\cdot\frac{\partial p_{sat}}{\partial T} & -L_v\cdot\delta_p\cdot p_{sat(T)}\cdot\frac{\varphi}{\rho_w\cdot R_v\cdot T}\cdot\frac{\partial p_c}{\partial Lp_c}\\ \delta_p\cdot\varphi\cdot\frac{\partial p_{sat}}{\partial T} & -k_l\cdot\frac{\partial p_c}{\partial Lp_c}-\delta_p\cdot p_{sat(T)}\cdot\frac{\varphi}{\rho_w\cdot R_v\cdot T}\cdot\frac{\partial p_c}{\partial Lp_c}\end{bmatrix}\cdot\nabla\begin{bmatrix}T\\ Lp_c\end{bmatrix}\right)$$

$$+\left(r_a\begin{bmatrix}-\left(\rho_a\cdot c_{pa}+L_v\cdot\rho_v\cdot\varphi\cdot\frac{\partial p_{sat}}{\partial T}\right) & L_v\cdot\rho_v\cdot p_{sat(T)}\cdot\frac{\varphi}{\rho_w\cdot R_v\cdot T}\cdot\frac{\partial p_c}{\partial Lp_c}\\ -\rho_v\cdot\varphi\cdot\frac{\partial p_{sat}}{\partial T} & \rho_v\cdot p_{sat(T)}\cdot\frac{\varphi}{\rho_w\cdot R_v\cdot T}\cdot\frac{\partial p_c}{\partial Lp_c}\end{bmatrix}\cdot\nabla\begin{bmatrix}T\\ Lp_c\end{bmatrix}\right)$$

Above matrix can't be implemented into COMSOL directly. To do so, in COMSOL a coefficient form PDE is used.
[Janetti, M.B. 2012] interprets the PDE as follows:

$$\begin{cases}e_a\cdot\frac{\partial^2 u}{\partial t^2}+d_a\cdot\frac{\partial u}{\partial t}+\nabla\cdot\left(-c\cdot\nabla u-\alpha\cdot u+\gamma\right) & \\ \beta\cdot\nabla u+a\cdot u=f & \text{in } \Omega\\ -n\cdot\left(-c\cdot\nabla u-\alpha\cdot u+\gamma\right)+q\cdot u=g & \text{on } \partial\Omega\end{cases}$$

u = dependent variable {φ,T}
e_a = α = a = f = q_1 = q_2 = g_1 = {0,0}
β = convection coefficient {0,0}
d_a = damping coefficient {du/dφ,C}
c = diffusion coefficient $\{D_{m,\varphi},D_{e,T}\}$
γ = flux source term $\{-D_{m,T}\cdot\nabla T,-D_{e,\varphi}\cdot\nabla\varphi\}$
g_2 = boundary conditions {j,0}
Ω = computational domain (union of sub-domains)
∂Ω = the domain boundary

[Janetti, M.B. 2012] uses φ as a moisture potential. Lp_c can be used as a substitute for this term. [Goesten, S. 2016] uses the PDE different by switching the term β with the term γ.
Resulting in the following form:

$$\begin{cases}d_a\cdot\frac{\partial u}{\partial t}+\nabla\cdot\left(-c\cdot\nabla u\right)+\beta\cdot\nabla u=0 & \text{in } \Omega\\ -n\cdot\left(-c\cdot\nabla u\right)=g & \text{on } \partial\Omega\end{cases}$$

For the computational domain the switch of β with γ makes the PDE more efficient since the dependent variables are already included. In the domain boundary, however, this results in a missing term compared to [Janetti, M.B. 2012].
The usage of the PDE coefficients by [Goesten, S. 2016] for Heat and Moisture coincides with the usage by [Nusser, B. 2012], however, the air coefficient isn't described by Nusser, B. [2012].
Beleudy, C. [2015] describes the Heat, Moisture and Air. Instead of using a matrix, Beleudy, C. splits the terms. Unused coefficients by [Goesten, S. 2016] and [Janetti, M.B. 2012] are used by [Beleudy, C. 2015] to make splitting of the terms possible.

The combined matrix has been separated to match the PDE terms in COMSOL [Goesten, S. 2016].

$$d_a = \begin{bmatrix} (\rho \cdot c + c_l \cdot w) & 0 \\ 0 & \frac{\partial w}{\partial p_c} \cdot \frac{\partial p_c}{\partial Lp_c} \end{bmatrix}$$

$$c = \begin{bmatrix} \lambda + L_v \cdot \delta_p \cdot \varphi \cdot \frac{\partial p_{sat}}{\partial T} & -L_v \cdot \delta_p \cdot p_{sat(T)} \cdot \frac{\varphi}{\rho_w \cdot R_v \cdot T} \cdot \frac{\partial p_c}{\partial Lp_c} \\ \delta_p \cdot \varphi \cdot \frac{\partial p_{sat}}{\partial T} & -k_l \cdot \frac{\partial p_c}{\partial Lp_c} - \delta_p \cdot p_{sat(T)} \cdot \frac{\varphi}{\rho_w \cdot R_v \cdot T} \cdot \frac{\partial p_c}{\partial Lp_c} \end{bmatrix}$$

$$\beta = r_a \begin{bmatrix} -\left(\rho_a \cdot c_{pa} + L_v \cdot \rho_v \cdot \varphi \cdot \frac{\partial p_{sat}}{\partial T} \right) & L_v \cdot \rho_v \cdot p_{sat(T)} \cdot \frac{\varphi}{\rho_w \cdot R_v \cdot T} \cdot \frac{\partial p_c}{\partial Lp_c} \\ -\rho_v \cdot \varphi \cdot \frac{\partial p_{sat}}{\partial T} & \rho_v \cdot p_{sat(T)} \cdot \frac{\varphi}{\rho_w \cdot R_v \cdot T} \cdot \frac{\partial p_c}{\partial Lp_c} \end{bmatrix}$$

Each matrix can be simplified using different coefficients as substitute:

$$d_a = \begin{bmatrix} B_T\left(Lp_c, T\right) & 0 \\ 0 & B_L\left(Lp_c, T\right) \end{bmatrix}$$

$$c = \begin{bmatrix} D11\left(Lp_c, T\right) & D12\left(Lp_c, T\right) \\ D21\left(Lp_c, T\right) & D22\left(Lp_c, T\right) \end{bmatrix}$$

$$\beta = r_a \begin{bmatrix} C11\left(Lp_c, T\right) & C12\left(Lp_c, T\right) \\ C21\left(Lp_c, T\right) & C22\left(Lp_c, T\right) \end{bmatrix}$$

The coefficients then represent the following equations, with B as buffer, D as diffusion and C as convection coefficient.

$B_T\left(Lp_c, T\right) = \left(\rho \cdot c + c_l \cdot w\right)$	$B_L\left(Lp_c, T\right) = \frac{\partial w}{\partial p_c} \cdot \frac{\partial p_c}{\partial Lp_c}$
$D11\left(Lp_c, T\right) = \lambda + L_v \cdot \delta_p \cdot \varphi \cdot \frac{\partial p_{sat}}{\partial T}$ $D21\left(Lp_c, T\right) = \delta_p \cdot \varphi \cdot \frac{\partial p_{sat}}{\partial T}$	$D12\left(Lp_c, T\right) = -L_v \cdot \delta_p \cdot p_{sat(T)} \cdot \frac{\varphi}{\rho_w \cdot R_v \cdot T} \cdot \frac{\partial p_c}{\partial Lp_c}$ $D22\left(Lp_c, T\right) = -k_l \cdot \frac{\partial p_c}{\partial Lp_c} - \delta_p \cdot p_{sat(T)} \cdot \frac{\varphi}{\rho_w \cdot R_v \cdot T} \cdot \frac{\partial p_c}{\partial Lp_c}$
$C11\left(Lp_c, T\right) = -\left(\rho_a \cdot c_{pa} + L_v \cdot \rho_v \cdot \varphi \cdot \frac{\partial p_{sat}}{\partial T} \right)$ $C21\left(Lp_c, T\right) = -\rho_v \cdot \varphi \cdot \frac{\partial p_{sat}}{\partial T}$	$C12\left(Lp_c, T\right) = L_v \cdot \rho_v \cdot p_{sat(T)} \cdot \frac{\varphi}{\rho_w \cdot R_v \cdot T} \cdot \frac{\partial p_c}{\partial Lp_c}$ $C22\left(Lp_c, T\right) = \rho_v \cdot p_{sat(T)} \cdot \frac{\varphi}{\rho_w \cdot R_v \cdot T} \cdot \frac{\partial p_c}{\partial Lp_c}$

5.5.3 Delphin

The following differential equations apply to the calculations with Delphin [Delgado, J.M.P.Q. 2013].
Moisture mass balance:

$$\frac{\partial}{\partial t}\left(\rho_w\theta_l+\rho_v\theta_g\right)=-\frac{\partial}{\partial x}\left[\left(\frac{\rho_w}{v-j_{disp}-j_{diff}}\right)\theta_l+\left(\frac{\rho_v}{v+j_{diff}}\right)\theta_g\right]$$

Air mass balance:

$$\frac{\partial}{\partial t}\left(\rho_a\theta_g\right)=-\frac{\partial}{\partial x}\left[\left(\frac{\rho_a}{v-j_{diff}}\right)\theta_g\right]$$

Salt mass balance:

$$\frac{\partial}{\partial t}\left(\rho_s\theta_l+\rho_p\theta_p\right)=-\frac{\partial}{\partial x}\left[\left(\frac{\rho_s}{v-j_{disp}-j_{diff}}\right)\theta_l\right]$$

Internal energy balance (salt included):

$$\frac{\partial}{\partial t}\left[\rho c_p T+\rho_p c_{pp}T\theta_p+\rho_w c_{pl}T\theta_l+\left(\rho_v c_{pv}T+\rho_a c_{pa}T\right)\theta_g\right]=-\frac{\partial}{\partial x}\left[\left(\frac{\rho_w c_{pl}T}{v\theta_l}\right)+\left(\frac{\rho_v c_{pv}T+\rho_a c_{pa}T}{v\theta_g}\right)\right]$$

$$-\frac{\partial}{\partial x}\left[-\lambda\frac{\partial T}{\partial x}+\left(h_s-h_w\right)\left(j_{disp}+j_{diff}\right)\theta_l+\left(h_v-h_a\right)j_{diff}\theta_g\right]$$

Internal energy balance (salt excluded):

$$\frac{\partial}{\partial t}\left[\rho c_p T+\rho_w c_{pl}T\theta_l+\left(\rho_v c_{pv}T+\rho_a c_{pa}T\right)\theta_g\right]=-\frac{\partial}{\partial x}\left[\left(\frac{\rho_w c_{pl}T}{v\theta_l}\right)+\left(\frac{\rho_v c_{pv}T+\rho_a c_{pa}T}{v\theta_g}\right)\right]$$

$$-\frac{\partial}{\partial x}\left[-\lambda\frac{\partial T}{\partial x}+\left(h_s-h_w\right)\left(j_{disp}+j_{diff}\right)\theta_l+\left(h_v-h_a\right)j_{diff}\theta_g\right]$$

Wind-driven rain coefficients:

$$U=\begin{cases}0 & if\left(\beta_{wind}\geq\dfrac{\pi}{2}\right)\vee\left(v_{wind}\leq 0\right)\\ \dfrac{\cos\left(\beta_{wind}\right)}{\sqrt{1+1141\cdot\sqrt{\dfrac{3600\cdot R_h}{v^4_{wind}}}}}\cdot\exp\left(-\dfrac{12}{5\cdot\sqrt[4]{3600\cdot R_h}}\right)\end{cases}$$

$$\beta_{wind}=\begin{cases}\left|\alpha_{wall}-\alpha_{wind}\right| & if\ \left|\alpha_{wall}-\alpha_{wind}\right|\leq\pi\\ 2\pi-\left|\alpha_{wall}-\alpha_{wind}\right| & \left|\alpha_{wall}-\alpha_{wind}\right|>\pi\end{cases}$$

ρ_w = liquid moisture partial density [kg/m³]
ρ_v = mass density of water vapour [kg/m³]
ρ_a = air partial density [kg/m³]
ρ_p = mass density of precipitated salt [kg/m³]
ρ_s = mass density of dissolved salt [kg/m³]
ρ = density of dry porous material [kg/m³]

θ_l = volumetric content of liquid phase [m³/m³]
θ_g = volumetric content of gaseous phase [m³/m³]
θ_p = volumetric content of precipitated salt [m³/m³]
v = humidity by volume in surrounding air [kg/m³]

c_p = heat capacity of solid material [J/kg·K]
c_{pp} = heat capacity of precipitated salt [J/kg·K]
c_{pl} = heat capacity of liquid water [J/kg·K]
c_{pv} = heat capacity of water vapour [J/kg·K]
c_{pa} = heat capacity of air [J/kg·K]

λ = thermal conductivity [W/m·K]

j_{disp} = dispersive flux
j_{diff} = diffusive flux

h_v = partial specific enthalphy of water vapour [J/kg]
h_w = partial specific enthalphy of water [J/kg]
h_s = partial specific enthalphy of salt [J/kg]
h_a = partial specific enthalphy of air [J/kg]

R_h = horizontal rainfall [kg/m²·s]
v_{wind} = wind speed [m/s]

6 Model improvement

[Goesten, S. 2016] simulated four wall assemblies based at the measurements from [Rafidiarison, H. et al. 2015].
Two different models are used that both include convective transport. A model where the airflux and convective boundary conditions are implemented into the heat and moisture PDE coefficients. And a model where the airflux and convective boundary conditions have their own PDE coefficient.
The simulations showed mixed results for the different assemblies. Overall the results of the simulation for temperature showed good analogy to the measurements (excluding the indoor and outdoor values, the RMSE variates between 1.67-4.67%). The relative humidity in the simulations had a larger differentiation from the measurements (excluding the indoor and outdoor values, the RMSE variates between 3.19-8.89%) [Goesten, S. 2016].

Since the measurements are 1D and no liquid water is involved in the measurements, the moisture content inside the material is determined by the relative humidity and the temperature [Engelund, E.T. 2011]. The influence of gravity, rising damp and the influence of rain (all mentioned as possible improvements by Goesten) can be neglected.

Some improvements, mentioned by Goesten, S. [2016] and found in the previous Chapter are still possible:
- Improving accuracy of vapour permeability (δ_p);
- Usage of material properties from Rafidiarison, et al. [2015] instead of mixed properties from the article and Delphin;
- Adding hysteresis to the model.

The improvement of the models could be found in the assignment of the correct hygrothermal properties to the materials.
However, before this improvement could me made, it needs to be certain that the models by Goesten, S. [2016] produces trustworthy results. If not, one tries to compensate bad simulations by adapting the materials until the results meet the measurements.

6.1 Comparison with Delphin

Goesten, S. [2016] showed that the COMSOL model produced good results for the HAMSTAD benchmarks, compared to other simulation software. Delphin also showed good results compared to other software when the HAMSTAD benchmarks were simulated [Sontag, L. et al. 2013].
It could be stated that the COMSOL model of Goesten, S. [2016] is correct for the simulations of the HAMSTAD benchmarks.
To be certain if the COMSOL model also performs well when all transport mechanisms are combined, the COMSOL model from Goesten, S. [2016] is directly compared to Delphin.
For this comparison, wall assembly 2 and wall assembly 4 from Rafidiarison, et al. [2015] are simulated (see figure 6.1) with both COMSOL models.
The material properties and the boundary conditions are similarized. All material properties are coming from the database in Delphin. The materials *'Gypsum plaster'*, *'Wood fibre insulation board'* and *'OSB board'* from the Delphin material database are used.
The boundary conditions and air permeability of the materials (see table 6.1) are extracted from the models of Goesten, S. [2016].

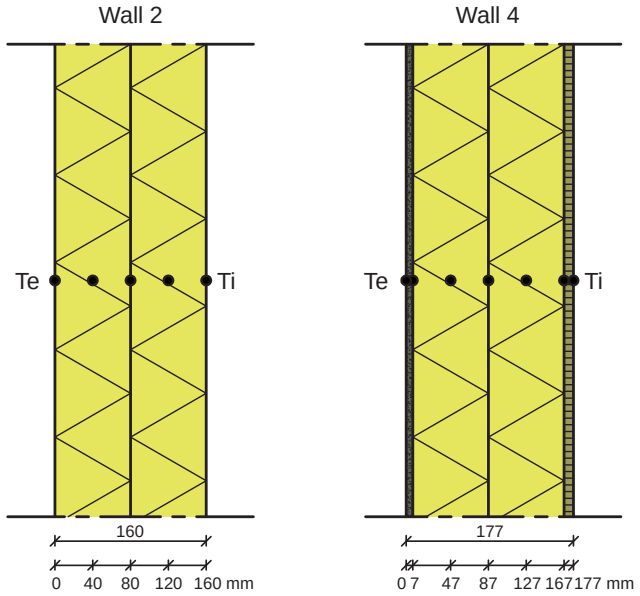

Figure 6.1 Wall setup from [Rafidiarison, et al. 2015]. Wall assembly 2 (left) consists of two layers wood fibre board. Wall assembly 4 (right) consists of lime plaster, wood fibre board and OSB (from outside to inside).

Table 6.1 Parameters used for the simulations with Delphin and COMSOL. Coming from Goesten, S. [2016].

Parameter	Dimension	Wall 2	Wall 4
β_e	[s/m]	$5.8382 \cdot 10^{-9}$	$5.8382 \cdot 10^{-9}$
β_i	[s/m]	$5.8823 \cdot 10^{-9}$	$5.8823 \cdot 10^{-9}$
h_e	[W/m^2 K]	16	19
h_i	[W/m^2 K]	7	4
$k_{g;fibre}$	[s]	$1 \cdot 10^{-6}$	-
$k_{g;plaster}$	[s]	$1 \cdot 10^{-8}$	-
$k_{g;OSB}$	[s]	1e-7	-

6.1.1 Model with implemented convective flux

The results between the Delphin simulation and the COMSOL simulation show good similarity for the temperature.
Wall 2 shows differences <0.6°C, while for wall 4 the differences are even <0.2°C. The results for the relative humidity show larger deviations up to >4% for wall 2. For wall 4 the differences are >1%. This is also reflected in the calculations of the RMSE and maximum errors (see table 6.2 & 6.3).

Improving vapour permeability

One difference between the Delphin model and the COMSOL model, is the calculation of vapour permeability (δ_p).
The difference in calculation is already adressed in chapter 5.2. As an improvement to the model, the Schirmer equation is implemented into the model with equation 1.5a and 1.6.

$$\delta_p = \frac{\delta_a}{\mu} \quad (1.5a) \qquad \delta_a = \frac{D_v}{R_v T} \quad (1.6)$$

D_v is assumed as a single-value of 2.66 * 10^{-6} [Janetti, M.B. 2016].

Adding the Schirmer equation caused all temperature values of wall 2 to improve (see table 6.4). The results of wall 4 only improved at the positions near the external boundary (see table 6.5).

Improving boundary conditions

The differences between the Delphin model and the COMSOL model inside the material are small. The remaining deviations are likely caused by differences in the boundary conditions.
The following boundary equation for heat is used by Goesten, S. [2016]:

$$h_e \cdot (T_e - T_s) + L_v \cdot \beta_e (p_e - p_s) + L_v \cdot \left(k_g (\nabla p_a) \cdot \rho_a \cdot \rho_v \cdot (p_s - p_e)\right) + k_g \cdot (\nabla p_a) \cdot \rho_a \cdot c_a \cdot (T_s - T_e)$$

For moisture the Goesten, S. [2016] uses the following equation:

$$\beta_e (p_e - p_s) + k_g (\nabla p_a) \cdot \rho_a \cdot \rho_v \cdot (p_s - p_e)$$

From the previous chapter, the following boundary equation is proposed for heat:

$$h_e \cdot (T_e - T_s) + L_v \cdot \beta_e (p_e - p_s) + L_v \cdot \left(k_g (\nabla p_a) \cdot \rho_v \cdot \langle \begin{matrix} p_e \\ p_s \end{matrix} \right) + k_g \cdot (\nabla p_a) \cdot \rho_a \cdot c_a \cdot \langle \begin{matrix} T_e \\ T_s \end{matrix}$$

From the previous chapter, the following boundary equation is proposed for moisture:

$$\beta_e (p_e - p_s) + k_g (\nabla p_a) \cdot \rho_v \cdot \langle \begin{matrix} p_e \\ p_s \end{matrix}$$

The choice between p_e/p_s and T_e/T_s is dependent at the direction of the airflux [Hagentoft, C.E. 2004].

Adapting the boundary conditions caused an improvement of the relative humidity for most positions of wall 2 (see table 6.6). Wall 4 showed mixed improvements (see table 6.7).
The results (see figure 6.2 and 6.3) show good similarity.

Table 6.2 Comparison between the simulations of wall 2 with Delphin and the COMSOL model with implemented convection from Goesten, S. [2016].

	Temperature		Relative humidity	
Position	RMSE	Max error	RMSE	Max error
40mm	0.5121	0.4067	0.3416	0.4929
80mm	0.4026	0.2889	0.5355	0.6824
120mm	0.2473	0.2102	0.6631	0.7753

Table 6.3 Comparison between the simulations of wall 4 with Delphin and the COMSOL model with implemented convection from Goesten, S. [2016].

	Temperature		Relative humidity	
Position	RMSE	Max error	RMSE	Max error
7mm	0.1383	0.1615	0.4087	1.1534
47mm	0.1255	0.0997	0.4711	0.6816
87mm	0.1068	0.0797	0.4555	0.4290
127mm	0.0823	0.0888	0.6036	0.5852
167mm	0.1026	0.1053	0.8074	0.6632

Table 6.4 Comparison between the simulations of wall 2 with Delphin and the COMSOL model with implemented convection. Improvement due to adding Schirmer equation in green.

	Temperature		Relative humidity	
Position	RMSE	Max error	RMSE	Max error
40mm	0.5093	0.3788	0.4379	0.5840
80mm	0.3876	0.2569	0.5740	0.8103
120mm	0.2364	0.2098	0.5612	0.8203

Table 6.5 Comparison between the simulations of wall 4 with Delphin and the COMSOL model with implemented convection. Improvement due to adding Schirmer equation in green.

	Temperature		Relative humidity	
Position	RMSE	Max error	RMSE	Max error
7mm	0.1378	0.1394	0.2951	1.5831
47mm	0.0898	0.0669	0.2401	0.3973
87mm	0.0724	0.0547	0.2975	0.4153
127mm	0.0612	0.0655	0.2676	0.3561
167mm	0.0948	0.1108	0.3376	0.6011

6.1.2 Model with seperate convective flux

Rafidiarison, H. et al [2015] measured the air pressure difference (∇p_a) over the whole construction. With ∇p_a representing the air pressure difference between p_i - p_e.
The lack of a seperatly calculated air flux is a shortcoming of the model with implemented convective flux. In this model ∇p_a is implemented as a boundary condition, however this is an overestimation of the pressure difference.
In the model with seperate convective flux, the air pressure difference is calculated using a PDE coefficient instead of estimating it through the moisture boundary conditions. In this model only the difference in air pressure between the ambient air and the surface (p_i - p_s and p_s - p_e) are applied at the boundaries.

As is visible in table 6.8 (wall 2) and table 6.9 (wall 4) the results of the model with seperate flux are in most cases worse than the results of the model with implemented flux. The error of the air pressure is largest at the external boundary. As the RMSE indicates, the mean value is nearly exact.
The results from Delphin shows larger peaks than the results from Comsol. It was expected that this is caused by an inaccuracy in Delphin. However, changes in the solver settings of Delphin didn't improve the results.

Table 6.6 Comparison between the simulations of wall 2 with Delphin and the COMSOL model with implemented convection. Improvement due to adding other boundary equations in green.

	Temperature		Relative humidity	
Position	RMSE	Max error	RMSE	Max error
40mm	0.4225	0.2386	0.4911	0.6253
80mm	0.4421	0.2892	0.5416	0.7078
120mm	0.2892	0.2129	0.4064	0.5773

Table 6.7 Comparison between the simulations of wall 4 with Delphin and the COMSOL model with implemented convection. Improvement due to adding other boundary equations in green.

	Temperature		Relative humidity	
Position	RMSE	Max error	RMSE	Max error
7mm	0.1415	0.1936	0.3149	0.9002
47mm	0.0983	0.1428	0.2347	0.4008
87mm	0.0944	0.2236	0.2967	0.4175
127mm	0.1099	0.5501	0.2708	0.3552
167mm	0.1945	1.3784	0.3476	0.7912

Table 6.8 Comparison between the simulations of wall 2 with Delphin and the COMSOL model with seperate convection. Improvement due to seperating the air flux in green.

	Temperature		RH		Air pressure	
Position	RMSE	Max error	RMSE	Max error	RMSE	Max error
40mm	0.5176	0.2933	0.6645	0.8962	0.0006	6.9279
80mm	0.5422	0.3635	0.7996	1.0805	0.0004	4.6158
120mm	0.3678	0.2815	0.6492	0.9366	0.0002	2.2949

Table 6.9 Comparison between the simulations of wall 4 with Delphin and the COMSOL model with seperate convection. Improvement due to seperating the air flux in green.

	Temperature		RH		Air pressure	
Position	RMSE	Max error	RMSE	Max error	RMSE	Max error
7mm	0.3270	0.2628	0.4182	0.9564	0.0003	2.8713
47mm	0.2220	0.1445	0.2180	0.2873	0.0002	2.4032
87mm	0.1862	0.1340	0.2921	0.3613	0.0002	2.1162
127mm	0.1496	0.1519	0.4576	0.5760	0.0002	1.7340
167mm	0.1547	0.1676	0.6750	0.9300	0.0001	1.2487

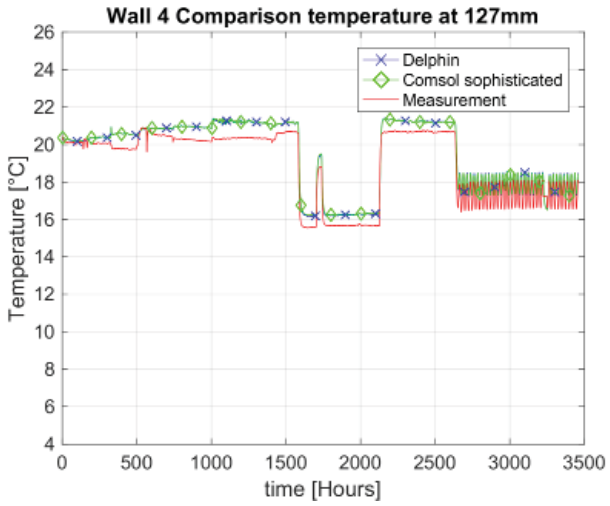

Figure 6.2 Comparison of temperature between Delphin and COMSOL with improved boundary conditions. The measurements are also included to see if the results are somewhat reliable.

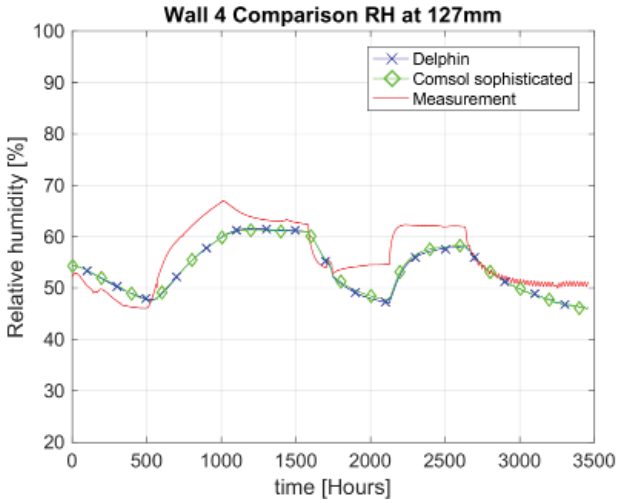

Figure 6.3 Comparison of RH between Delphin and COMSOL with improved boundary conditions. The measurements are also included to see if the results are somewhat reliable.

6.2 Comparison with measurements

In figure 6.2 - 6.3 the measurements were already included. Using material data solely from Delphin, results in differences between the simulations and the measurements. These differences are comparable to the differences found by Goesten, S. [2016].
Goesten, S. [2016] used a hybrid of altered material data from Delphin and data mentioned by Rafidiarison, H. et al. [2015].

The following material properties are necessary for the simulations:
- sorption isotherm ($w(\varphi)$);
- water vapour diffusion (μ);
- liquid permeability (k_l);
- thermal conductivity (λ).

To make a good comparison between the Comsol simulations and the measurements, the material properties in the Comsol model (originating from the Delphin database) are replaced by the material properties mentioned in [Rafidiarison, H. et al. 2015].
The paper provides material data. However, some material data is insufficient or missing, as is visualized in table 6.10.

6.2.1 Material data

Sorption isotherm

Rafidiarison, H. et al. [2015] mentions both the adsorption and desorption properties of each material, where Delphin assumes a single sorption term for each material (thus not including hysteresis). At various humidity levels the adsorption and desorption properties are measured.
Using a non-lineair regression method it's possible to define a continuous curve. The produced curves can then be fitted for the hygroscopic region - using a GAB model for instance - [Lelievre, D. 2014].

The moisture content from Goesten, S. [2016] and Delphin is expressed as volume percentage [m^3/m^3]. Rafidiarison, H. et al. [2015] uses mass percentage [kg/kg]. Both are related using the mass of water [Wit, M. 2009][Adan and Samson, 2011]:

$$\rho \cdot u = 100 \cdot w = 1000 \cdot \psi$$

ρ = mass of material [kg/m^3]
u = mass percentage of moisture [kg/kg]
w = mass percentage of moisture per volume material [kg/m^3]
ψ = volume percentage of moisture [m^3/m^3]

A comparison between the data used by Goesten, S. [2016], the original Delphin material data and the curves produced from the measured values by Rafidiarison, H. et al. [2015] is visible in figure 6.4 for OSB. For the other materials see Appendix V.

The adsorption and desorption curves for wood fibre board (originating from Vololonirina, O. [2014]) are in the same order of magnitude as the sorption curve used by Goesten, S. [2016].
This doesn't hold for OSB and lime plaster, where the adaptions of Goesten, S. [2016] even increased the difference between the original Delphin materials and the properties mentioned by Rafidiarison, H. et al. [2015].

When hysteresis is included in the model, the complexity is increased and more accurate results can be obtained [Colinart, T. 2016][Zhang, X. 2016]. This is beyond the scope of this paper. Therefore the average of the adsorption and desorption curve will be used as sorption curve in the simulations (see proposed sorption in figure 6.4).

Table 6.10 Availability of material properties in [Rafidiarison, H. et al. 2015].

	lime plaster	wood fibre board*	OSB*
$w(\varphi)$	ads-des	ads-des	ads-des
μ	single-value	dry-/wet cup	dry-/wet cup
k_l	-	dry-/wet cup	dry-/wet cup
λ	single-value	f(Lpc,T)	f(Lpc,T)

*extracted from [Vololonirina, O. 2014].

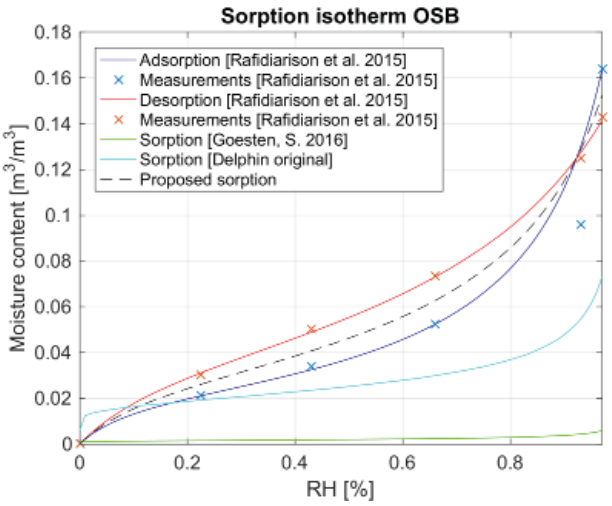

Figure 6.4 Sorption isotherm for OSB that Goesten, S. [2016] used, compared to the original data from Delphin, the measurements by Rafidiarison, H. et al. [2015] with the fitted curves produced using a non-linear regression method.

Water vapour diffusion

Water vapour diffusion is a material property that heavily depends at the moisture content of a material, which has also been mentioned in the previous chapter (equation 1.5-1.7).

Rafidiarison, et al. [2015] again used the material properties from Vololonirina, et al. [2014] for OSB and wood fibre board. The properties for the lime plaster are obtained from self performed measurements.
Vololonirina, et al. [2014] measured the OSB and wood fibre board coming from a dry and a wet state (comparible to the measurement of the adsorption and desorption curve) and performed both a dry- and wet cup measurement.
Goesten, S. [2016] used the material properties from Delphin for OSB (lowered it with 95) and lime plaster (original). For the wood fibre board a single-value was used.
Large differences occur for the OSB material between the material used by Goesten, S. [2016] and the material measured by Vololonirina, et al. [2014] (see figure 6.5). First the values aren't in the same order of magnitude and second the slopes are each others opposite.
The lime plaster and wood fibre board are in the same order of magnitude as the properties used by Goesten, S. [2016] (see appendix V).

The low amount of measured values by Rafidiarison, et al. [2015] and Vololonirina, et al. [2014] are not ideal. However, the influence of diffusion is relatively small compared to the convective moisture transfer.

Liquid permeability

The liquid permeability of the material has a large influence at the results. The liquid permeability of a material is strongly dependend at the moisture content [Berger, J. 2014] (see figure 6.6). And it is a significant parameter for high relative humidities [Belleudy, C. 2015].
Colinart, T. [2016] mentions that wet cup measurements alone aren't enough calculate the liquid transport.
Using the measurements of Vololonirina, et al. [2014] (that has both a wet- and dry cup measurement) there's still hardly any moisture dependence.
The moisture curve used by Goesten, S. [2016] however, shows a good moisture dependancy.

6.2.2 Results

The simulations with the original material properties have been performed using the Comsol model with seperate convective flux. All results are visible in Appendix VI. The results show that any relation to the measurements has dissapeared. The earlier performed simulations with Delphin materials (see figure 6.2 and 6.3) even have a better relation to the measurements.
The measured material properties (in particular the liquid permeability) by Vololonirina, et al. [2014] appear to be insufficiënt to perform reliable simulations.

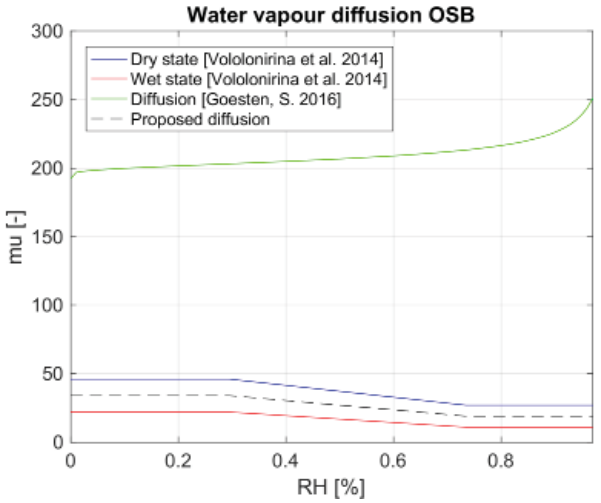

Figure 6.5 Water vapour diffusion for OSB that Goesten, S. [2016] used, compared to the measurements by Vololonirina, et al. [2014].

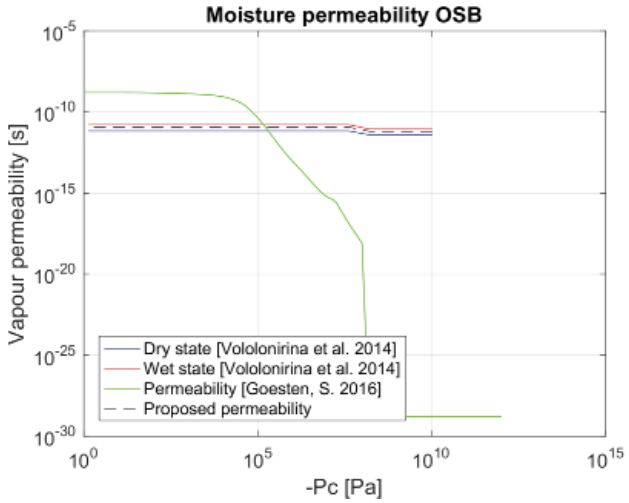

Figure 6.6 Liquid permeability for OSB that Goesten, S. [2016] used, compared to the measurements by Vololonirina, et al. [2014].

7 Case study

The case study - a multi-storey building in Copenhagen Denmark - is based at the construction measured and simulated by [Harrestrup, M. & Svendsen, S. 2016]. The walls of this building consist of masonry and are to a certain extent comparable to the (massive) masonry walls built in the Netherlands. The thickness of the walls is 1,5 - 2 stones.

The case study consists of three parts (see appendix VII)
- Chapter 7.2.1: indoor climate;
- Chapter 7.2.2: Insulation type;
- Chapter 7.2.3: Construction type.

For each part different scenarios are simulated which are further elaborated below.

7.1 Validation

The COMSOL model was already validated for a 1D construction type at chapter 6. In this chapter a validation is performed with a 2D construction. The COMSOL model is validated with measeruments performed by Harrestrup, M. [2016].

The original construction consists of a masonry wall with a thickness of 2 bricks (see figure 7.1). The load bearing beam inside the wall has a diameter of 150x150mm. The floor beam has a height of 140mm and is surrounded by an air layer of 20mm. The cladding and the plaster are both 30mm thick.

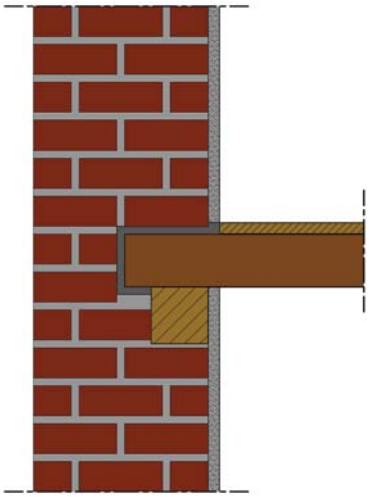

Figure 7.1 Danish construction used by [Harrestrup, M. 2016].

The size of the bricks and the thickness of the lime-cement mortar is 220x100x80mm (LxWxH) and 20 mm respectively.
The validation has been performed for the insulated construction (see figure 7.2). The insulation with a thickness of 40mm consists of a mixture of mineral wool with an aerogel. At the interior side of the insulation a vapour barrier has been applied (μd = 2.0m), finished with an gypsum board of 12mm (for material properties, see table 7.1).
For the external climate no measurement data was available, therefore a Danish reference year is used. Included parameters are: ambient temperature, relative humidity, wind-driven-rain (calculated with equation 1.17, the coefficients mentioned in chapter 5.5.3 and $\kappa = 0.3$) and solar radiation.
The indoor temperature and relative humidity have been measured. These measurements are used as input parameters for the model.
There are no air pressure measurements, therefore this isn't included into the COMSOL model.
After the first exploratory simulations, three necessary adaptions were made to the model. First, the air layer around the wooden beam end has been replaced by lime-cement mortar. Second, the solar radiation hasn't been included.
Inclusion of the air layer and/or solar radiation lead to the inability to converge.
Third, the material properties of the insulation material couldn't be exported properly from Delphin. EPS is an insulation material that has similar properties as the combination of the insulation material and the vapour barrier. The heat capacity (c) and thermal conductivity (λ) are adapted to meet the same values as mentioned by Harrerstrup, M. [2016].
It is expected that the adaptions mentioned above result in lower temperatures and higher humidity levels than in reality.
Harrestrup, M. [2016] has performed temperature and relative humidity measurements at a single position in the wooden beam (see figure 7.2).

Table 7.1 Material properties used for the COMSOL simulations

Material properties	Unit	Masonry	Lime mortar	Lime plaster	Spruce (wood)	Gypsum board	EPS	XPS	Calcium silicate
Density	[kg/m^3]	1788	1568	1800	528	850	23	35	270
Specific heat capacity	[J/kg·K]	868	1000	850	2000	850	1500	1500	1158
Thermal conductivity	[W/m·K]	0.91	0.70	0.82	0.13	0.20	0.036	0.027	0.069
Water vapour resistance	[-]	13.2	30	12	40	10	96	225	3.85
Liquid permeability	[kg/m·s·Pa]	$1.4 \cdot 10^{-8}$	$6.5 \cdot 10^{-10}$	$2.8 \cdot 10^{-9}$	$4 \cdot 10^{-9}$	$6.3 \cdot 10^{-9}$	-	-	$2.34 \cdot 10^{-8}$
Air permeability*	[kg/m·s·Pa]	$5 \cdot 10^{-10}$	$1.5 \cdot 10^{-9}$	$1 \cdot 10^{-11}$	$5 \cdot 10^{-11}$	$4.16 \cdot 10^{-9}$	$1.1 \cdot 10^{-8}$	-	$1.38 \cdot 10^{-7}$

** Properties based at measurements from ASHREA RP1018*

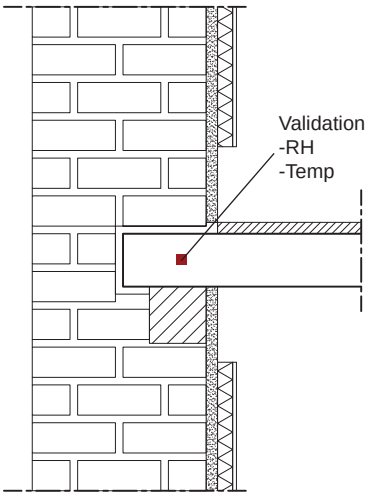

Figure 7.2 Position of the measurements. Also used for the comparison with the simulation model.

The measurements were available from 15-05-2013 to 10-02-2014. For this period of time both the temperature and the relative humidity are compared (see figure 7.3 & 7.4).
Both figures show a large deviation between the measured and simulated temperature and humidity values. The trend, however, is similar.
As expected the temperature of the simulation is lower due to the absence of solar radiation. The relative humidity, which is also temperature dependend, is higher than the measurements. A lower initial humidity value could already improve these results.

7.2 Simulations for the Netherlands

The validated 2D model is adapted. Instead the construction now has dimensions that are common in Dutch constructions.
The brick size is changed to 210x100x50mm (LxWxH) and the lime-cement mortar has an adapted thickness of 10mm (see figure 7.5).
The external climate depends at the geographical position of the building.The Danish climate data, is replaced by Dutch climate data. According to the RCE (Cultural Heritage Agency) most monumental buildings in The Netherlands are located in the province 'Noord-Holland'. Within this province the cities Amsterdam and Haarlem contain most monumental buildings.

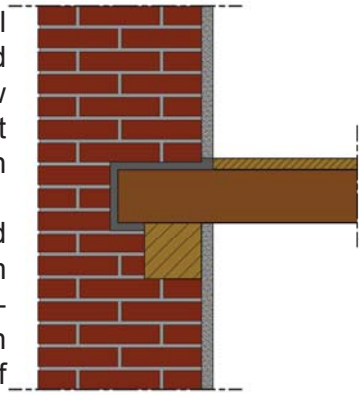

Figure 7.3 Adapted common Dutch construction used for the simulations in this report.

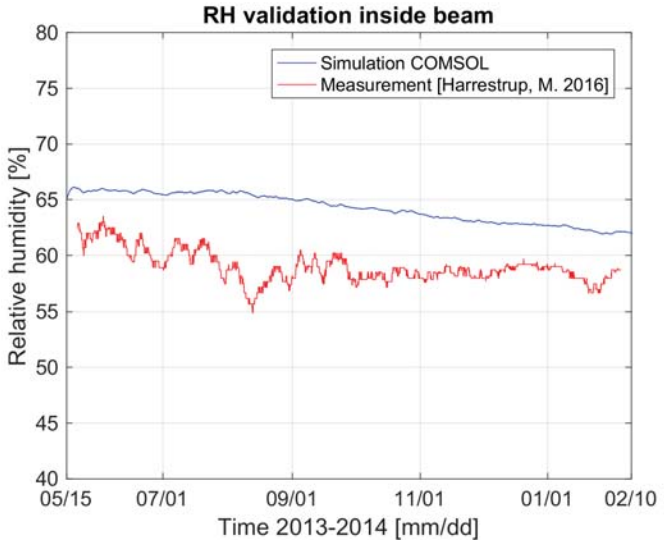

Figure 7.4 Relative humidity in the wooden beam at the position as visualised in figure 7.2. A comparison between the measurements (red) with the simulation in COMSOL (blue).

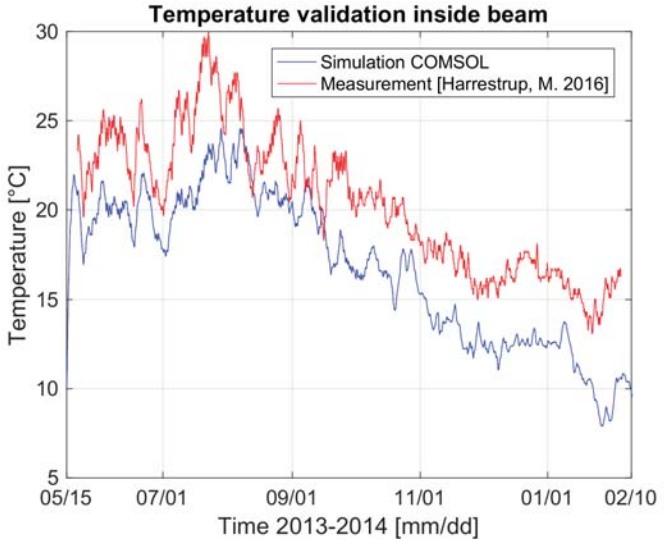

Figure 7.5 Temperature in the wooden beam at the position as visualised in figure 7.2. A comparison between the measurements (red) with the simulation in COMSOL (blue).

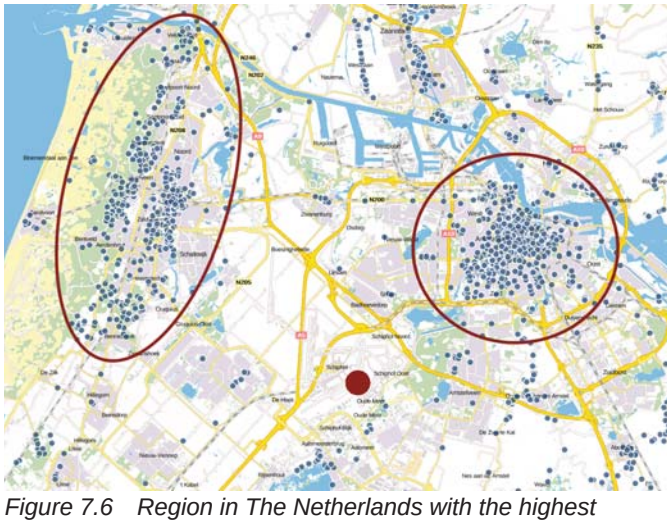

Figure 7.6 Region in The Netherlands with the highest density of monumental buildings: Amsterdam (right circle) and Haarlem (left circle). The nearest Meteorological station is Schiphol (red dot) [RCE, 2016].

As seen in figure 7.6 the KNMI has a Meteorological station near these cities. The measured climate data from this station are applied to the external boundaries. The simulated year is 2012. Which is one year before the measurements in Denmark were performed by Harrestrup, M. [2016]. In 2012 the average temperature over the year deviates only 0.2°C from the long term average. It contains a very cold period at the start of the year and a warm period near the end of the summer. With 876 mm the precipitation amount is somewhat higher than than the long term average of 849 mm.
The uninsulated wall is used as the starting situation. It is assumed that no moisture buildup occurs in this situation, which means that the uninsulated construction is safe and also no mould or deterioration of the wood occurs.
The air pressure difference between indoor and outdoor is estimated with the calculation of the stack-effect (equation 1.46). The calculation assumes a temperature and gravitational based pressure difference. With an overpressure situation at the interiour.
Initial values used for all simulations are 10°C and a RH of 65% for the whole contruction.

7.2.1 Indoor climate

At first the influence of the indoor climate at the moisture safety of wooden beam ends is investigated.

Simulation settings

Two different indoor climates are used for this comparison: A museum climate with a constant temperature of 20°C and a RH of 50% throughout the year; And a dwelling climate, calculated with HAMBASE.
The indoor climate is depending at the outdoor climate, construction and indoor setpoints. All are inserted into the HAMBASE model and the resulting indoor climate is used as input for the COMSOL model (see Appendix VII for the trend of the indoor climate).
The internal gains and ventilation rate used for the HAMBASE calculation are based at the ISSO 2008 and Dutch building standard respectively.
The COMSOL simulations are performed for the uninsulated original construction and for a fully insulated wall at the interiour. EPS is used as insulation material with a thickness of 100mm. At the interiour side of the insulation gypsum board is applied with a thickness of 12mm.

Results

In figure 7.7 and 7.8 the analysed positions are visualised. At these positions the RH is calculated. Also the whole surface of the wooden beam is analysed. Using COMSOL the highest moisture content has been searched.
In figure 7.9 the RH distribution is visualised. Near the end of the wooden beam, highest humidity values are reached.
The maximum moisture content in the wooden beam (see figure 7.9) is highest for the insulated wall (see appendix IX for the summer situation).

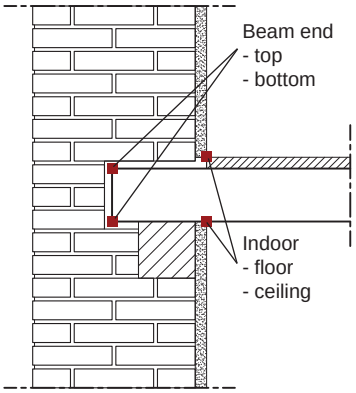

Figure 7.7 Position of the results for the uninsulated wall

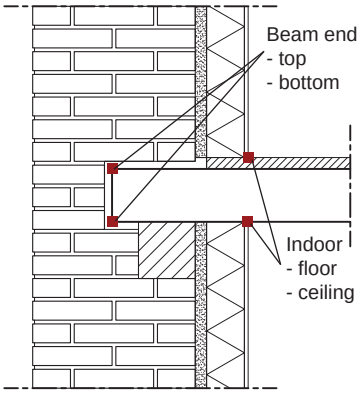

Figure 7.8 Position of the results for the insulated wall

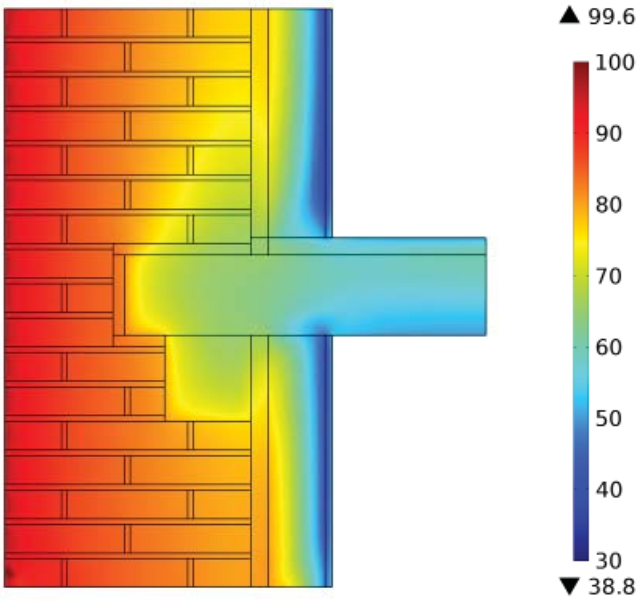

Figure 7.9 RH distribution within the construction and the museum indoor climate, during a rain event at 29-12-2012.

For both the dwelling and the museum indoor climate the moisture content after one year is almost similar, difference <0,1% (see figure 7.10). In all situations moisture buildup occurs.
In the summer the museum climate appears to be most critical. Highest deviation between the two different indoor climates are also found in this season.
During the summer, the indoor temperature of the museum remains 20°C while the indoor temperature of the dwelling reaches values up to 34°C, due to the absence of cooling.

The relative humidity at the surface of the beam end (figure 7.11) shows a similar trend as the moisture content. The insulated situation shows relative humidity values higher than 80% (the threshold for mould growth). Also here the museum climate shows the highest values during summer.

At the indoor surface the RH shows large variations for the dwelling (see figure 7.12) in a short period of time. These variations are in agreement to the temperature variations of the indoor climate as seen in Appendix VII.
For the museum climate the RH at the surface shows less variance (see figure 7.13). During winter the air needs to be humidified and during summer dehumidification is needed to maintain a RH of 50% at a temperature of 20°C, due to the low absolute humidity of the outdoor air. Changes in humidity are well visible, as the RH of the museum is higher during winter and lower during summer than that of the dwelling.
At the interior surface none of the simulations reach relative humidity values above 80%.

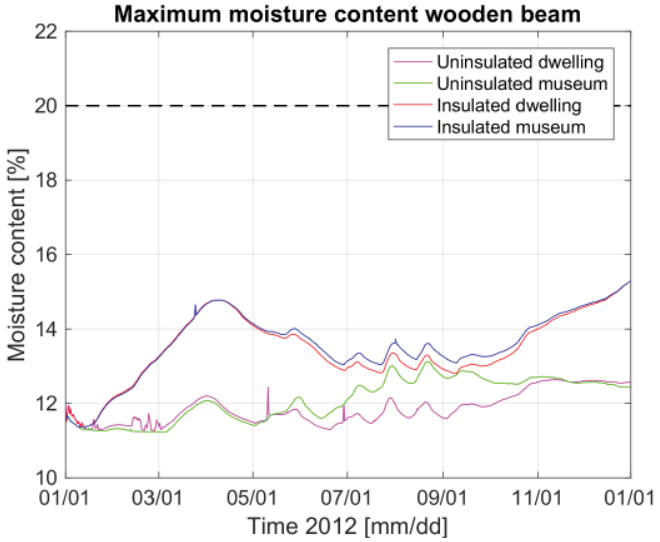

Figure 7.10 Highest moisture content found in the wooden beam in mass percentage [%]. The uninsulated situation with dwelling (blue) and museum (red) climate is compared to the insulated situation with a dwelling (magenta) and museum (green) climate.

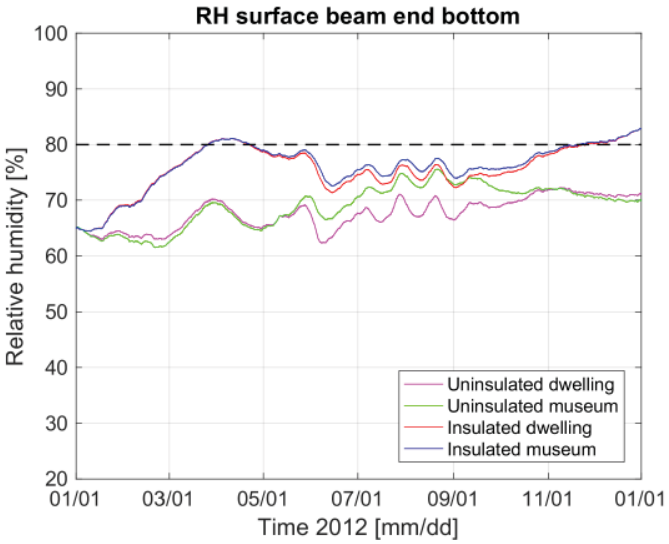

Figure 7.11 RH at the surface of the wooden beam end. The uninsulated situation with a dwelling (magenta) and museum (green) indoor climate is compared to the insulated situation with dwelling (red) and museum (blue) indoor climate.

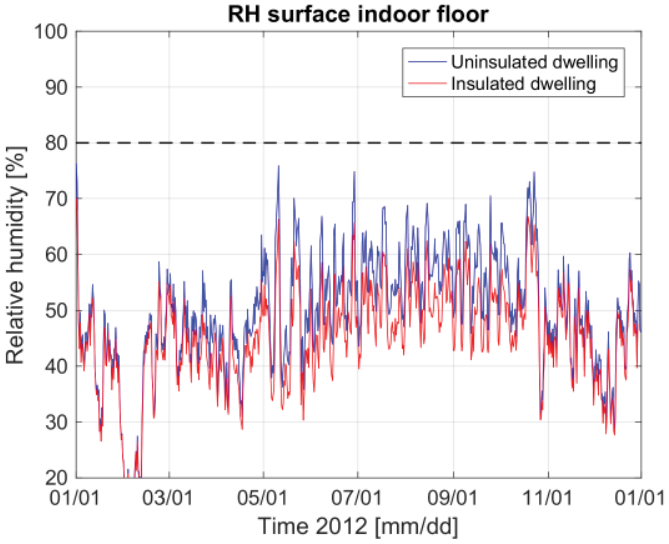

Figure 7.12 RH at the indoor surface. The uninsulated situation with a dwelling climate (blue) is compared to the insulated situation with a dwelling climate (red).

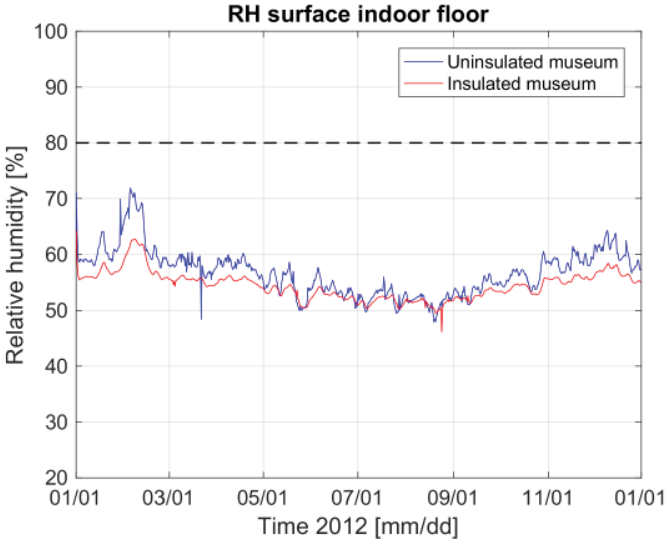

Figure 7.13 RH at the indoor surface. The uninsulated situation with a museum climate (blue) is compared to the insulated situation with a museum climate (red).

7.2.2 Insulation type

The second setup is used to determine the influence of applying different insulation materials.

Simulation settings

The simulations are performed for the original construction (uninsulated) and a fully insulated wall at the interiour. The insulation thickness is 100mm. At the interior side of the insulation gypsum board with a thickness of 12mm is applied.

The following variants are simulated:
- EPS;
- XPS;
- Calcium silicate board.

The material properties are extracted from the Delphin material database. For both EPS and XPS there is no liquid permeability taken into account. XPS also isn't permeable when it comes to air transport.

The most critical indoor climate is used from chapter 7.1.3. Which is the museum climate.
Calcium Silicate is the only insulation material in this comparison that is active when it comes to moisture permeability. Also the vapour permeability of this material is lowest.

Results

In figure 7.7 and 7.8 the analysed positions are visualised.
Calcium Silicate causes the highest moisture content in the wooden beam (see figure 7.14)
XPS insulation results in the lowest moisture content in the wooden beam. The difference between the EPS and XPS insulation, however, remains below a mass percentage of 1%.
Also after one year the moisture content is up to 3-4% higher than at the start of the year for all insulation types compared to the uninsulated wall.

The trend for the RH at the beam end is similar as the one of the moisture content (see figure 7.15). Highest values are again found with Calcium Silicate applied. For all insulation types, the RH at the beam end reaches the 80% value. Indicating there's a risk at mould growth.
At the indoor surface an important difference is noticable (see figure 7.16). With EPS and XPS applied, the RH is lower than the uninsulated situation. The Calcium Silicate causes the RH to be higher than the uninsulated construction. However, the calcium silicate also results in a more stable humidity level at the indoor surface. Indicating that short variations in humidity can be absorbed.

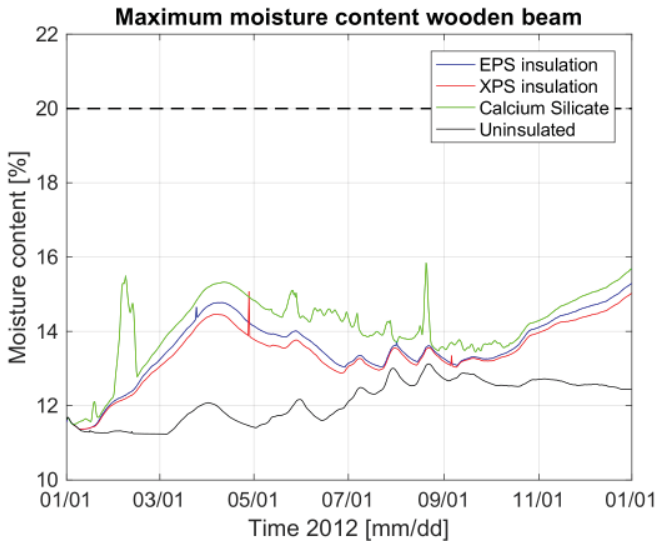

Figure 7.14 Highest moisture content found in the wooden beam in mass percentage [%]. Uninsulated (black) is compared to insulated with EPS (blue), XPS (red) and Calcium Silicate (green).

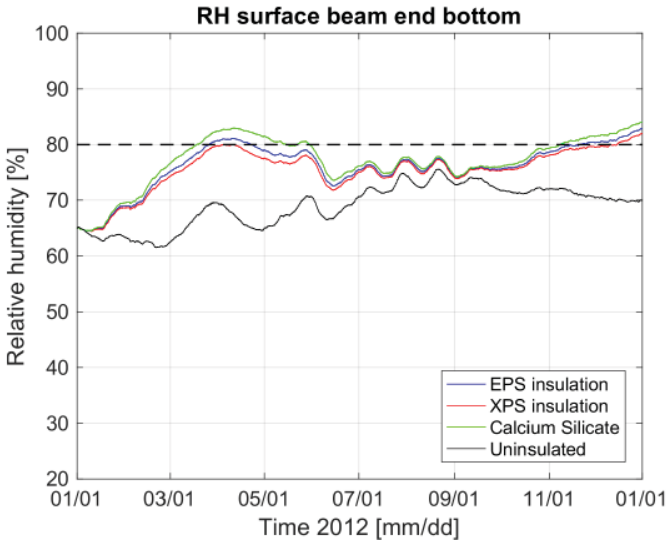

Figure 7.15 RH at the surface of the wooden beam end. Uninsulated (black) compared to the insulated with EPS (blue), XPS (red) and Calcium silicate (green).

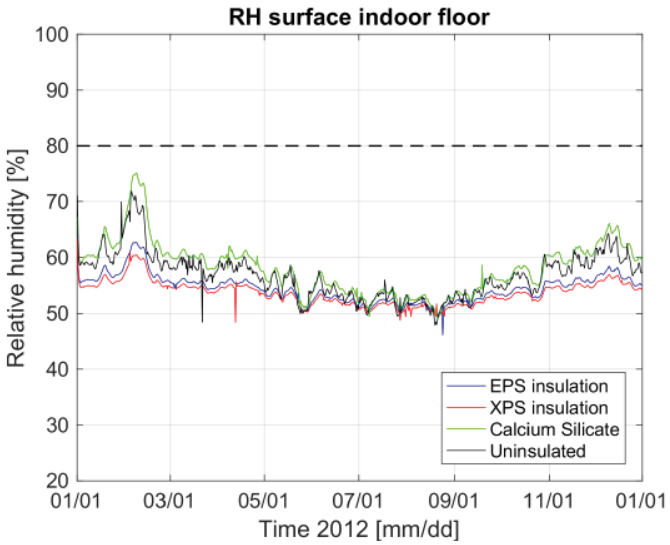

Figure 7.16 RH at the indoor surface. Uninsulated (black) is compared to insulated with EPS (blue), XPS (red) and Calcium Silicate (green).

7.2.3 Construction type

The influence of changing the construction of the insulation is also investigated.

Simulation settings

The simulations are performed for the original construction (uninsulated), a fully insulated wall at the interiour, an insulated wall with a gap of 200mm around the wooden beam and an insulated wall with a gap of 100mm at the connection to the floor, where active heating is applied.
The insulation thickness is 100mm. In all cases EPS is applied. At the interior side of the insulation, gypsum board with a thickness of 12mm is applied. The heating is activated when the outdoor temperature drops below 10°C. With a water temperature of 35°C in the heating system, it is assumed that the air temperature near the wall and floor reaches a temperature of 30°C.

Results

In figure 7.17 and 7.18 the analysed positions are visualised. For the moisture content (see figure 7.21) The results of a change in construction already look promising when compared to the other categories. The moisture increase due to adding full insulation is halved when active heating is applied. This is also visible in figure 7.19, where the humidity is lower near the interior than the fully insulated construction from figure 7.9 (see appendix IX for the summer situation).
The best result is achieved when a 200mm gap is applied. There the moisture content deviates < 1% from the uninsulated construction.

The positive effect of heating is also visible for the RH values at the surfaces. All analysed positions are included in figure 7.22 - 7.25. In none of the positions a RH higher than 80% has been reached. The RH shows the best improvement at the indoor surface and the top of the wooden beam end. There is also a positive effect noticable at the bottom of the wooden beam end, however the coverage of the active heating remains limited compared to the insulation gap of 200mm.

For the construction with a 200mm gap at the surface of the beam end, a significant improvement has been found. However, the downside to this construction appears to be the inside surface that has higher RH values than the uninsulated wall. While the fully insulated wall with EPS caused an improvement as described at chapter 7.2.2.

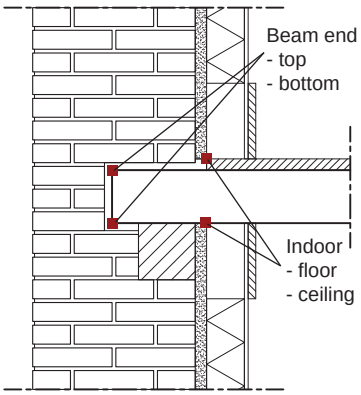

Figure 7.17 Position of the results for the insulated wall with 200mm insulation gap around the wooden beam.

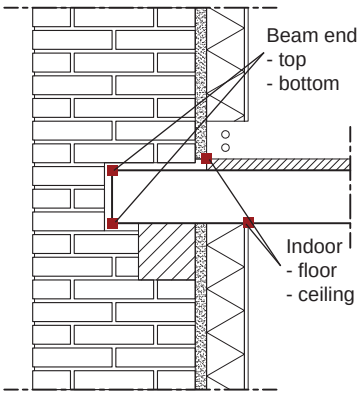

Figure 7.18 Position of the results for the insulated wall with active heating at the wooden beam.

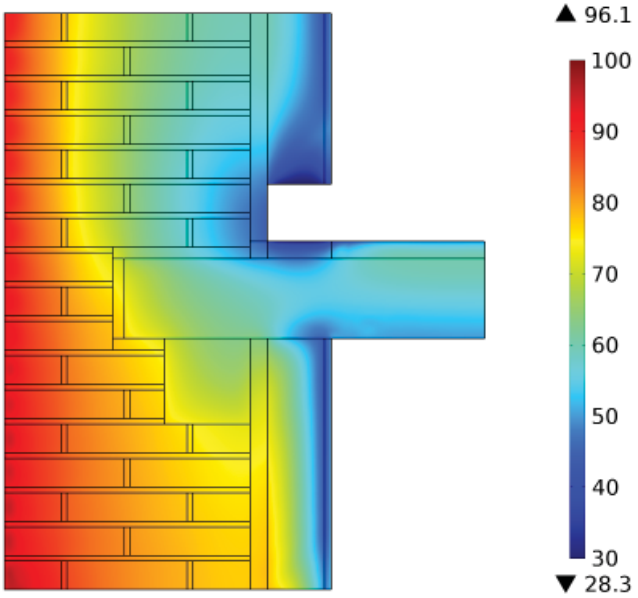

Figure 7.19 RH distribution within the construction and the active heating at the gap, during a rain event at 29-12-2012.

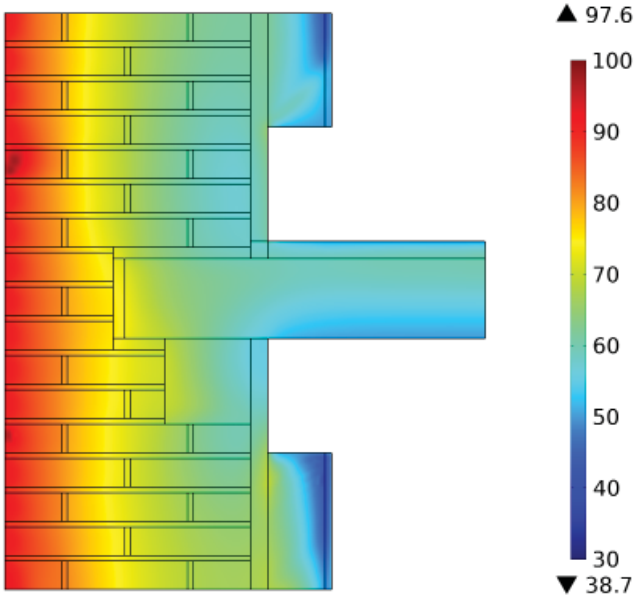

Figure 7.20 RH distribution within the construction and the insulation gap of 200mm, during a rain event at 29-12-2012.

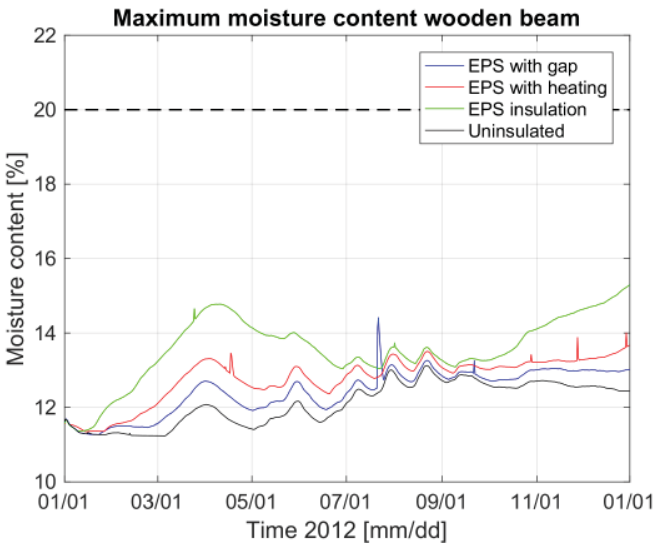

Figure 7.21 Highest moisture content found in the wooden beam in mass percentage [%]. The uninsulated situation (black) is compared to the fully insulated situation (green), a 200mm insulation gap (blue) and active heating (red).

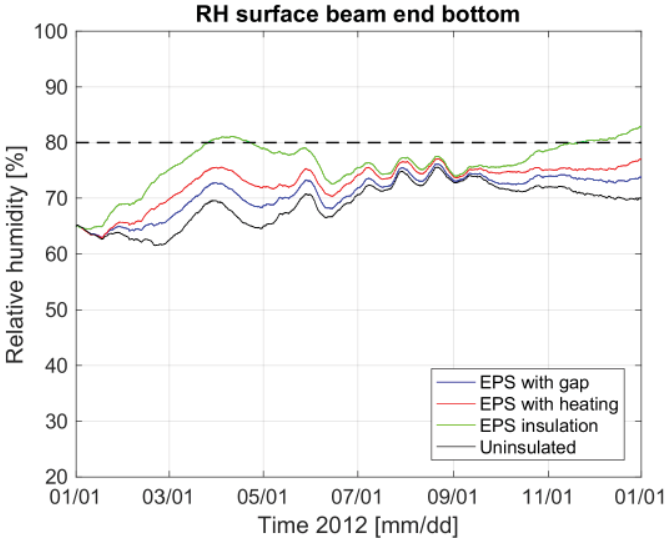

Figure 7.22 RH at the bottom surface of the wooden beam end. The uninsulated situation (black) is compared to the fully insulated situation (green), a 200mm insulation gap (blue) and active heating (red).

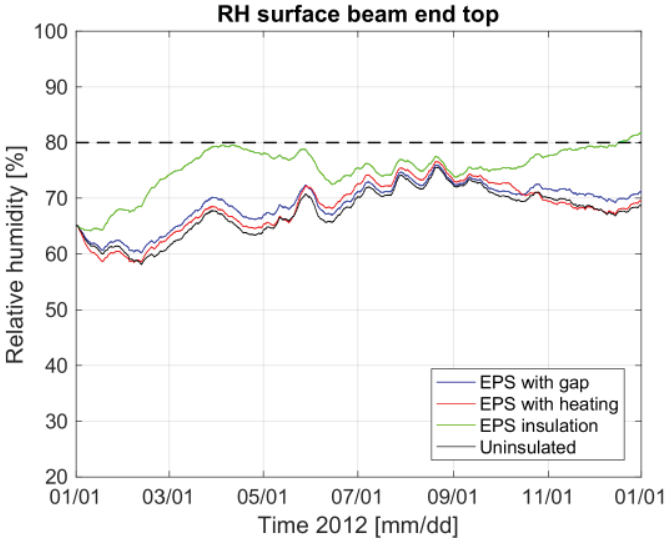

Figure 7.23 RH at the top surface of the wooden beam end. The uninsulated situation (black) is compared to the fully insulated situation (green), a 200mm insulation gap (blue) and active heating (red).

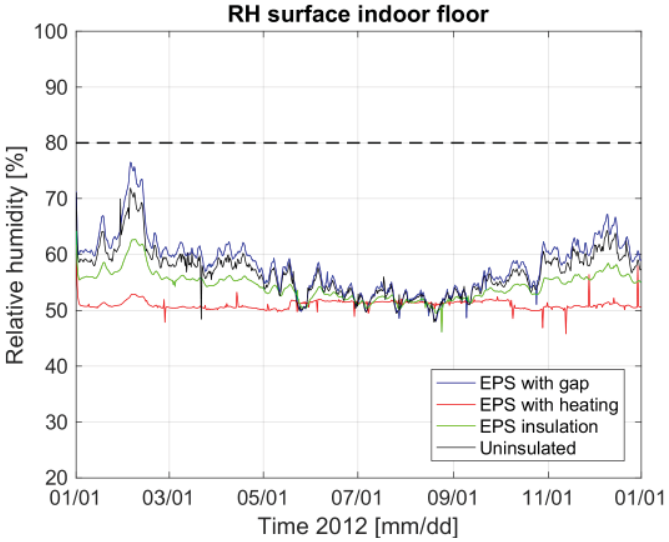

Figure 7.24 RH at the indoor surface. The uninsulated situation (black) is compared to the fully insulated situation (green), a 200mm insulation gap (blue) and active heating (red).

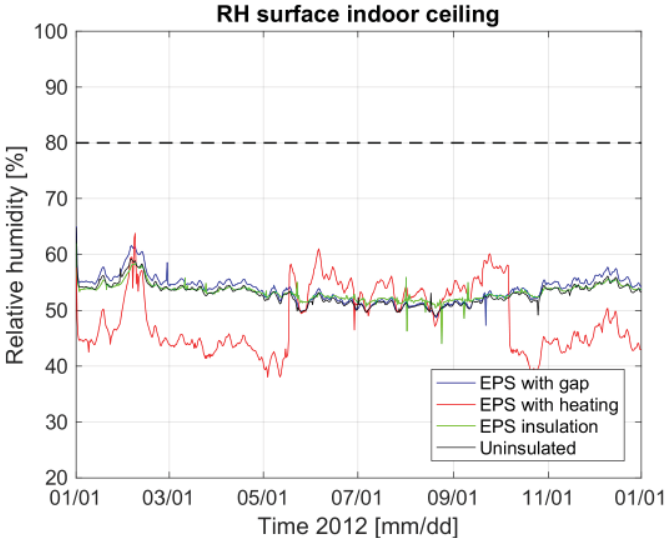

Figure 7.25 RH at the indoor surface. The uninsulated situation (black) is compared to the fully insulated situation (green), a 200mm insulation gap (blue) and active heating (red).

8 Discussion

The COMSOL and Delphin models are compared in 1D. Even after there weren't any noticable differences between the input parameters of the models, a small error remained.
The remaining error could be caused by a difference in moisture potential. A difference also found by [Janssen, H. 2014] while comparing the potentials Lp_c (COMSOL model in this research) and p_c (Delpin model in this research).
After the 1D validation, the model is used for 2D simulations of a wooden beam end connected to a wall. [Harrestrup, M. 2016] has performed measurements and thereafter simulations with Delphin of this construction.

The 2D simulation in COMSOL has been validated with the measurements performed by [Harrestrup, M. 2016]. The simulation results and the measurements did not align. The inability to include solar radiation into the model is most likely the cause of the unalignment.
Also the air layer couldn't be simulated - instead lime mortar is used - and no measurement data from the external climate was available.

Due to the differences between the simulation results and the measurements, a 2D validation with the Delphin model from Harrestrup, M [2016] is desired.
A 2D validation of the COMSOL model with the 2D Delphin model from Harrestrup could not be performed due to several reasons. The material data of the Mineral wool (directly extracted from Delphin) proved to be incorrect. The applied boundary conditions in the Delphin model weren't available. Thus no replication of the simulation by Harrestrup, M. [2016] was possible.
Aside from the missing validation of the 2D COMSOL model, there are some other limitations to this study.

The following simplifications and assumptions are made regarding the 2D simulations of a wooden beam end connected to a wall:

- Material properties are extracted from Delphin material database. Materials from the database have a single sorption isotherm, thus hysteresis isn't included. Inclusion of hysteresis causes significant differences [Cerny, R. 2009].
- The thermal conductivity (λ) imported from Delphin only depends at the moisture content inside the material. While in reality the thermal conductivity also depends at the temperature.
- Solar irradiance is neglected. Inclusion of this parameter caused errors in the solver.
- Simulation time variated between 3,5 and 18 hours while simulating one year, using a laptop containing an Intel i7-3630QM processor and 8GB RAM. It's preferrable to simulate multiple years to see if a moisture buildup occurs and a critical situation, with a moisture content higher than 20%, can develop over time.
- The connection of the wooden beam end to the external wall is actually a 3D situation. Simulating this in 2D is therefore a limitation.
- The wind driven rain has been calculated using the precipitation amount measured at the meteorological station. However this is an open-field situation. In urban or sub-urban areas there is more shielding from the surroundings. Thus the wind driven rain should be lower at these areas.
- A factor of 0,3 is chosen for the wind driven rain. CFD is needed to determine if this factor is indeed a good estimate.

The validation with the measurements by Harrestrup, M. [2016] could be further improved. However, the best solution is to perform new extensive measurements at a building for at least a year, both without and with insulation.
The comparison with the measurements by Harrestrup could only be performed for temperature and relative humidity. The addition of a continuous moisture content measurement could prove valuable.

Solving a 3D problem in 2D inevatably causes differences. In the 2D simulation the wooden beam end only has direct contact with the interior at the ceiling. While in reality also the sides of the beam are in contact with the interior. From energy perspective this results in a higher energy loss. Or in other terms, the 2D simulation overestimates the thermal bridge and it's effects.

9 Conclusion

How wooden beam ends can be preserved with the use of HAM simulations, while insulating a monumental building.

When deterioration of wood will take place

Wood and especially wooden beam ends beared in walls, have a risk at deteroration when exposed to high humidity levels for longer periods of time. For the moisture mass content and relative humidity, static tresholds above which deterioration and growth of mould/fungi can prevail, are 20% and 80% respectively.

These thresholds aren't arbitrary and should be handled with care. In certain circumstances (high temperatures for instance) mould can grow at relative humity values below 80%.

Accuracy of the COMSOL model using Logarithmic capillary pressure as moisture potential and the differences between different moisture potentials.

Simulations with COMSOL multiphysics are validated in 1D with Delphin. In the COMSOL model logarithmic capillary pressure (Lp_c) is used as moisture potential, while the Delphin model uses capillary pressure (p_c) as potential.

Using similar input variables, both models produced equal results for Heat, Moisture and Air transport - RMSE remains below 1% -.

After this 1D validation, the COMSOL model is used for a comparison with temperature and relative humidity measurements in a wooden beam end connected to a wall. These measurements are performed by Harrestrup, M. [2016].

For the temperature the results from the model and measurements differed <8°C and for the relative humidity <10%.

Possible improvements for the COMSOL model

Some small improvements are made to the existing COMSOL model described by Goesten, S. [2016]. Inclusion of the Schirmer equation improved the accuracy of the vapour permeability (δ_p). Also the implementation of the boundary conditions is changed and now meets the boundary conditions as proposed by Hagentoft, C.E. [2004].

The experience of insulating around wooden beam ends from former research

When insulation is applied at the interior - which is mostly the only applicable position in monumental buildings - a moisture risk is introduced.

Possible solutions to reduce this risk:

Improvement of the air tightness in the construction by adding an extra layer of OSB;

Addition of a vapour resistant layer;

Introducing a 200mm insulation gap around the wooden beam;

Applying active heating (heating pipe) near the wooden beam end. Or use passive heating (heating rod) inside the wooden beam.

Insulating without causing deterioration of wooden beam ends

The autumn and the wintertime are the most critical seasons within a year. The precipitation amounts are high in the autumn, and during the winter the temperature differences between indoor and outdoor increase. The low temperatures of the outdoor climate result in low absolute humidity levels. For a well ventilated and heated dwelling the relative humidity values are around 40% during winter. The museum climate, however, remains at a relative humidity of 50%, even in the winter.

A stable climate, which is present in a museum, proves to be more critical than a climate present in a dwelling.

Insulating a wall from the inside prevents the wall to heat up during the winter and reduces the drying capacity of a wall. The wooden beam end penetrates the insulation layer and forms a thermal bridge. After a single year the moisture level at the wooden beam end has increased significant for both the dwelling and museum indoor climate.

To reduce the moisture level at the wooden beam end, different insulation types can be applied. Three different insulation types are compared: EPS; XPS and Calcium silicate. Simulations are performed with the museum climate (worst-case) and a fully insulated wall at the interior.

It has been found that applying Calcium silicate causes the highest moisture level at the wooden beam end. Thereafter followed by EPS, while with XPS the best results are achieved.

For all three insulation types a significant moisture buildup occured after one year of simulating. Also there's a risk of mould growth at the surface of the wooden beam end, since the relative humidity exceeds the 80% threshold. At the interiour surface, however, applying EPS and XPS results in a lower relative humidity than in the uninsulated situation.

To achieve the best results in reducing the risk at deterioration and still apply insulation at the interior, changes need to be made in the construction. Adding an active heating pipe at the corner between the wall and the floor is such an adaption. The simulated heating pipe is able to localy increase the air temperature to 30°C. The earlier found increase of the moisture level - after one year - for a fully insulated wall with EPS, is halved when the heating pipe has been applied.
The most effective way to reduce the moisture level is to create an insulation gap of 200mm around the wooden beam. After one year only a quarter of the original increase for a fully insulated wall with EPS remains.
There is a downside to applying an insulation gap or an active heating pipe. The heat losses increase compared to a fully insulated wall. For the heating pipe solution this results in a higher energy use. For the insulation gap solution, however, this results in a lower temperature at the interior surface and therefore a higher relative humidity. The relative humidity rises above 75% but remains below the 80% treshold that is used in this research.
Due to the assumptions made for the simulations, the solutions are only applicable for this situation.

10 References

- Abuku, M., Janssen, H. & Roels, S. (2009). *Impact of wind-driven rain on historic brick wall buildings in a moderately cold and humid climate: Numerical analyses of mould growth risk, indoor climate and energy consumption*. Energy and Buildings, Vol. 41. pp. 101–110.
- Adan, O.C.G., & Samson, R.A. (2011). *Fundamentals of mold growth in indoor environments and strategies for healthy living.* Wageningen Academic Publishers. Wageningen, The Netherlands. DOI: 10.3920/978-90-8686-722-6.
- Aelenei, D., & Henriques, F.M.A. (2008). *Analysis of the condensation risk on exterior surface of building envelopes.* Energy and Buildings. Vol. 40. pp.1866–1871.
- Beleudy, C., Woloszyn, M., Chhay, M. & Cosnier, M. (2015). *A 2D model for coupled heat, air, and moisture transfer through porous media in contact with air channels.* International Journal of Heat and Mass Transfer. Vol. 95. pp. 453–465.
- Berger, J., Chhay, M., Guernouti, S. & Woloszyn, M. (2014). *Proper generalized decomposition for solving coupled heat and moisture transfer*. Journal of Building Performance Simulation, DOI: 10.1080/19401493.2014.932012.
- Berger, J., Guernouti, S., Woloszyn, M. & Chinesta, F. (2015). *Proper Generalised Decomposition for heat and moisture multizone modelling*. Energy and Buildings, Vol. 105. pp. 334–351.
- Blocken, B. & Carmeliet, J. (2004). *A review of wind-driven rain research in building science.* Journal of Wind Engineering and Industrial Aerodynamics, Vol. 92. pp. 1079–1130. DOI:10.1016/j.jweia.2004.06.003.
- Blocken, B. & Carmeliet, J. (2005). *High-resolution wind-driven rain measurements on a lowrise building – experimental data for model development and model validation*. Journal of Wind Engineering and Industrial Aerodynamics. Vol. 93 pp. 905-928.
- Blocken, B. & Carmeliet, J. (2006). *The influence of the wind-blocking effect by a building on its wind-driven rain exposure.* Journal of Wind Engineering and Industrial Aerodynamics, Vol. 94. pp. 101–127. DOI:10.1016/j.jweia.2005.11.001.
- Blocken, B. & Carmeliet, J. (2007). *On the errors associated with the use of hourly data in wind-driven rain calculations on building facades.* Atmospheric Environment, Vol. 41. pp. 2335–2343.
- Blocken, B. & Carmeliet, J. (2010). *Overview of three state-of-the-art wind-driven rain assessment models and comparison based on model theory.* Building and Environment, Vol. 45. pp. 691–703.
- Blocken, B., Derome, D. & Carmeliet, J. (2013). *Rainwater runoff from building facades: A review*. Building and Environment Vol. 60. pp. 339-361.
- Bonnema, T.J. (1960). Bouwkunde voor het Hoger Technisch Onderwijs deel 1; Houten Balklagen. Uitgeverij Waltman, Delft. 8e druk.
- Börjesson, F. (2013). *An investigation of the water vapour resistance.* Chalmers University of Technology. Gothenburg, Sweden.
- Borsch-Laaks, R. (2006). *Innendämmung – Wo ist das Risiko?.* WTA-Journal 1/06. pp. 19-42.
- Borsch-Laaks, R. (2009). *Balkendurchdringungen in historischen Außenwänden.* Hochschule Biberbach: Zukunft holz; Statusbericht zum aktuellen Stand der Verwendung von Holz und Holzprodukten im Bauwesen und Evaluierung künftiger Entwicklungspotenziale. pp. 883-887.
- Borsch-Laaks, R. (2010). *Zur Schadensanfälligkeit von Innendämmungen.* Aachener Bausachverständigentage. pp. 35-49.
- Brande, T., Blocken, B. & Roels, S. (2013). *Rain water runoff from porous building facades: Implementation and application of a first-order runoff model coupled to a HAM model*. Building and Environment, Vol. 64. pp. 177-186.
- Bratasz, L., Kozłowska, A. & Kozłowski, R. (2011). A*nalysis of water adsorption by wood using the Guggenheim-Anderson-de Boer equation.* Eur. J. Wood Prod. Vol. 70. pp. 445–451.
- Carmeliet, J., Wit, M.H.D. & Janssen, H. (2005). *Hysteresis and moisture buffering of wood.* In: Proceedings of the 7th Symposium on Building Physics in the Nordic Countries. Reykjavik, Iceland, June 13–15, 2005. pp. 55–62.
- Černý, R., Maděra, J., Kočí, J. & Vejmelková, E. (2009). *Heat and moisture transport in porous materials involving cyclic wetting and drying*. WIT Transactions on Modelling and Simulation, Vol. 48. pp. 3-12. DOI:10.2495/CMEM090011.
- Cestari, C.B. & Lucchio, A. (2001). *Interventions on historical building timber floors: Retractable – visible? Invasive – not visible?* Historical Constructions, pp. 837-846.
- Colinart, T., Lelievre, D., & Glouanecc, P. (2016). *Experimental and numerical analysis of the transient hygrothermalbehavior of multilayered hemp concrete wall*. Energy and Buildings. Vol. 112. pp. 1–11.
- Dafraeye, T. (2011). *Convective heat and mass transfer at exterior building surfaces.* Katholieke Universiteit Leuven - Faculteit Ingenieurswetenschappen. DOI: D/2011/7515/17.
- Delgado, J.M.P.Q., Barreira, E., Ramos, N.M.M & Freitas, V.P. (2013). *Hygrothermal numerical simulation tools applied to building physics*. DOI 10.1007/978-3-642-35003-0.
- Delgado, J.M.P.Q., Guimaraes, A.S. & Freitas, V.P. (2015). *Hygrothermal risk on building heritage; A methodology for a risk map.* DOI 10.1007/978-3-319-19114-0.
- Engelund, E.T. (2011). *Wood – water interactions; Linking molecular level mechanisms with macroscopic performance*. DTU Civil Engineering Report R-258 (UK).
- Engelund, E.T., Thygesen, L.G., Svennson, S., & Hill, C.A.S. (2013). *A critical discussion of the physics of wood–water interactions.* Wood Sci Technol. Vol. 47. pp. 141–161. DOI:10.1007/s00226-012-0514-7.
- Fluent, Inc. (2006). *Fluent 6.3 User's guide.*
- Ge, H. & Krpan, R. (2009). *Wind-driven Rain Study in the Coastal Climate of British Columbia.* Building Science Centre of Excellence, BCIT.
- Gnoth, S., Jurk, K., & Strangfeld, P. (2005). *Hygrothermisches Verhalten eingebetteter Holzbalkenköpfe im innnengedämmten Außenmauerwerk*. Bauphysik 27, Vol. 2. pp. 117-128.
- Goethem, S. (2014). Rainwater runoff on building facades: Numerical simulations and prediction of wetting patterns. Faculty of Engineering and Architecture. Ghent University.
- Goesten, S. (2016). *Hygrothermal simulation model: Damage as a result of insulating historical buildings.* Master thesis.

- Grobbauer, M., & Ruisinger, U. (2012). *Innendämmung, Holzbalkenköpfe und Kastenfenster in der Sanierung*. Technische Universität Graz, Bauphysiktagung 2012. pp. 88-108. DOI: 10.3217/978-3-85125-237-8.
- Guizzardi, M., Derome, D., Vonbank, R. & Carmeliet, J. (2015a). *Hygrothermal behavior of a massive wall with interior insulation during wetting.* Building and Environment, Vol. 89. pp. 59-71.
- Guizzardi, M., Carmeliet, J. & Derome, D. (2015b). *Risk analysis of biodeterioration of wooden beams embedded in internally insulated masonry walls*. Construction and Building Materials, Vol. 99. pp. 159–168.
- Hagentoft, C.E., et al. (2001). *Introduction to building physics.* Sweden, Lund: Studentlitteratur Ab.
- Hagentoft, C.E. (2002). *HAMSTAD – Final report: Methodology of HAM-Modeling*. Gothenburg, Department of Building Physics, Chalmers University of Technology.
- Hagentoft, C.E., et al. (2004). *Assessment method of numerical prediction models for combined Heat, Air and Moisture transfer in building components: Benchmarks for one-dimensional cases*. Journal of thermal environment & building science, Vol. 27, pp. 327-352. DOI: 10.1177/1097196304042436.
- Hagentoft, C.E. & Kalagasidis, A.S. (2012). *Hygrothermal conditions and mould growth potential in cold attics: Impact of weather, building system and construction design characteristics.* DOI: 10.1007/978-3-642-31158-1_4.
- Harrestrup, M. & Svendsen, S. (2015). *Full-scale test of an old heritage multi-storey building undergoing energy retrofitting with focus on internal insulation and moisture*. Building and Environment, Vol. 85. pp.123-133.
- Harrestrup, M. & Svendsen, S. (2016). *Internal insulation applied in heritage multi-storey buildings with wooden beams embedded in solid masonry brick façades.* Building and Environment, Vol. 99. pp. 59-72.
- Hens, H.L.S.C. (2015). *Combined heat, air, moisture modelling: A look back, how, of help?* Building and Environment, Vol. 91. pp. 138-151.
- Holle, H.J. (2009). I*nnendämmung bei erhaltenswerten Fassaden - ein baukonstruktives Projektbeispiel*. Bauphysik 31, Vol. 4. pp. 227-234. DOI: 10.1002/bapi.200910030.
- Janetti, M.B., Ochs, F., & Feist, W. (2011). *3D Simulation of Heat and Moisture Diffusion in Constructions*. University of Innsbruck, Unit Building Physics, Innsbruck, Austria.
- Janetti, M.B., Ochs, F. & Wolfgang, F. (2012). *On the conservation of mass and energy in hygrothermal numerical simulation with COMSOL multiphysics*. Proceedings of BS2013: 13th Conference of International Building Performance Simulation Association, Chambéry, France, August 26-28. pp. 2860-2867.
- Janetti, M.B. (2016). *Hygrothermal analysis of building components inclosing air cavities: Comparison between different modeling approaches and experimental results*. Leopold-Franzens-Universität. Innsbruck, Austria.
- Janssen, H. (2014). *Simulation efficiency and accuracy of different moisture transfer potentials*. Journal of Building Performance Simulation. Vol. 7, No. 5. pp. 379-389. DOI: 10.1080/19401493.2013.852246.
- Kehl, D. (2012). *Holzbalkenköpfe im Mauerwerk*. Holzbau 6. pp. 20-25.
- Kehl, D., Ruisinger, U., Plagge, R., & Grunewald, J. (2013). *Wooden beam ends in masonry with interior insulation – A literature review and simulation on causes and assessment of decay.* Proceedings of 2nd Central European Symposium on Building Physics.
- KNMI. (2000). *Handbook for the meteorological observation.* Koninklijk Nederlands Meteorologisch Instituut.
- Lelievre, D., Colinart, T., & Glouannec, P. (2014). *Hygrothermal behavior of bio-based building materials including hysteresis effects: Experimental and numerical analyses.* Energy and Buildings. Vol. 84. pp. 617–627.
- Li, Q., Rao, J., & Fazio, P. (2009). *Development of HAM tool for building envelope analysis.* Building and Environment. Vol. 44. pp. 1065–1073.
- Morelli, M., Nielsen, T.R., Scheffler, G.A., & Svendsen, S. (2010). *Internal insulation of masonry walls with wooden floor beams in northern humid climate.* Proceedings at Thermal Performance of the Exterior Envelopes of Whole Buildings XI. pp. 89.
- Morelli, M., & Svendsen, S. (2012). *Investigation of interior post-insulated masonry walls with wooden beam ends*. Journal of building physics 36, Vol. 3. pp. 265-292. DOI: 10.1177/1744259112447928.
- NEN-EN 13013-3 (1997). *Hydrothermal performance of buildings - Climatic data - Part 3: Calculating a driving rain index for vertical surfaces from hourly wind and rain data.* NNI: NEN-EN 13013-3:1997.
- NEN-EN-ISO 15927-3 (2009). *Hygrothermal performance of buildings - Calculation and presentation of climatic data - Part 3: Calculation of a driving rain index for vertical surfaces from hourly wind and rain data.* NNI: NEN-EN-ISO 15927-3:2009.
- Nespoli, L. (2013a). Analysis of heat and moisture transfer in building components by conjugate modeling.
- Nusser, B. & Teibinger, M. (2012). *Coupled heat and moisture transfer in building components.* Excerpt from the proceedings of the 2012 COMSOL Conference in Milan.
- Ochs, F., Heidemann, W. & Müller-Steinhagen, H. (2008). *Effective thermal conductivity of moistened insulation materials as a function of temperature*. International Journal of Heat and Mass Transfer. Vol. 51. pp. 539–552.
- Portal, N.W., Aarle van, M.A.P., & Schijndel van, A.W.M. (2011). *Simulation and Verification of Coupled Heat and Moisture Modeling*.
- Portal, N.W., Schijndel, A.W.M., & Kalagasidis, A.S. (2013). *The multiphysics modeling of heat and moisture induced stress and strain of historic building materials and artefacts.* BUILD SIMUL. Vol. 7. pp. 217–227. DOI: 10.1007/s12273-013-0153-4.
- Rafidiarison, H., Rémond, R., & Mougel, E. (2015). *Dataset for validating 1-D heat and mass transfer models within building walls with hygroscopic materials.* Building and Environment. Vol. 89. pp. 356-368.
- RCE. (2016). Data downloaded at 26-12-2016 from: http://rce.webgispublisher.nl/Viewer.aspx?map=Monumentenkaart_groot#.
- Renato, P. (2013). *Innovative approaches for the experimental determination of the liquid water conductivity and validation of a model for heat and moisture transfer in porous building materials.*
- Rhydock, J.P. (2005). Validation of a present weather observation method for driving rain mapping. Norwegian University of Science and Technology.
- Santos, G.H., Mendes, N. & Philippi, P.C. (2009). *A building corner model for hygrothermal performance and mould growth risk analyses*. International Journal of Heat and Mass Transfer. Vol. 52. pp. 4862–4872.

- Schie, F.T. (2013). *A combination of state space and mapping functions in matlab: Evaluation tool for climate related cases in the Netherlands*. Eindhoven University of Technology.
- Schijndel, A.W.M., Goesten, S. & Schellen, H. (2016). *HAMSTAD Benchmarks using Comsol revisited.* Eindhoven University of Technology.
- Smith, D. (2012). *Climate Change and its Potential Impacts on Construction in Ireland: The Argument for Mitigation and Adaptation.* National University of Ireland, Maynooth.
- Steen, J.M., & Schijndel, A.W.M. (2015). *The development of a mapping tool for the evaluation of building systems for future climate scenarios on European scale*. Eindhoven University of Technology.
- Stopp, H., Strangfeld, P., Toepel, T., & Anlauft, E. (2010). *Messergebnisse und bauphysikalische Lösungsansätze zur Problematik der Holzbalkenköpfe in Außenwänden mit Innendämmung*. Bauphysik 32, Vol. 2. pp. 61-72. DOI: 10.1002/bapi.201010008.
- Strangfeld, P., et al. (2011). *Bauphysikalisch schadensfreie Innendämmung von Außenwänden mit eingebundenen Holzbalkenköpfen*. Wissenschaftstage der Hochschule Lausitz.
- Tammes, E., & Vos, B.H. (1986). *Warmte- en vochttransport in bouwconstructies.* Deventer: Kluwer.
- Tariku, F., Kumaran, K., & Fazio, P. (2010). *Transient model for coupled heat, air and moisture transfer through multilayered porous media.* International Journal of Heat and Mass Transfer. Vol. 53. pp. 3035–3044.
- Uittenbosch, S. (2012). *Risico van inwendige condensatie in een externe scheidingsconstructie.* Eindhoven University of Technology.
- Vereecken, E., & Roels, S. (2015). *Capillary active interior insulation: do the advantages really offset potential disadvantages?* Materials and Structures. Vol. 48. pp. 3009–3021. DOI: 10.1617/s11527-014-0373-9.
- Viitanen, H., Vinha, J., Salminen, K., Ojanen, T., Peuhkuri, R., Paajanen, L., & Lähdesmäki, K. (2010a). *Moisture and bio-deterioration risk of building materials and structures.* Journal of Building Physics. Vol. 33. pp. 201-224. DOI: 10.1177/1744259109343511.
- Viitanen, H., Toratti, T., Makkonen, L., Peuhkuri, R., Ojanen, T., Ruokolainen, L., Räisänen, J. (2010b). *Towards modelling of decay risk of wooden materials*. Eur. J. Wood Prod. Vol. 68. pp. 303–313. DOI: 10.1007/s00107-010-0450-x.
- Vinha, J. (2007). *Hygrothermal performance of timber-framed external walls in finnish climatic conditions.* Tampere University of Technology.
- Vololonirina, O., Coutand, M., & Perrin, B. (2014). *Characterization of hygrothermal properties of wood-based products – Impact of moisture content and temperature.* Construction and Building Materials. Vol. 63. pp. 223–233.
- Wit, M.H. (2009). *Heat, Air and Moisture in building envelopes.* Eindhoven University of Technology.
- Woloszyn, M., & Rode, C. (2008). Tools for performance simulation of Heat, Air and Moisture conditions of whole buildings. Build Simul. Vol.1. pp. 5–24. DOI: 10.1007/s12273-008-8106-z.
- Zhang, X., Zillig, W., Künzel, H.M., Mitterer, C., Zhang, X. (2016). *Combined effects of sorption hysteresis and its temperature dependency on wood materials and building enclosures-part II: Hygrothermal modeling.* Building and Environment. Vol. 106. pp. 181-195.

11 Appendix

- Appendix I Factors wind driven rain
Table 11.1 Roughness coefficient from EN-ISO 15927-3:2009.
Table 11.2 Obstruction factor from EN-ISO 15927-3:2009.
Figure 11.1 Wall factors from EN-ISO 15927-3:2009.

- Appendix II Mathematical equations Lpc as moisture potential

- Appendix III Comparison Comsol with Delphin wall 2
Figure 11.2-11.7 Comparison T and RH simple model
Figure 11.8-11.13 Comparison T and RH simple model with Schirmer
Figure 11.14-11.19 Comparison T and RH simple model with adapted boundary conditions
Figure 11.20-11.28 Comparison T, RH and P_a sophisticated model with adapted boundary conditions.

- Appendix IV Comparison Comsol with Delphin wall 4
Figure 11.29-11.38 Comparison T and RH simple model
Figure 11.39-11.48 Comparison T and RH simple model with Schirmer
Figure 11.49-11.58 Comparison T and RH simple model with adapted boundary conditions
Figure 11.59-11.73 Comparison T, RH and P_a sophisticated model with adapted boundary conditions.

- Appendix V Material data
Figure 11.74-11.79 Comparison sorption isotherm for OSB, plaster and wood fibre board.
Figure 11.80-11.85 Comparison capillary suction and moisture permeability for OSB, plaster and wood fibre board.
Figure 11.86-11.91 Comparison vapour diffusion for OSB, plaster and wood fibre board.

- Appendix VI Comparison Comsol with measurements wall 2 and wall 4
Figure 11.92-11.97 Wall 2 comparison T and RH with material data of Rafidiarison et al. [2015].
Figure 11.98-11.107 Wall 4 comparison T and RH with material data of Rafidiarison et al. [2015].

- Appendix VII Simulated variants
Figure 11.108 Variants devided over three categories that are simulated.

- Appendix VIII Climate used in Case Study
Figure 11.109-11.110 External temperature, relative humidity and wind-driven rain applied.
Figure 11.111-11.112 Air pressure difference applied for dwelling and museum indoor climate.

- Appendix IX Results Case Study summer
Figure 11.113-11.116 Surface plots T and RH of an uninsulated wall with different indoor climates.
Figure 11.117-11.120 Surface plots T and RH of an insulated wall with different indoor climates.
Figure 11.121-11.124 Surface plots T and RH of an insulated wall with different constructions.

Appendix I

Table 11.1 Roughness coëfficient (C_r) from EN-ISO 15927-3:2009 [Blocken, et al. 2010]

Terrain category	Description	K_r	z_0	z_{min}
I	Rough open sea; lake shore with at least 5 km open water upwind and smooth flat country without obstacles	0.17	0.01	2
II	Farm land with boundary hedges, occasional small farm structures, houses or trees	0.19	0.05	4
III	Suburban or industrial areas and permanent forests	0.22	0.3	8
IV	Urban areas in which at least 15% of the surface is covered with buildings of average height exceeding 15 m	0.24	1	16

Table 11.2 Obstruction factor (O) from EN-ISO 15927-3:2009 [Blocken, et al. 2010]

Distance of obstruction from facade (m)	Obstruction factor O
0-2*	0.1*
2-4*	0.2*
4-8	0.2
8-15	0.3
15-25	0.4
25-40	0.5
40-60	0.6
60-80	0.7
80-100	0.8
100-120	0.9
over 120	1.0

* These numbers complete the standard [Coutu, S. 2013]

Description of wall	Average value	Distribution
Two-storey gable	0,4	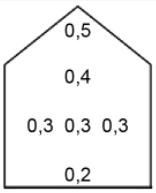
Three-storey gable	0,3	
Multi-storey building with flat roof (pitch < 20°)	0,2 for a ten-storey building, for example, but with a higher intensity at top	0,5 for top 2,5m
Two-storey wall with eaves	0,3	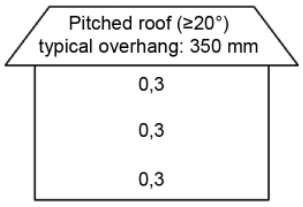
Three-storey wall with eaves	0,4	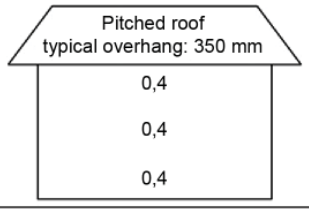
Two-storey building with flat roof (pitch < 20°)	0,4	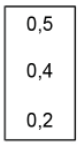

Figure 11.1 Wall factors (W) from EN-ISO 15927-3:2009 [Blocken, et al. 2010]

Appendix II

Heat

The heat equation includes the conductive heat flux, latent heat and the heat flux by convection:

$$(\rho \cdot c + c_l \cdot w)\frac{\partial T}{\partial t} + c_l \cdot T \cdot \frac{\partial w}{\partial t} = \nabla(\lambda \cdot \nabla T) + L_v \cdot \nabla(\delta_p \nabla p_v) - L_v \cdot r_a \cdot \rho_v - r_a \cdot \rho_a \cdot c_{pa} \cdot \nabla T$$

The parts which include the latent heat in the equation require the right potential:

$$L_v(\nabla \delta_p - r_a \cdot \nabla \rho_v) \cdot \frac{\partial p_v}{\partial x}$$

$$\rightarrow \quad p_v = p_{sat} \cdot \exp\left(\frac{-p_c}{\rho_w \cdot R_v \cdot T}\right)$$

$$\rightarrow \quad \varphi = \exp\left(\frac{-p_c}{\rho_w \cdot R_v \cdot T}\right)$$

$$L_v(\nabla \delta_p - r_a \cdot \rho_v) \cdot \frac{\partial(\varphi \cdot p_{sat}(T))}{\partial x}$$

$$L_v(\nabla \delta_p - r_a \cdot \rho_v)\left(\varphi \cdot \frac{p_{sat}(T)}{\partial x} + p_{sat}(T) \cdot \frac{\partial \varphi}{\partial x}\right)$$

$$L_v(\nabla \delta_p - r_a \cdot \rho_v)\left(\varphi \cdot \frac{p_{sat}}{\partial T} \cdot \frac{\partial T}{\partial x} + p_{sat}(T) \cdot \frac{\partial \varphi}{\partial x}\right)$$

$$\rightarrow \quad p_c = \rho_l \cdot R_v \cdot T \cdot \ln(\varphi)$$

$$L_v(\nabla \delta_p - r_a \cdot \rho_v)\left(\varphi \cdot \frac{p_{sat}}{\partial T} \cdot \frac{\partial T}{\partial x} + p_{sat}(T) \cdot \frac{\partial \varphi}{\partial p_c} \cdot \frac{\partial p_c}{\partial x}\right)$$

$$\rightarrow \quad \frac{\partial \varphi}{\partial p_c} = \frac{1}{\rho_w \cdot R_v \cdot T} \cdot \exp\left(\frac{-p_c}{\rho_w \cdot R_v \cdot T}\right)$$

$$\rightarrow \quad \frac{\partial \varphi}{\partial p_c} = \frac{1}{\rho_w \cdot R_v \cdot T} \cdot \exp\left(\frac{-\rho_w \cdot R_v \cdot T \cdot \ln(\varphi)}{\rho_w \cdot R_v \cdot T}\right)$$

$$\rightarrow \quad \frac{\partial \varphi}{\partial p_c} = \frac{-\varphi}{\rho_w \cdot R_v \cdot T}$$

$$\rightarrow \quad \frac{\partial \varphi}{\partial p_c} = \frac{\varphi}{\rho_w \cdot R_v \cdot T}$$

$$L_v(\nabla \delta_p - r_a \cdot \nabla \rho_v)\left(\varphi \cdot \frac{p_{sat}}{\partial T} \cdot \frac{\partial T}{\partial x} - p_{sat}(T) \cdot \frac{\varphi}{\rho_w \cdot R_v \cdot T} \cdot \frac{\partial p_c}{\partial x}\right)$$

$$\rightarrow \quad Lp_c = \log_{10}(p_c)$$

$$\rightarrow \quad p_c = 10^{Lp_c}$$

$$\rightarrow \quad \frac{\partial p_c}{\partial Lp_c} = 10^{Lp_c} \cdot \log_{10}(10)$$

$$\rightarrow \quad \frac{\partial p_c}{\partial Lp_c} = 10^{Lp_c} \cdot 2.3026$$

$$L_v(\nabla \delta_p - r_a \cdot \nabla \rho_v)\varphi \cdot \frac{p_{sat}}{\partial T}\frac{\partial T}{\partial x} - L_v(\nabla \delta_p - r_a \cdot \nabla \rho_v) \cdot p_{sat}(T)\frac{\varphi}{\rho_w R_v T} \cdot \frac{\partial p_c}{\partial Lp_c} \cdot \frac{\partial Lp_c}{\partial x}$$

The previous equations are implemented in the heat flux equation:

$$(\rho c + c_l w)\frac{\partial T}{\partial t} = \lambda \cdot \nabla T + L_v \cdot \nabla \delta_p \cdot \varphi \frac{\partial p_{sat}}{\partial T} \cdot \nabla T - L_v \cdot \nabla \delta_p \cdot p_{sat}(T) \cdot \frac{\varphi}{\rho_w R_v T} \cdot \frac{\partial p_c}{\partial Lp_c} \cdot \nabla Lp_c - L_v \cdot r_a \cdot \rho_v \cdot$$

$$\varphi \cdot \frac{\partial p_{sat}}{\partial T} \cdot \nabla T + L_v \cdot r_a \cdot \rho_v \cdot p_{sat}(T) \cdot \frac{\varphi}{\rho_w R_v T} \cdot \frac{\partial p_c}{\partial Lp_c} \cdot \nabla Lp_c - r_a \cdot \rho_a \cdot c_{pa} \cdot \nabla T$$

The equation is made more compact by using brackets:

$$(\rho c + c_l w)\frac{\partial T}{\partial t} = \left(\nabla \lambda + L_v \cdot (\nabla \delta_p - r_a \cdot \nabla \rho_v) \varphi \cdot \frac{\partial p_{sat}}{\partial T} - r_a \cdot \rho_a \cdot c_{pa} \right) \cdot \nabla T + L_v (\nabla \delta_p - r_a \cdot \rho_v) \cdot$$

$$p_{sat}(T) \cdot \frac{\varphi}{\rho_w R_v T} \cdot \frac{\partial p_c}{\partial Lp_c} \cdot \nabla Lp_c$$

Moisture transport

The same mathematical transformation is done for the potential of the moisture flux:

$$\frac{\partial w}{\partial t} = \nabla(\delta_p \cdot \nabla p_v) - r_a \cdot \rho_v + \nabla((-k_m) \cdot (\nabla p_c + \rho_l \cdot g \cdot z))$$

The storage term at the left side of the equation is changed to the equivalent with the potential Lpc:

$$\frac{\partial w}{\partial p_c} \cdot \frac{\partial p_c}{\partial Lp_c} \cdot \frac{\partial Lp_c}{\partial t} = \nabla(\delta_p \cdot \nabla p_v) - r_a \cdot \rho_v + \nabla((-k_m) \cdot (\nabla p_c + \rho_l \cdot g \cdot z))$$

The water vapor transport by diffusion and convection in the equation receives the Lpc as potential:

$$(\delta_p \cdot \nabla p_v) - r_a \cdot \rho_v$$

$$(\delta_p - r_a \cdot \rho_v) \nabla p_v$$

$$(\nabla \delta_p - r_a \cdot \rho_v) \varphi \cdot \frac{p_{sat}}{\partial T} \cdot \frac{\partial T}{\partial x} - (\nabla \delta_p - r_a \cdot \rho_v) p_{sat}(T) \frac{\varphi}{\rho_w R_v T} \cdot \frac{\partial p_c}{\partial Lp_c} \cdot \frac{\partial Lp_c}{\partial x}$$

When the equation is inserted into the water vapor transport equation, this leads to:

$$\frac{\partial w}{\partial p_c} \cdot \frac{\partial p_c}{\partial Lp_c} \cdot \frac{\partial Lp_c}{\partial t} = (\nabla \delta_p - r_a \cdot \rho_v) \varphi \cdot \frac{\partial p_{sat}}{\partial T} \nabla T -$$

$$(\nabla \delta_p - r_a \cdot \rho_v) p_{sat}(T) \cdot \frac{\varphi}{\rho_w R_v T} \cdot \frac{\partial p_c}{\partial Lp_c} \nabla Lp_c + \nabla(-k_m) \cdot \frac{\partial p_c}{\partial Lp_c} \nabla Lp_c$$

The equation is made more compact by using brackets:

$$\frac{\partial w}{\partial p_c} \cdot \frac{\partial p_c}{\partial Lp_c} \cdot \frac{\partial Lp_c}{\partial t} = (\nabla \delta_p - r_a \cdot \rho_v) \varphi \cdot \frac{\partial p_{sat}}{\partial T} \nabla T +$$

$$\left(\left((\nabla \delta_p - r_a \cdot \rho_v) p_{sat}(T) \cdot \frac{\varphi}{\rho_w R_v T} \cdot \frac{\partial p_c}{\partial Lp_c} \right) - \nabla k_m \cdot \frac{\partial p_c}{\partial Lp_c} \right) \nabla Lp_c$$

Appendix III

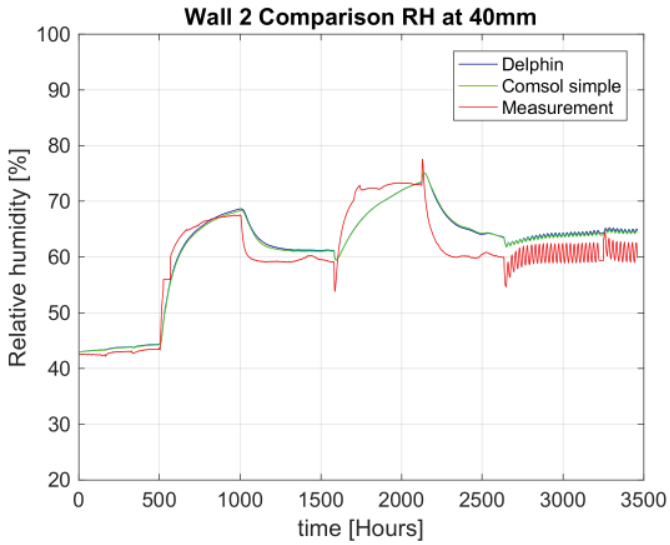

Figure 11.2 RH at 40mm. Comparison between Comsol model with implemented flux based at Goesten [2016] and Delphin.

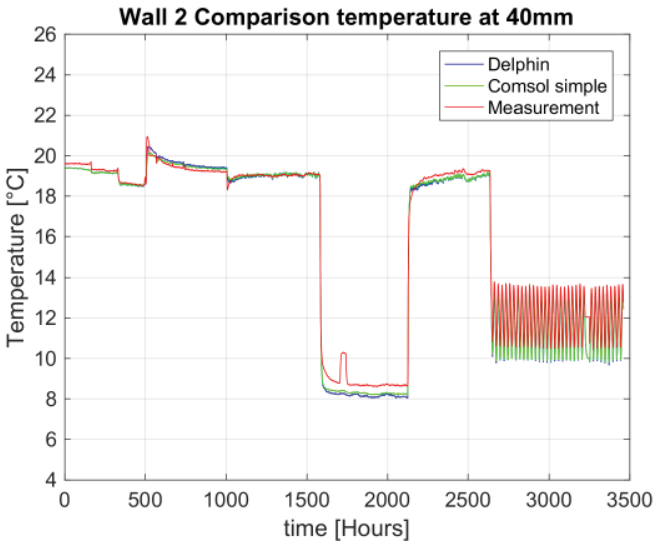

Figure 11.3 T at 40mm. Comparison between Comsol model with implemented flux based at Goesten [2016] and Delphin.

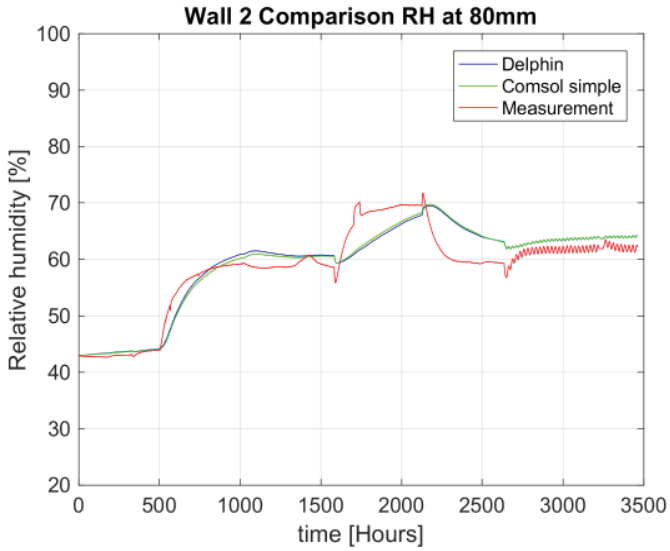

Figure 11.4 RH at 80mm. Comparison between Comsol model with implemented flux based at Goesten [2016] and Delphin.

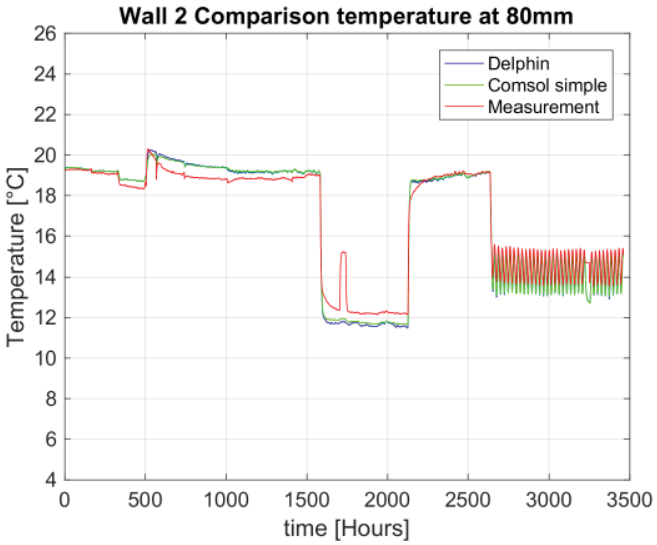

Figure 11.5 T at 80mm. Comparison between Comsol model with implemented flux based at Goesten [2016] and Delphin.

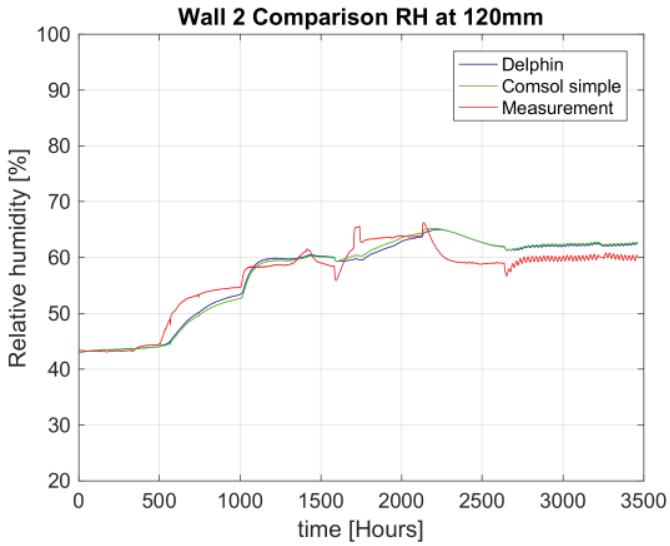

Figure 11.6 RH at 120mm. Comparison between Comsol model with implemented flux based at Goesten [2016] and Delphin.

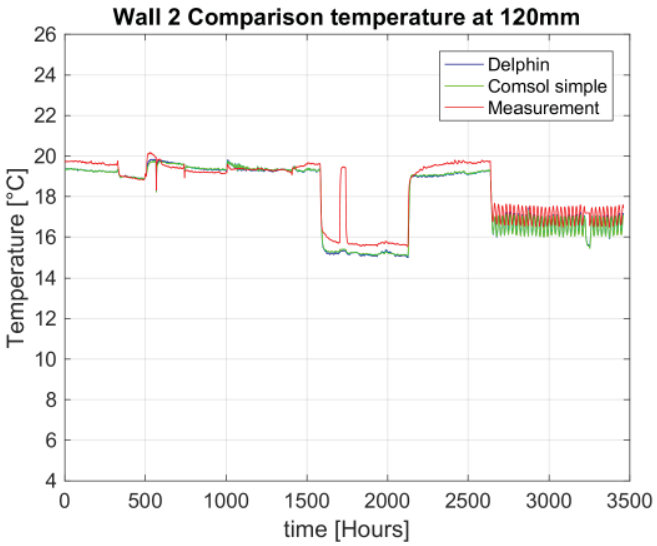

Figure 11.7 T at 120mm. Comparison between Comsol model with implemented flux based at Goesten [2016] and Delphin.

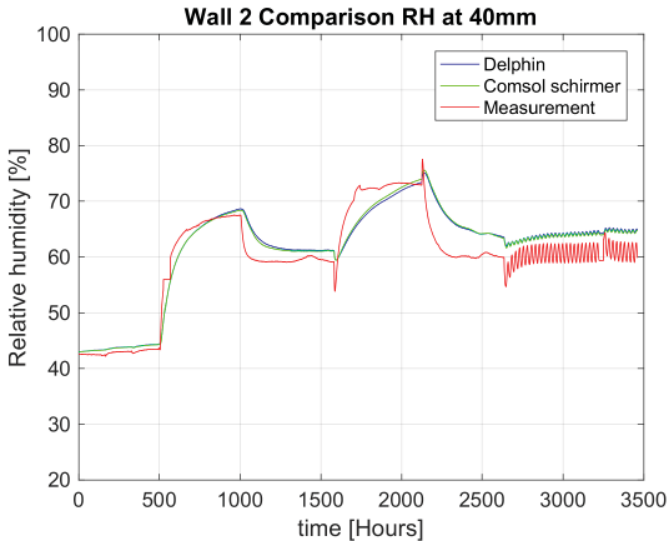

Figure 11.8 RH at 40mm. Comparison between Comsol model with implemented flux, added Schirmer equation and Delphin.

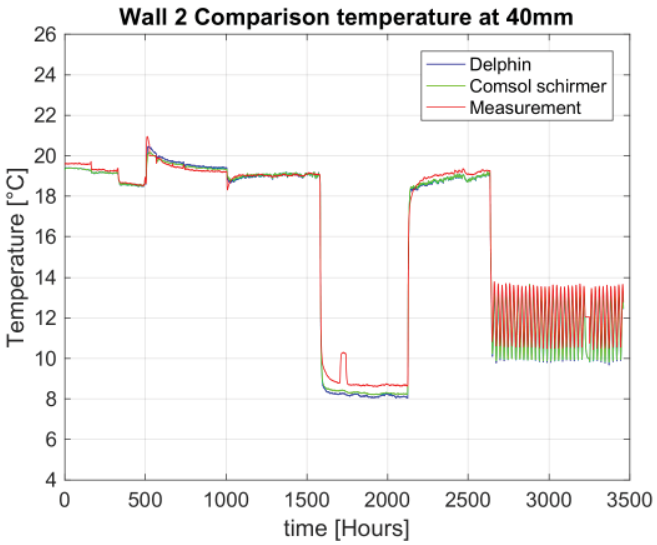

Figure 11.9 T at 40mm. Comparison between Comsol model with implemented flux, added Schirmer equation and Delphin.

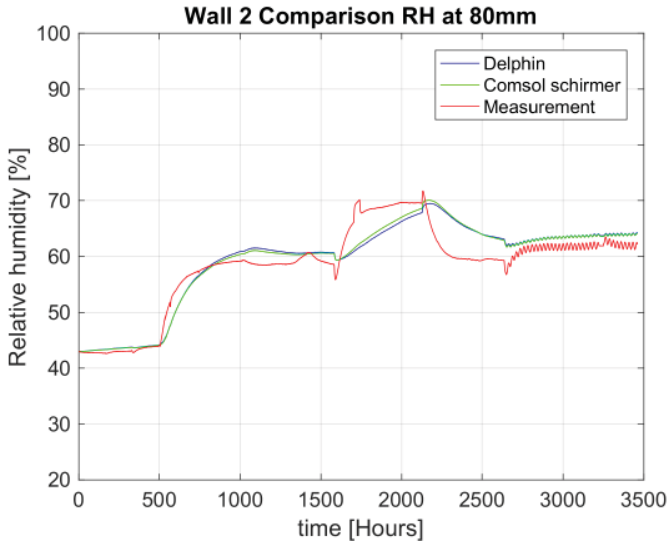

Figure 11.10 RH at 80mm. Comparison between Comsol model with implemented flux, added Schirmer equation and Delphin.

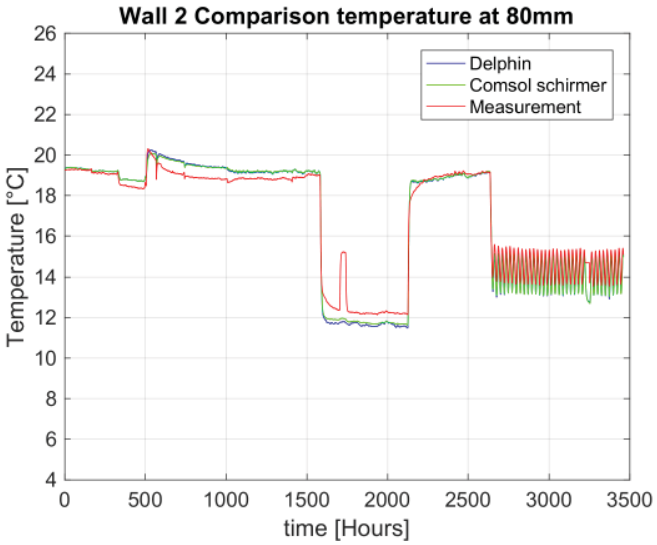

Figure 11.11 T at 80mm. Comparison between Comsol model with implemented flux, added Schirmer equation and Delphin.

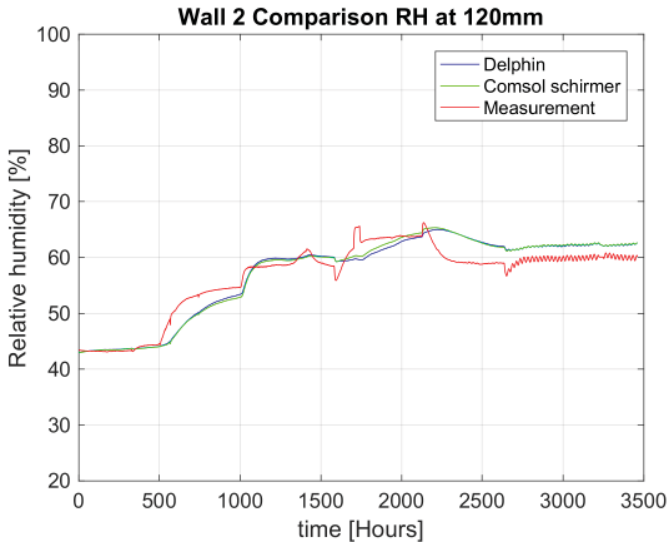

Figure 11.12 RH at 120mm. Comparison between Comsol model with implemented flux, added Schirmer equation and Delphin.

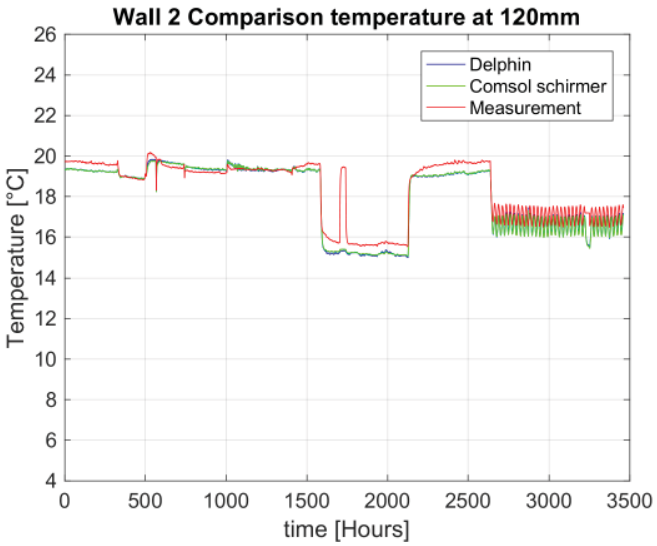

Figure 11.13 T at 120mm. Comparison between Comsol model with implemented flux, added Schirmer equation and Delphin.

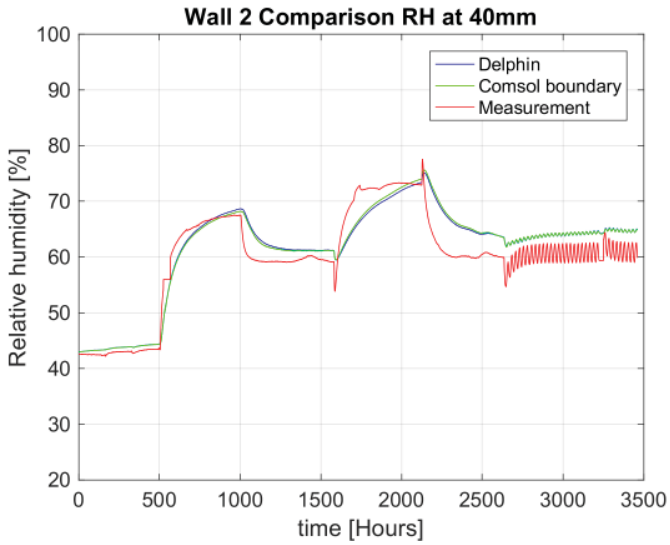

Figure 11.14 RH at 40mm. Comparison between Comsol model with implemented flux, adapted boundary conditions and Delphin.

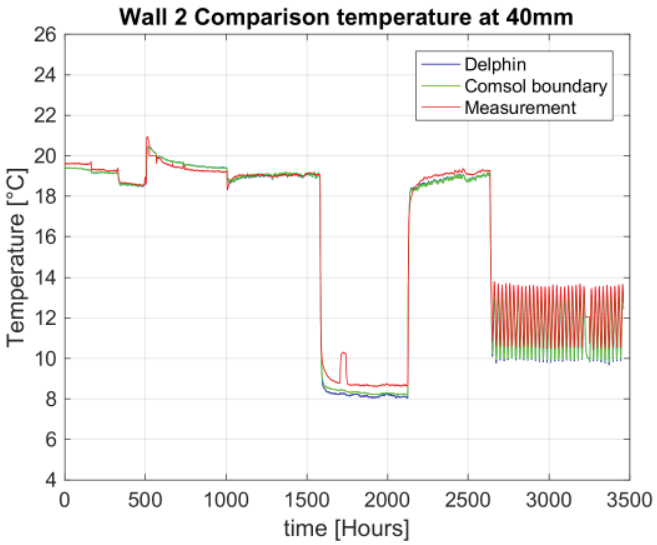

Figure 11.15 T at 40mm. Comparison between Comsol model with implemented flux, adapted boundary conditions and Delphin.

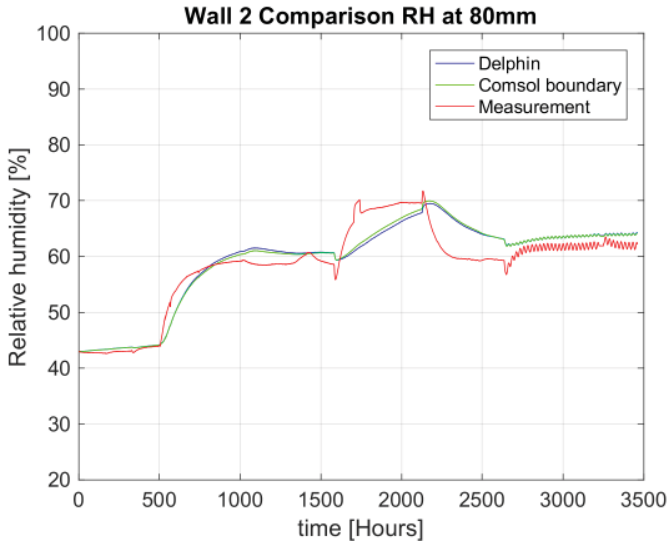

Figure 11.16 RH at 80mm. Comparison between Comsol model with implemented flux, adapted boundary conditions and Delphin.

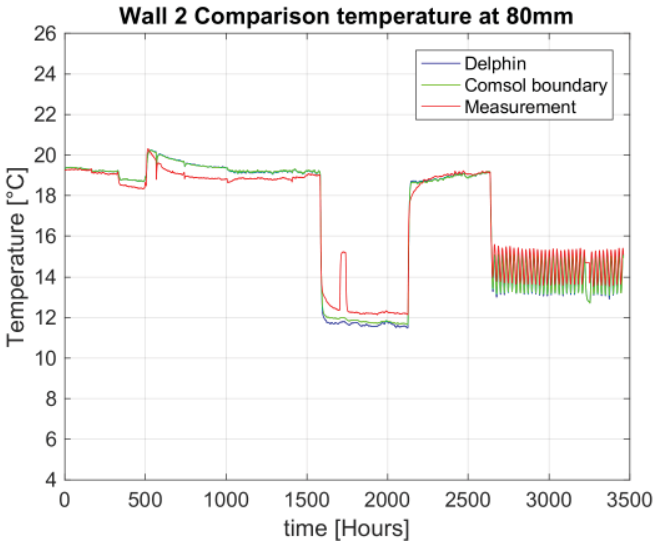

Figure 11.17 T at 80mm. Comparison between Comsol model with implemented flux, adapted boundary conditions and Delphin.

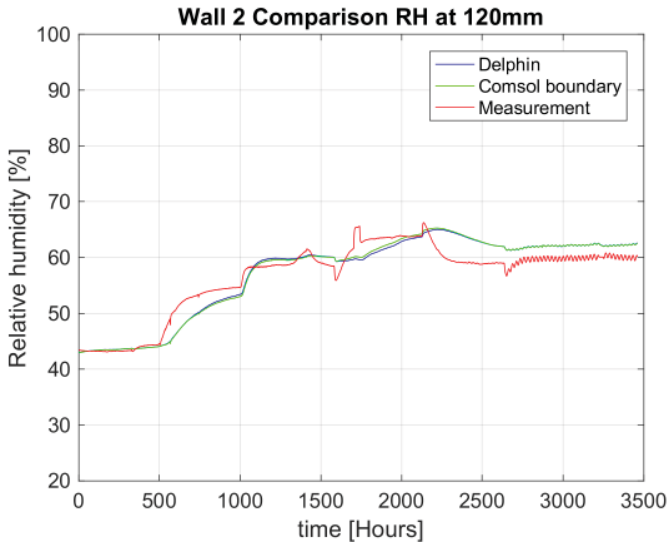

Figure 11.18 RH at 120mm. Comparison between Comsol model with implemented flux, adapted boundary conditions and Delphin.

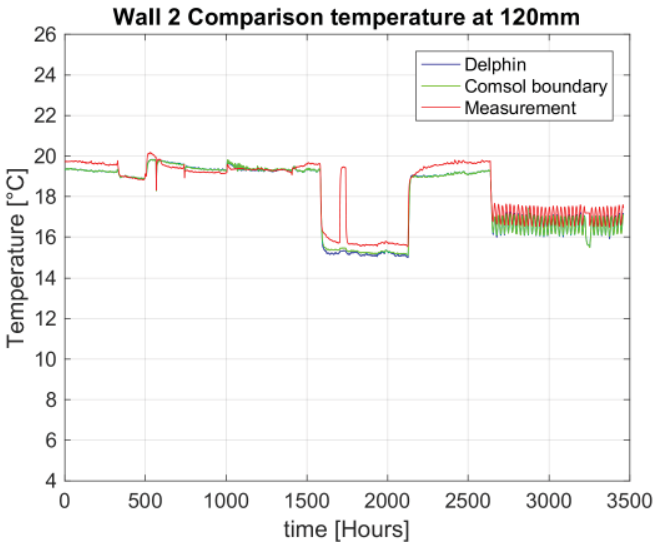

Figure 11.19 T at 120mm. Comparison between Comsol model with implemented flux, adapted boundary conditions and Delphin.

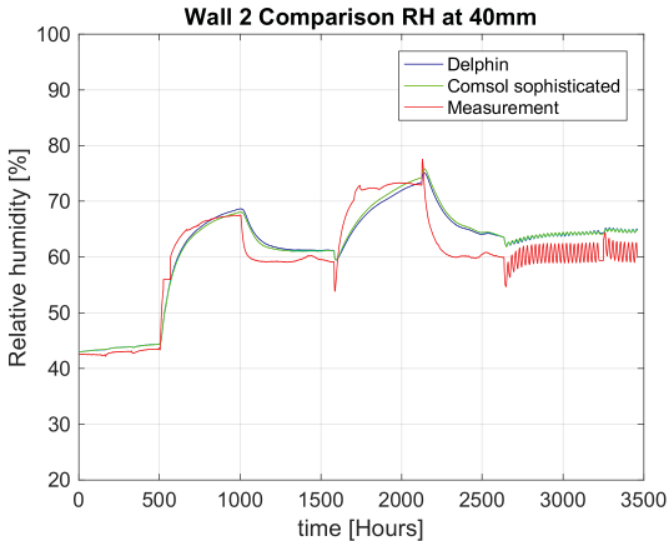

Figure 11.20 RH at 40mm. Comparison Comsol model with seperate flux, adapted boundary conditions and Delphin.

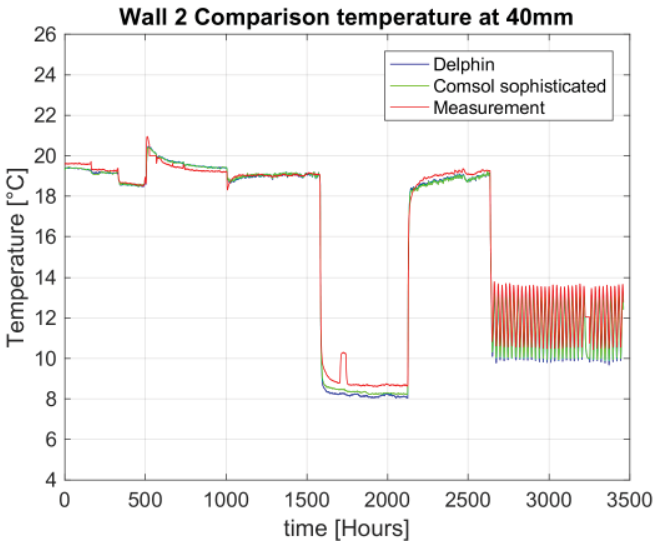

Figure 11.21 T at 40mm. Comparison Comsol model with seperate flux, adapted boundary conditions and Delphin.

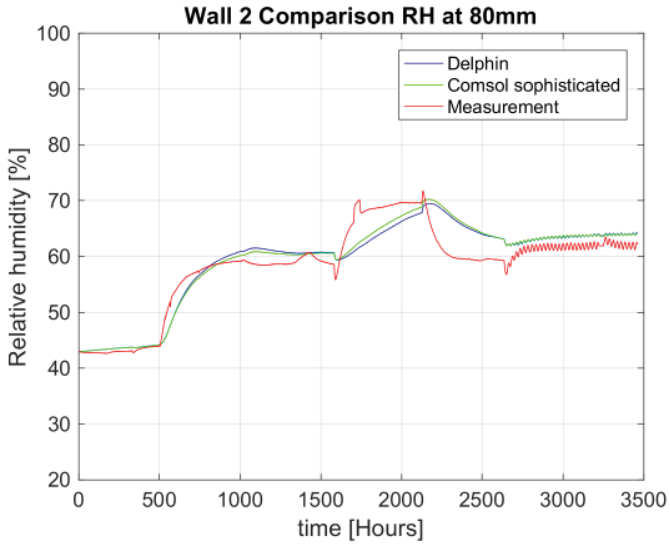

Figure 11.22 RH at 80mm. Comparison Comsol model with seperate flux, adapted boundary conditions and Delphin.

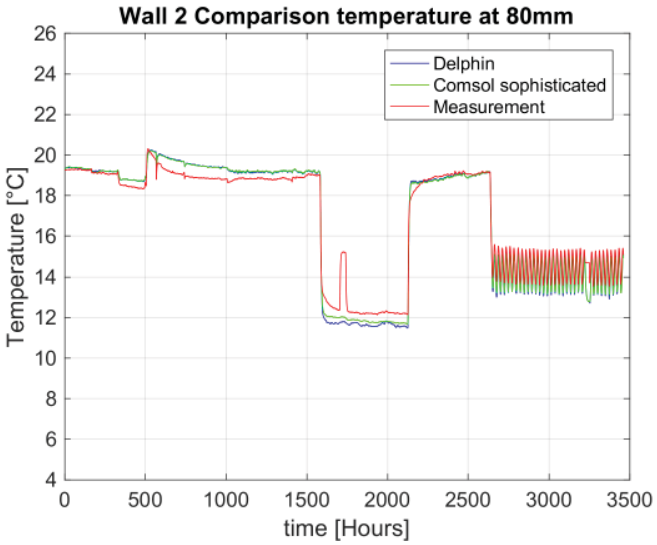

Figure 11.23 T at 80mm. Comparison Comsol model with seperate flux, adapted boundary conditions and Delphin.

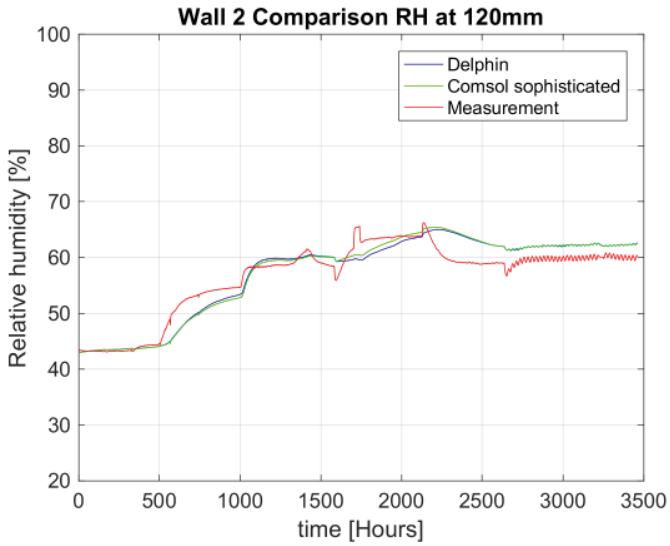

Figure 11.24 RH at 120mm. Comparison Comsol model with seperate flux, adapted boundary conditions and Delphin.

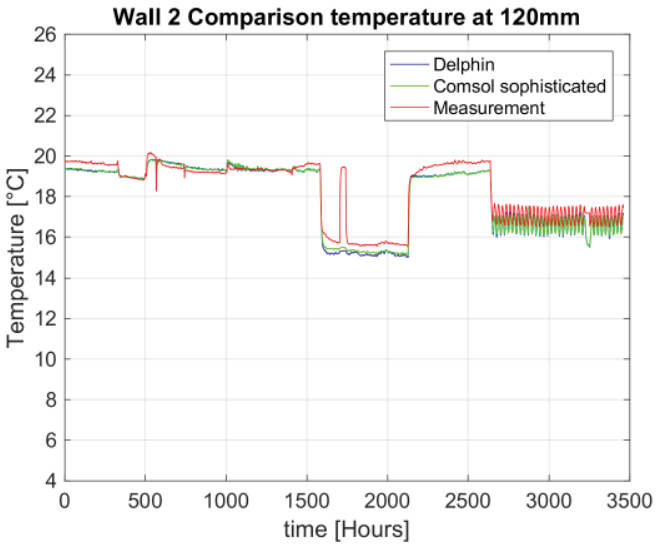

Figure 11.25 T at 120mm. Comparison Comsol model with seperate flux, adapted boundary conditions and Delphin.

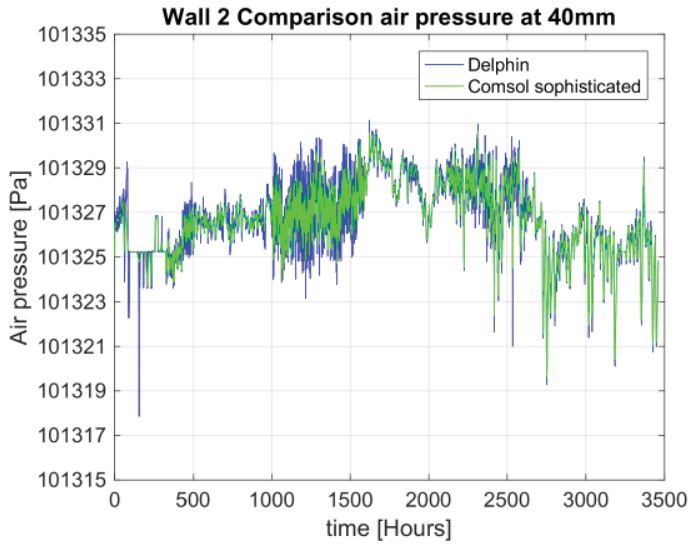

Figure 11.26 p_a at 40mm. Comparison Comsol model with seperate flux, adapted boundary conditions and Delphin.

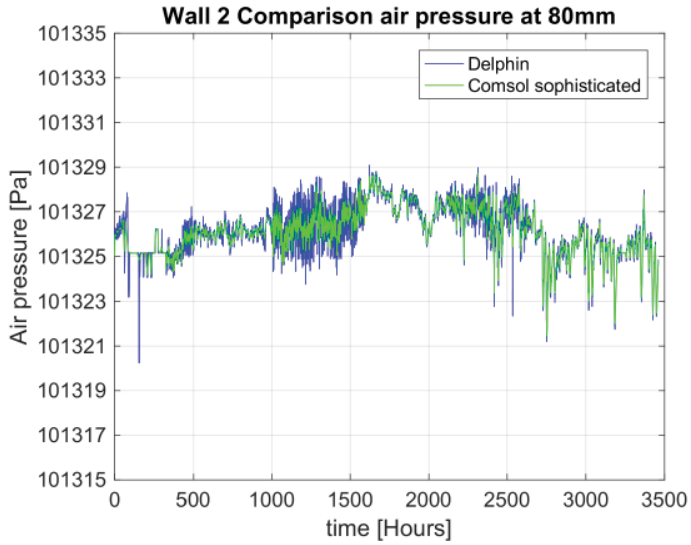

Figure 11.27 p_a at 80mm. Comparison Comsol model with seperate flux, adapted boundary conditions and Delphin.

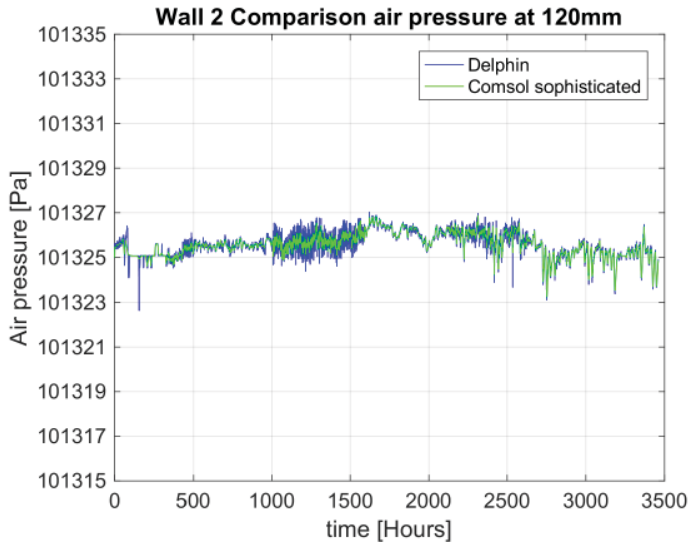

Figure 11.28 p_a at 120mm. Comparison Comsol model with seperate flux, adapted boundary conditions and Delphin.

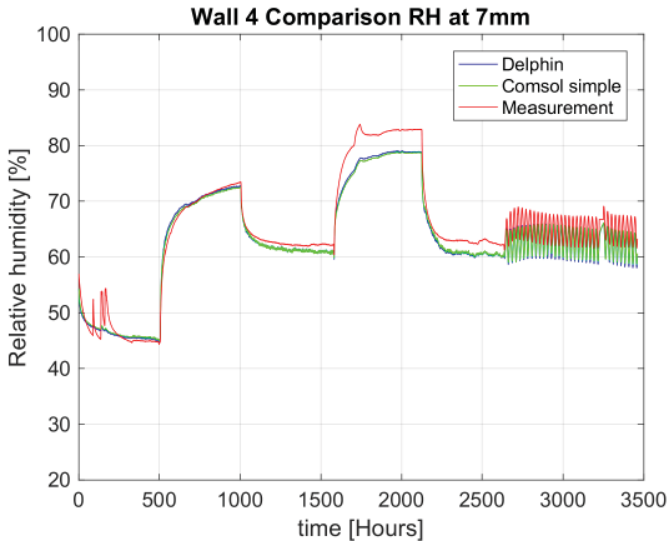

Figure 11.29 RH at 7mm. Comparison between Comsol model with implemented flux based at Goesten [2016] and Delphin.

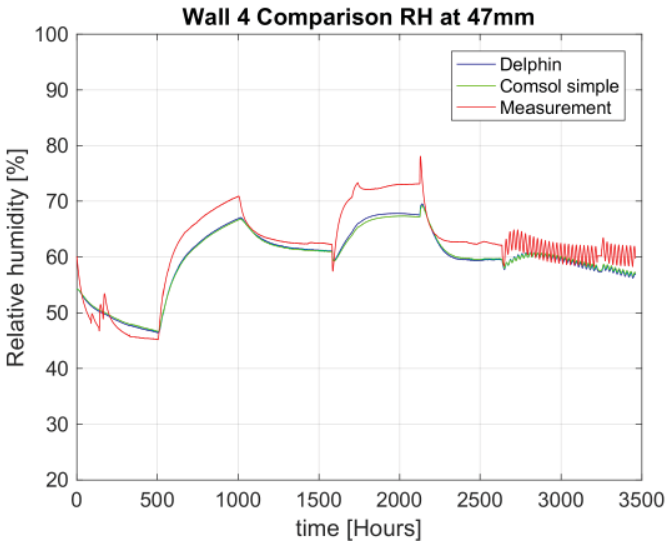

Figure 11.30 RH at 47mm. Comparison between Comsol model with implemented flux based at Goesten [2016] and Delphin.

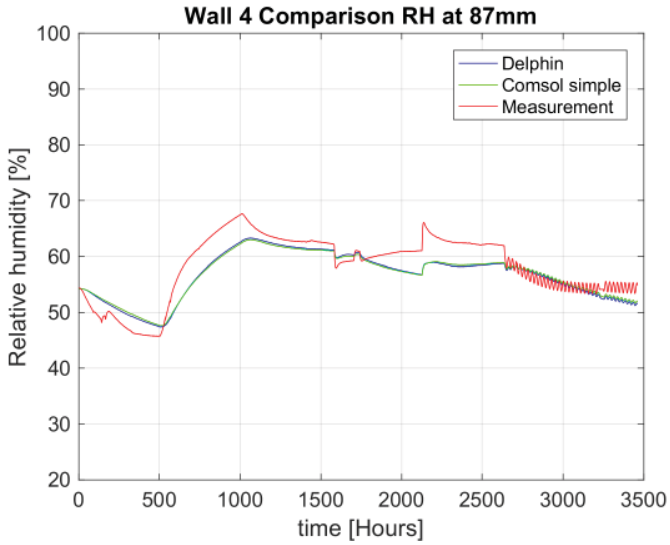

Figure 11.31 RH at 87mm. Comparison between Comsol model with implemented flux based at Goesten [2016] and Delphin.

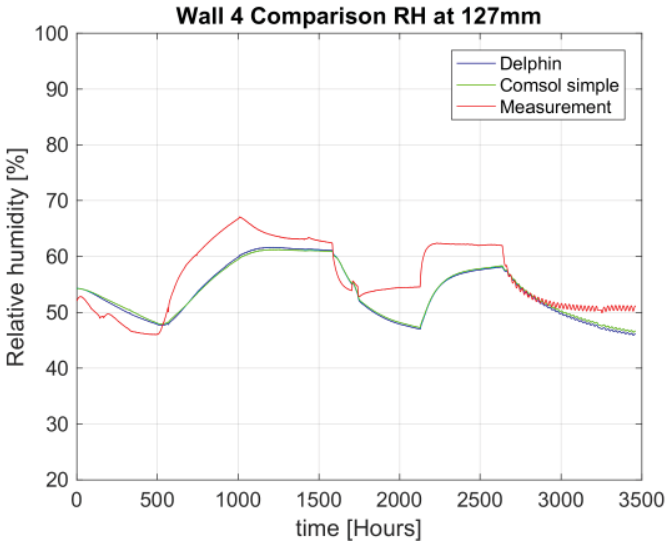

Figure 11.32 RH at 127mm. Comparison between Comsol model with implemented flux based at Goesten [2016] and Delphin.

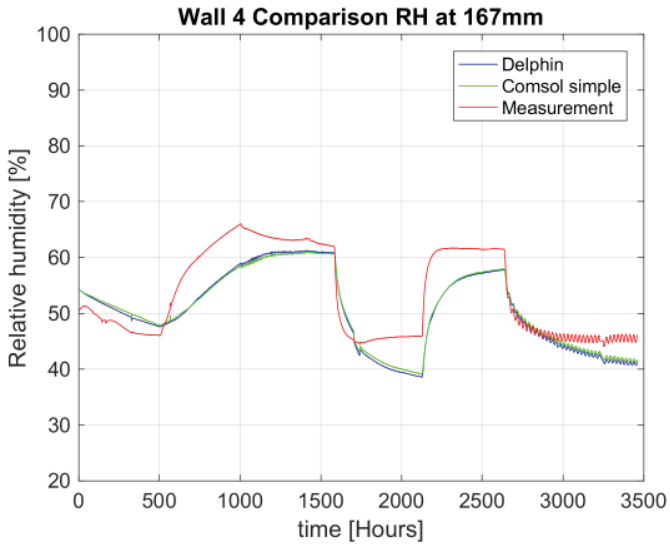

Figure 11.33 RH at 167mm. Comparison between Comsol model with implemented flux based at Goesten [2016] and Delphin.

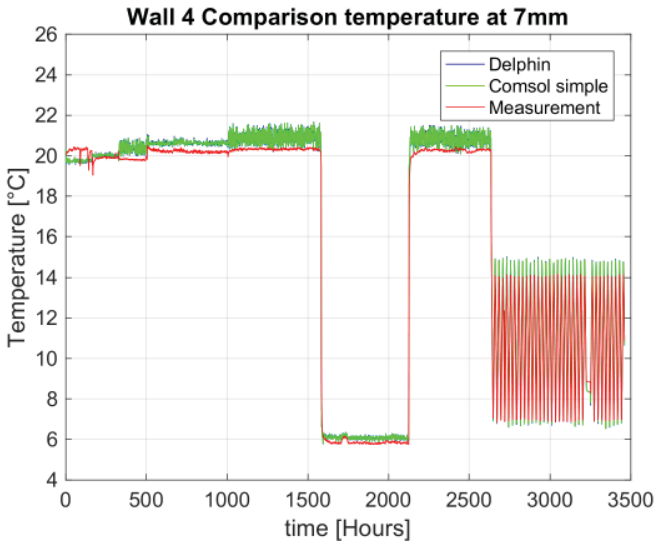

Figure 11.34 T at 7mm. Comparison between Comsol model with implemented flux based at Goesten [2016] and Delphin.

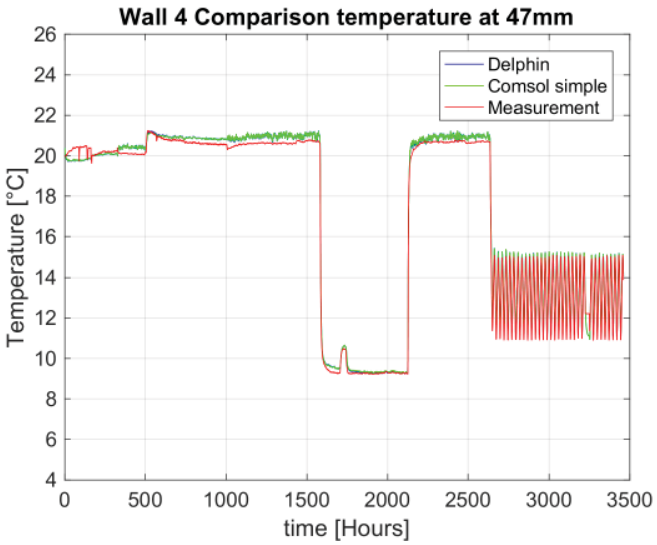

Figure 11.35 T at 47mm. Comparison between Comsol model with implemented flux based at Goesten [2016] and Delphin.

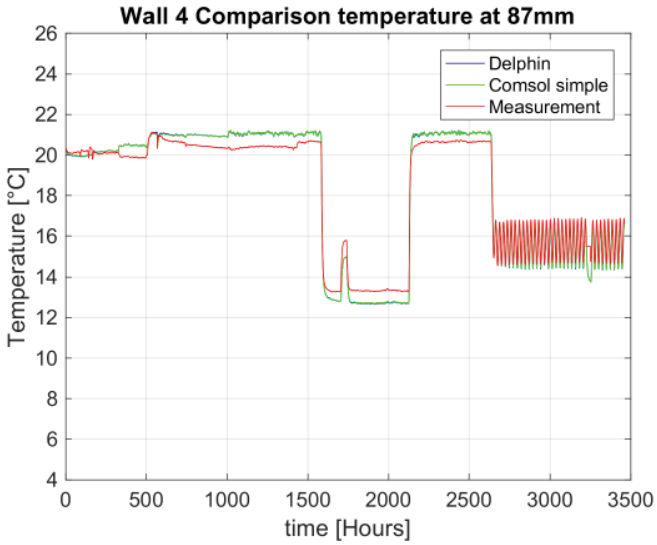

Figure 11.36 T at 87mm. Comparison between Comsol model with implemented flux based at Goesten [2016] and Delphin.

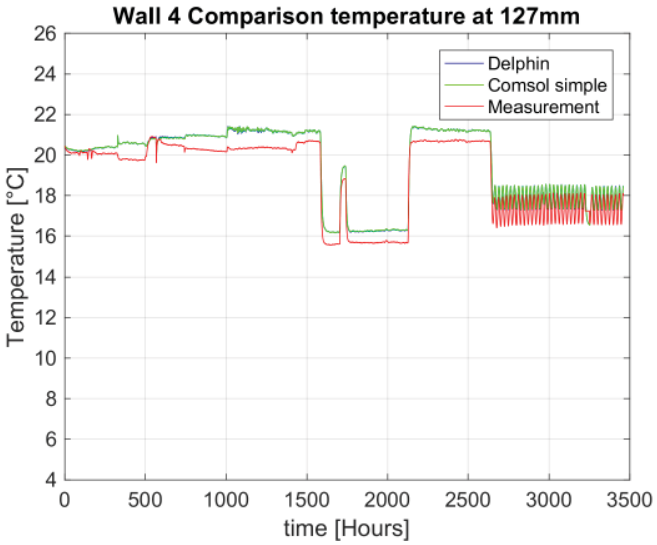

Figure 11.37 T at 127mm. Comparison between Comsol model with implemented flux based at Goesten [2016] and Delphin.

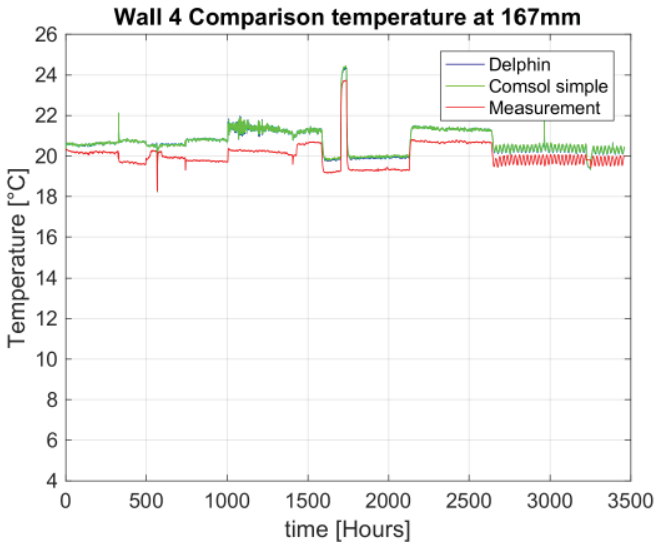

Figure 11.38 T at 167mm. Comparison between Comsol model with implemented flux based at Goesten [2016] and Delphin.

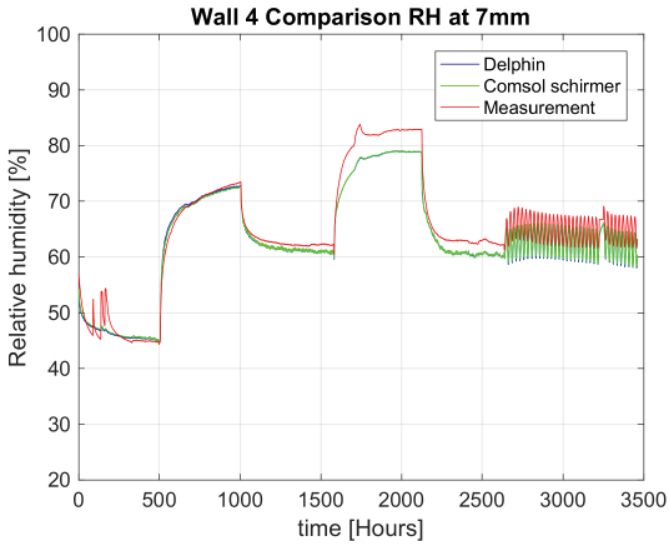

Figure 11.39 RH at 7mm. Comparison between Comsol model with implemented flux, added Schirmer equation and Delphin.

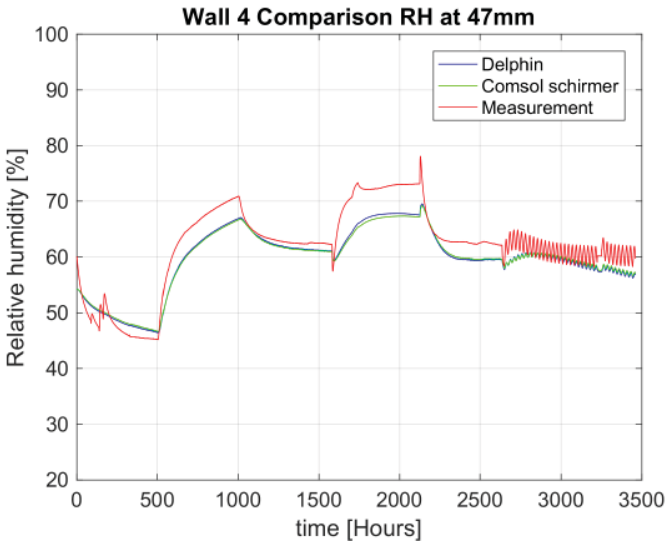

Figure 11.40 RH at 47mm. Comparison between Comsol model with implemented flux, added Schirmer equation and Delphin.

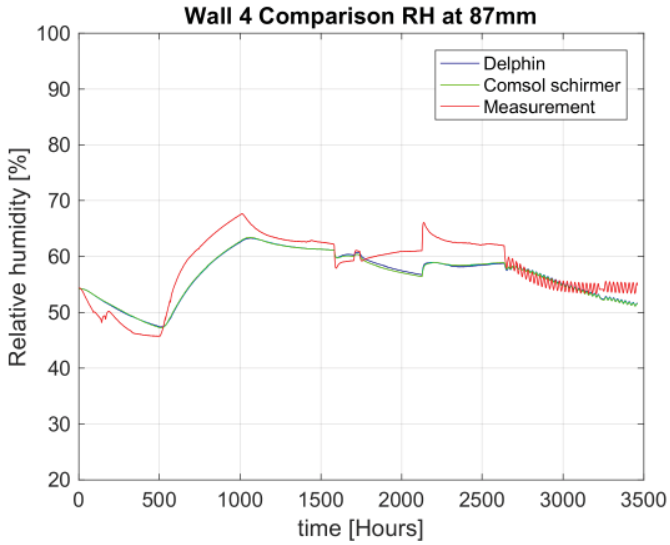

Figure 11.41 RH at 87mm. Comparison between Comsol model with implemented flux, added Schirmer equation and Delphin.

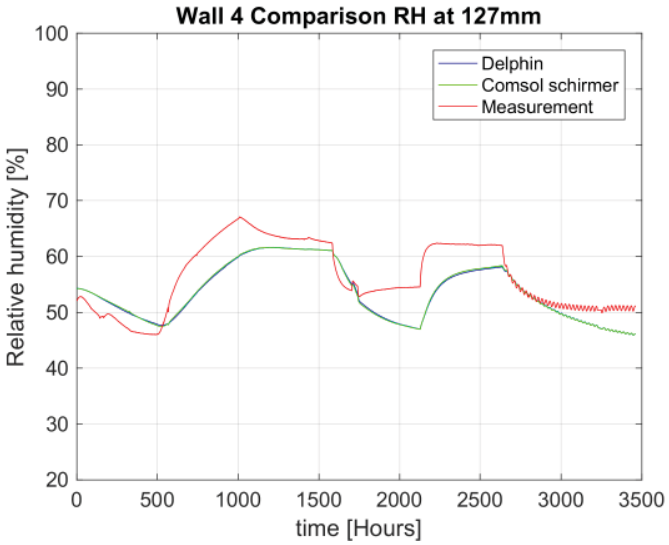

Figure 11.42 RH at 127mm. Comparison between Comsol model with implemented flux, added Schirmer equation and Delphin.

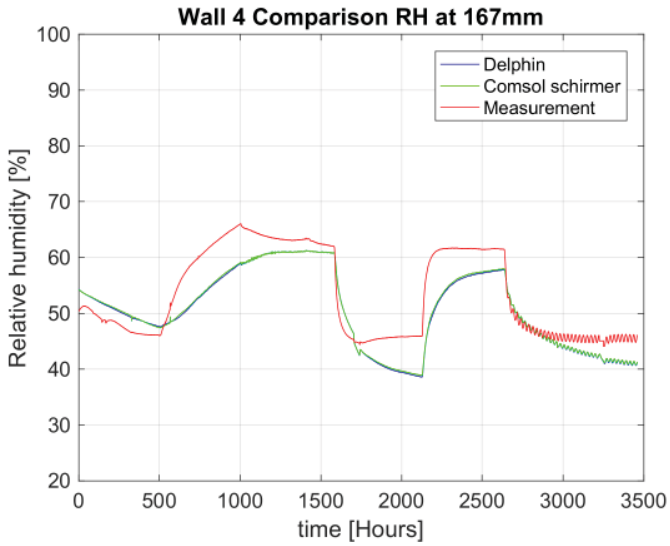

Figure 11.43 RH at 167mm. Comparison between Comsol model with implemented flux, added Schirmer equation and Delphin.

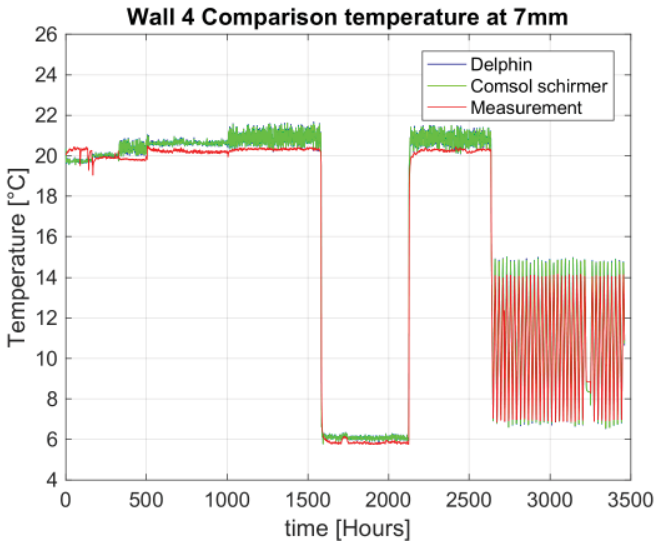

Figure 11.44 T at 7mm. Comparison between Comsol model with implemented flux, added Schirmer equation and Delphin.

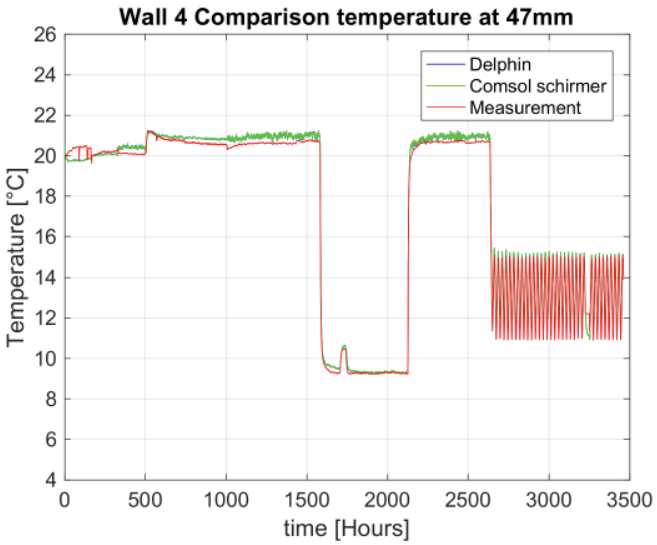

Figure 11.45 T at 47mm. Comparison between Comsol model with implemented flux, added Schirmer equation and Delphin.

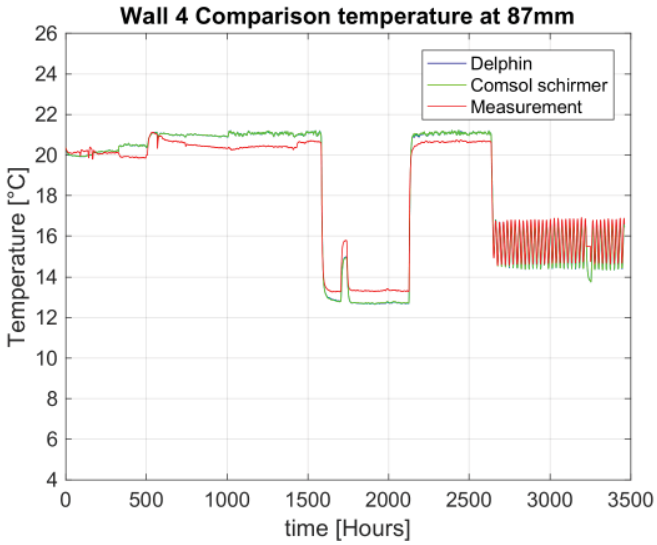

Figure 11.46 T at 87mm. Comparison between Comsol model with implemented flux, added Schirmer equation and Delphin.

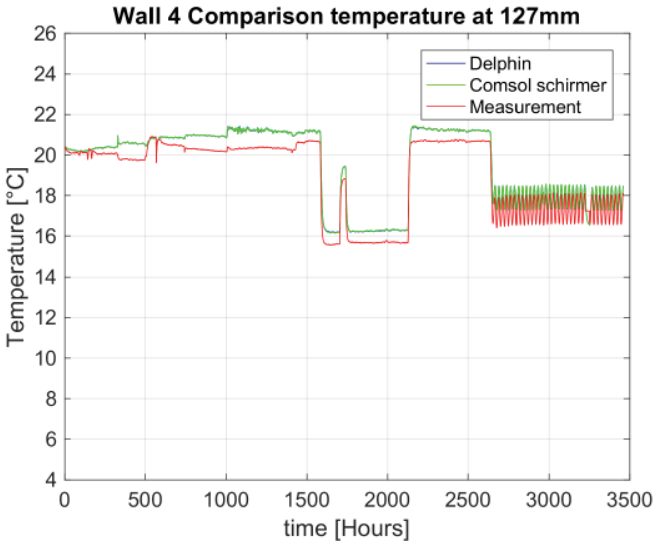

Figure 11.47 T at 127mm. Comparison between Comsol model with implemented flux, added Schirmer equation and Delphin.

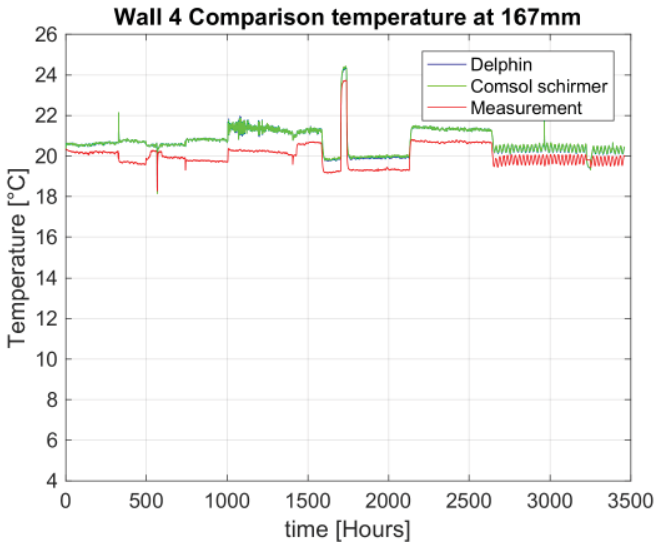

Figure 11.48 T at 167mm. Comparison between Comsol model with implemented flux, added Schirmer equation and Delphin.

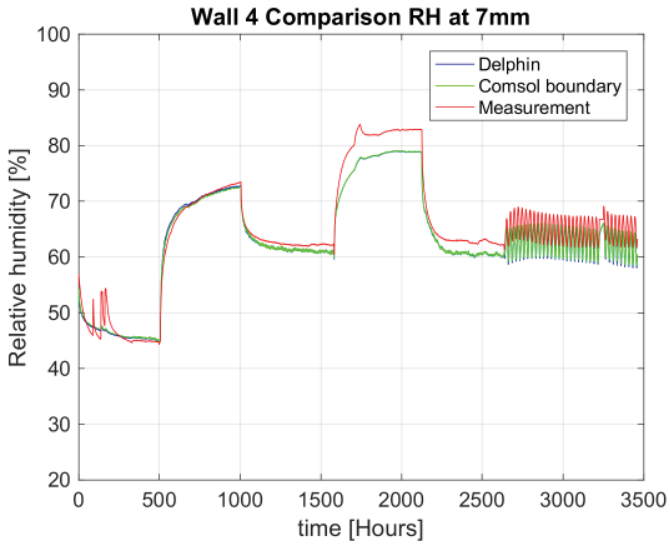

Figure 11.49 RH at 7mm. Comparison between Comsol model with implemented flux, adapted boundary conditions and Delphin.

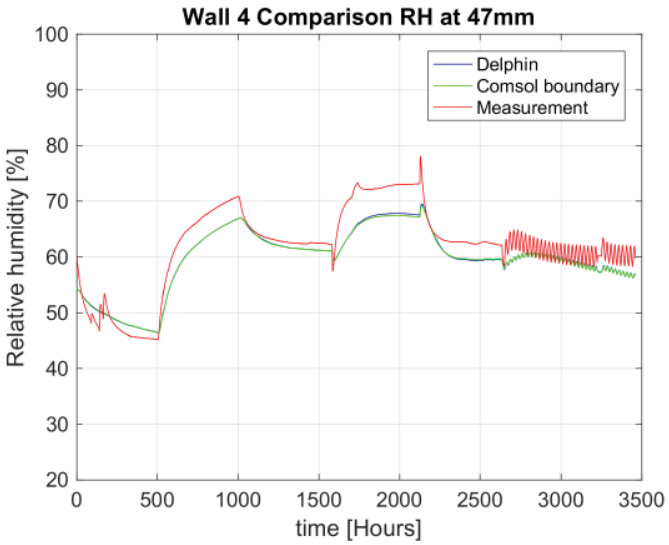

Figure 11.50 RH at 47mm. Comparison between Comsol model with implemented flux, adapted boundary conditions and Delphin.

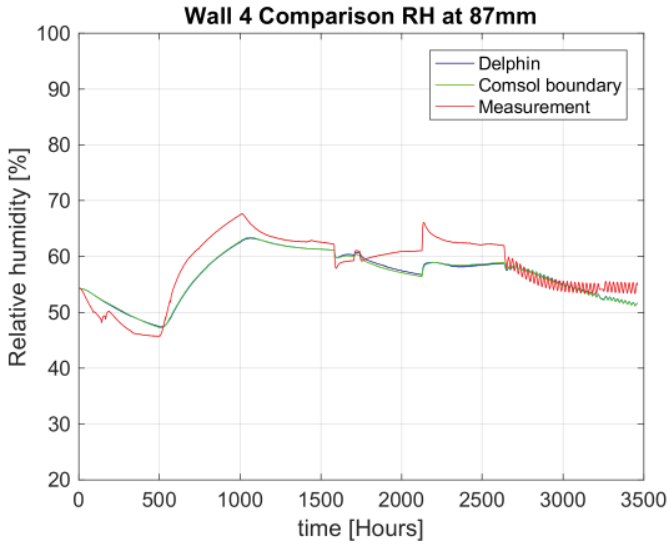

Figure 11.51 RH at 87mm. Comparison between Comsol model with implemented flux, adapted boundary conditions and Delphin.

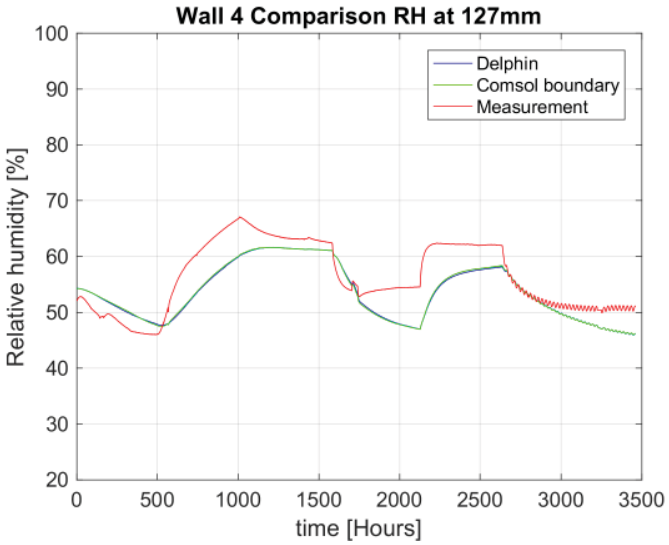

Figure 11.52 RH at 127mm. Comparison between Comsol model with implemented flux, adapted boundary conditions and Delphin.

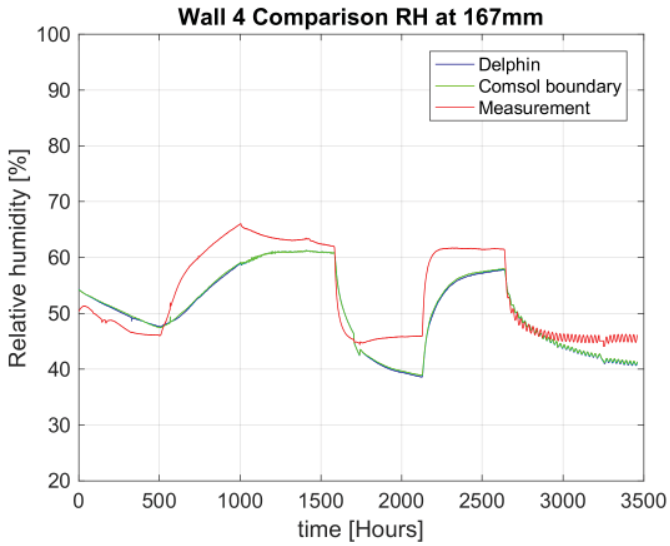

Figure 11.53 RH at 167mm. Comparison between Comsol model with implemented flux, adapted boundary conditions and Delphin.

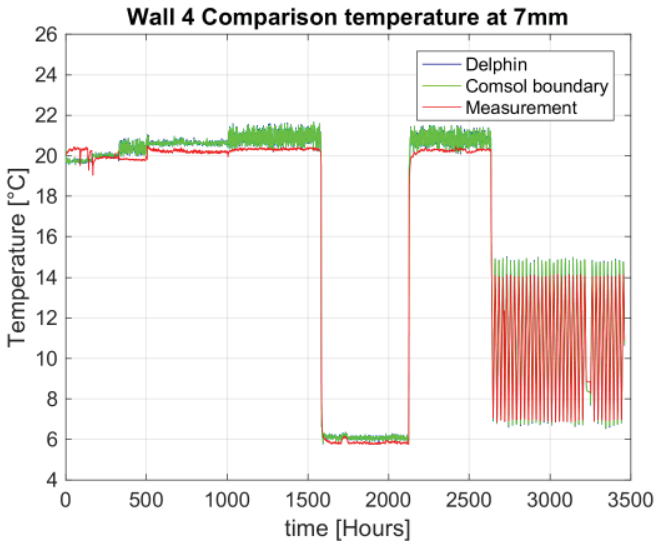

Figure 11.54 T at 7mm. Comparison between Comsol model with implemented flux, adapted boundary conditions and Delphin.

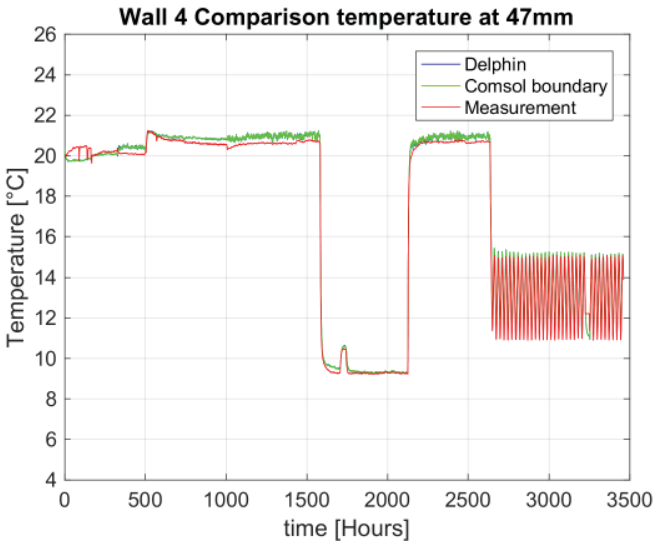

Figure 11.55 T at 47mm. Comparison between Comsol model with implemented flux, adapted boundary conditions and Delphin.

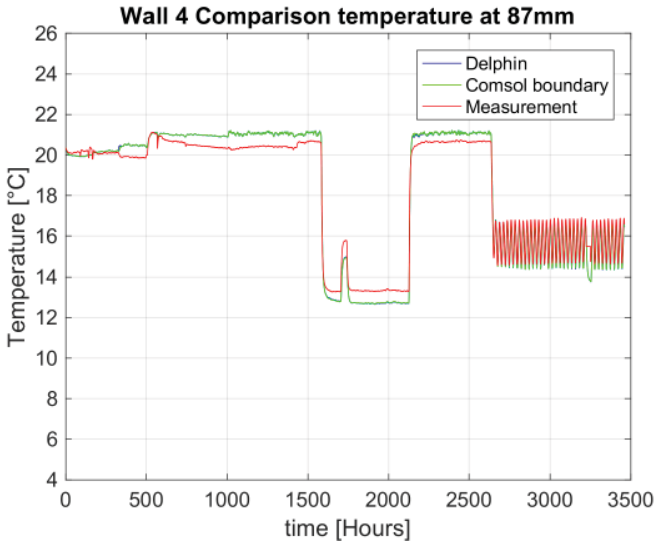

Figure 11.56 T at 87mm. Comparison between Comsol model with implemented flux, adapted boundary conditions and Delphin.

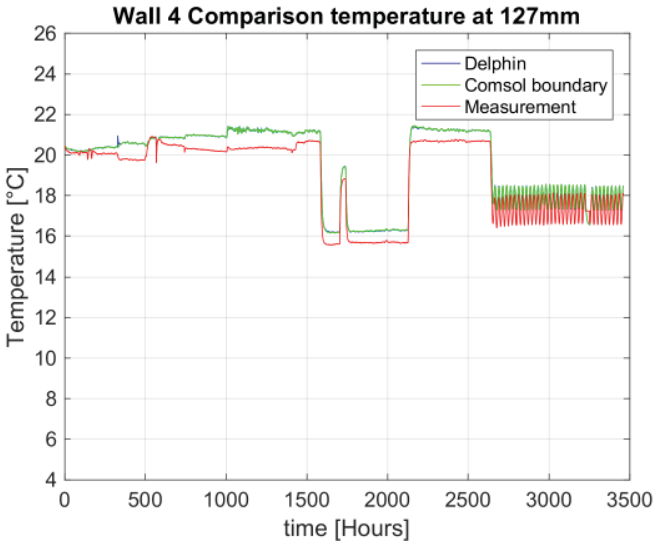

Figure 11.57 T at 127mm. Comparison between Comsol model with implemented flux, adapted boundary conditions and Delphin.

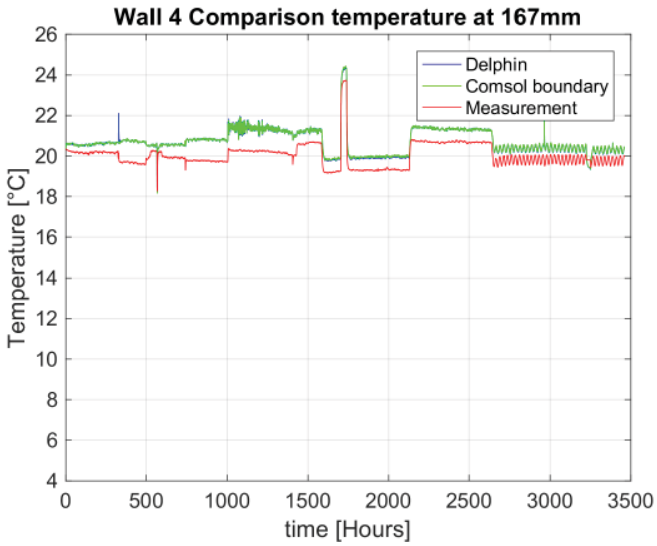

Figure 11.58 T at 167mm. Comparison between Comsol model with implemented flux, adapted boundary conditions and Delphin.

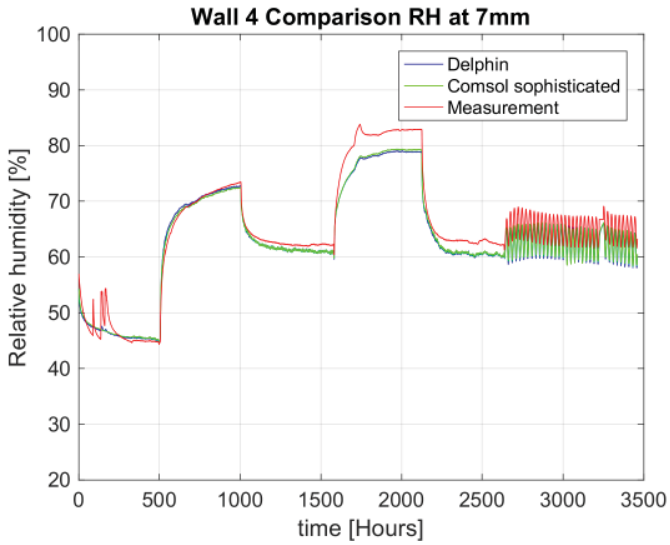

Figure 11.59 RH at 7mm. Comparison Comsol model with seperate flux, adapted boundary conditions and Delphin.

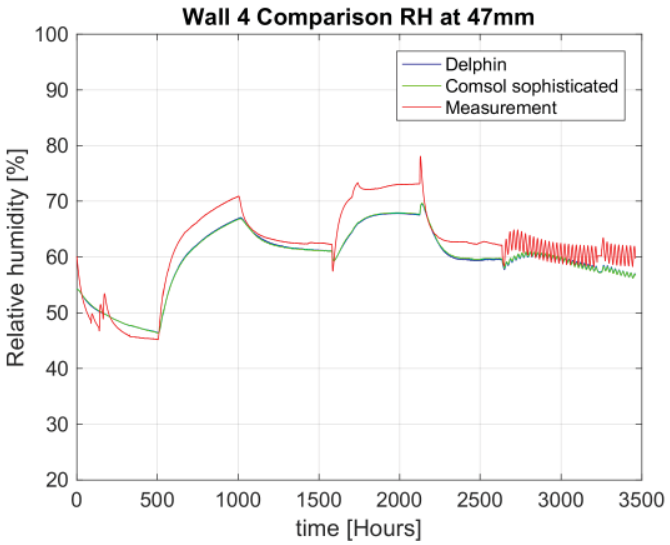

Figure 11.60 RH at 47mm. Comparison Comsol model with seperate flux, adapted boundary conditions and Delphin.

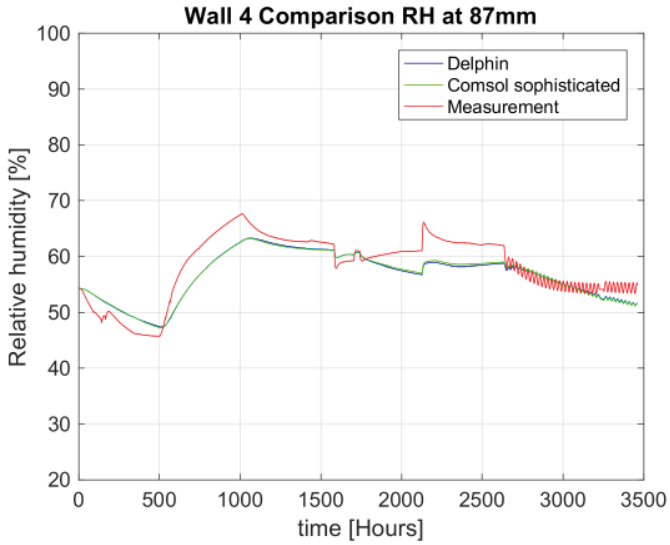

Figure 11.61 RH at 87mm. Comparison Comsol model with seperate flux, adapted boundary conditions and Delphin.

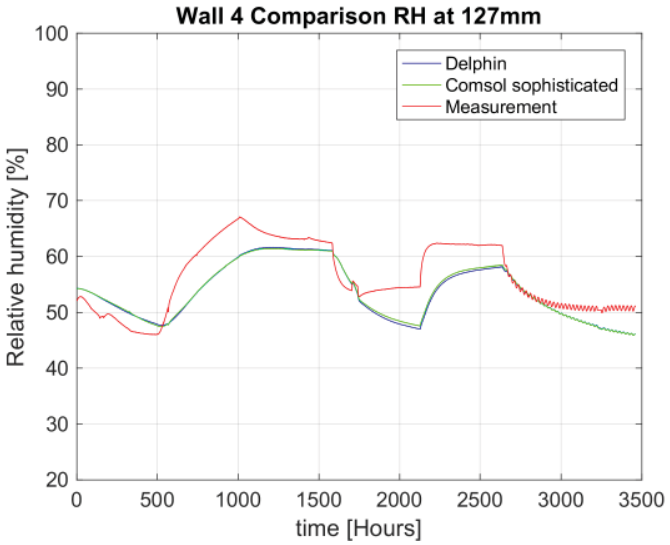

Figure 11.62 RH at 127mm. Comparison Comsol model with seperate flux, adapted boundary conditions and Delphin.

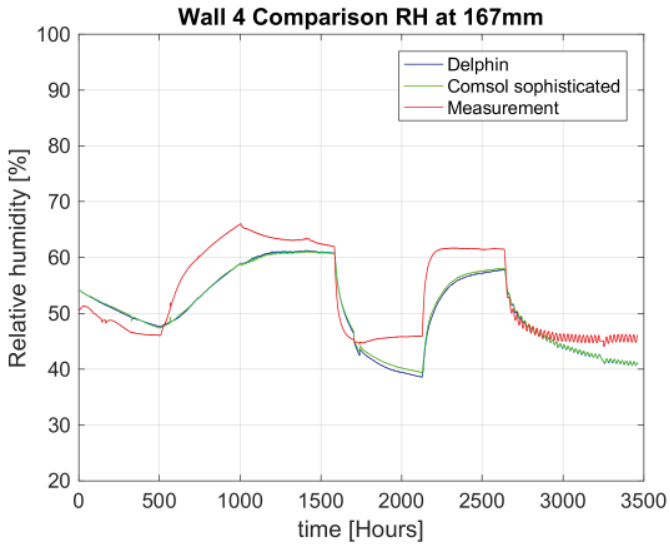

Figure 11.63 RH at 167mm. Comparison Comsol model with seperate flux, adapted boundary conditions and Delphin.

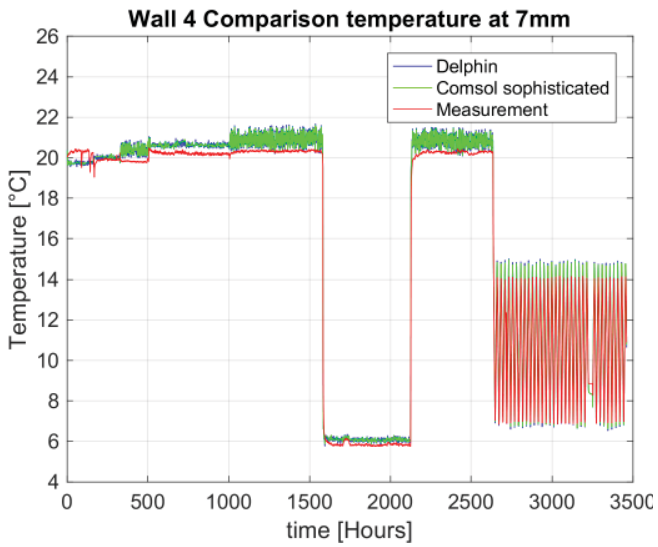

Figure 11.64 T at 7mm. Comparison Comsol model with seperate flux, adapted boundary conditions and Delphin.

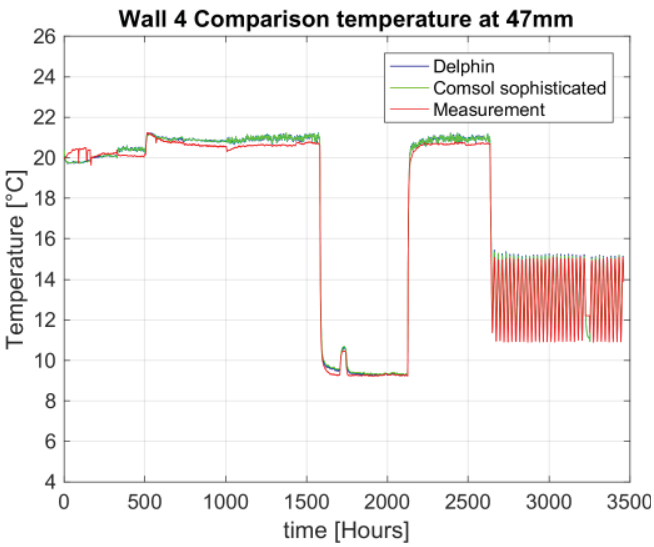

Figure 11.65 T at 47mm. Comparison Comsol model with seperate flux, adapted boundary conditions and Delphin.

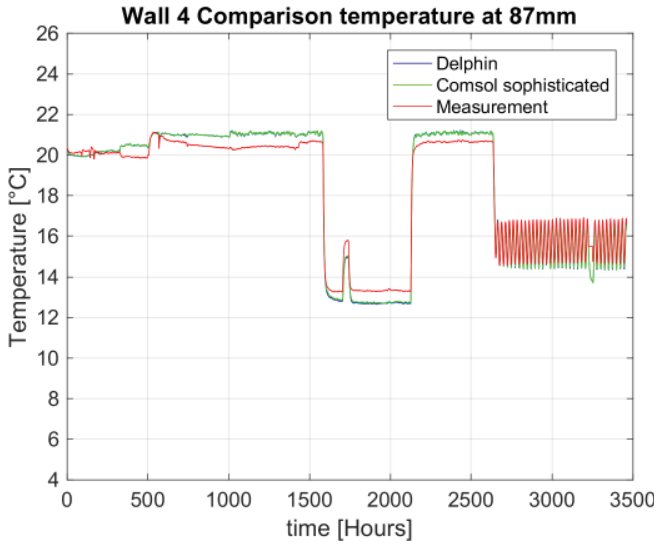

Figure 11.66 T at 87mm. Comparison Comsol model with seperate flux, adapted boundary conditions and Delphin.

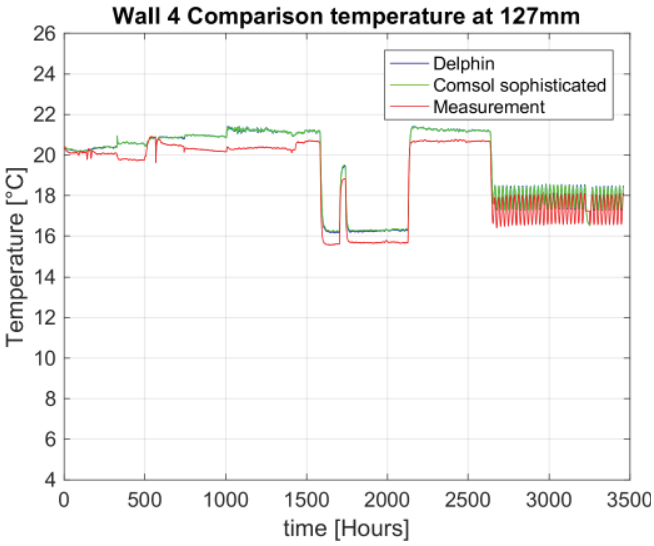

Figure 11.67 T at 127mm. Comparison Comsol model with seperate flux, adapted boundary conditions and Delphin.

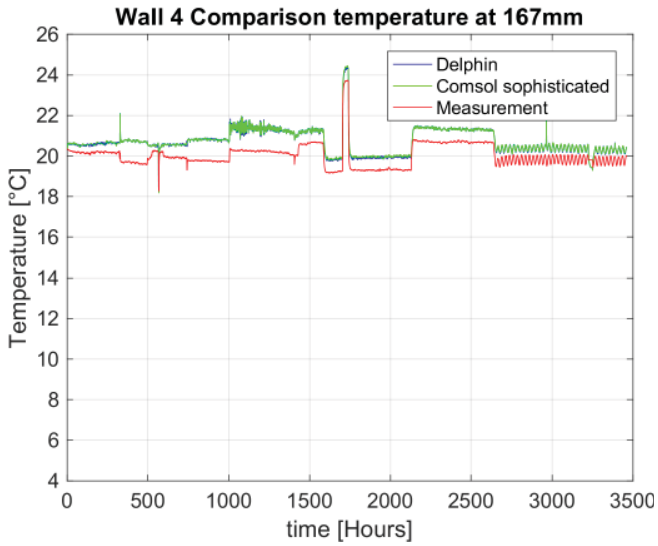

Figure 11.68 T at 167mm. Comparison Comsol model with seperate flux, adapted boundary conditions and Delphin.

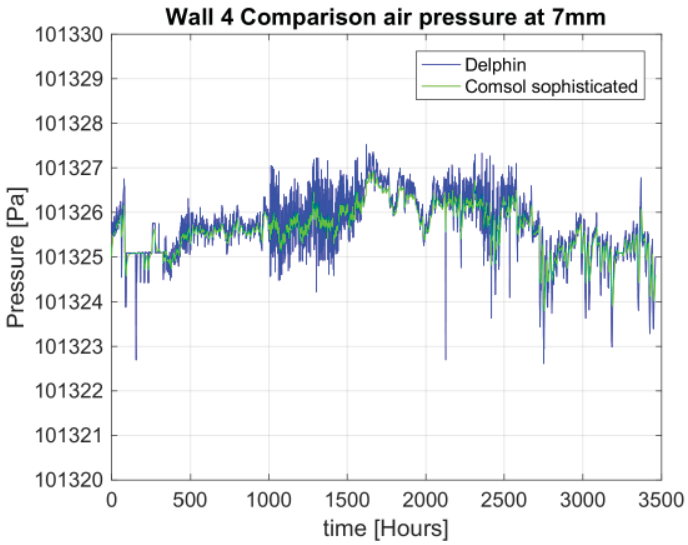

Figure 11.69 p_a at 7mm. Comparison Comsol model with seperate flux, adapted boundary conditions and Delphin.

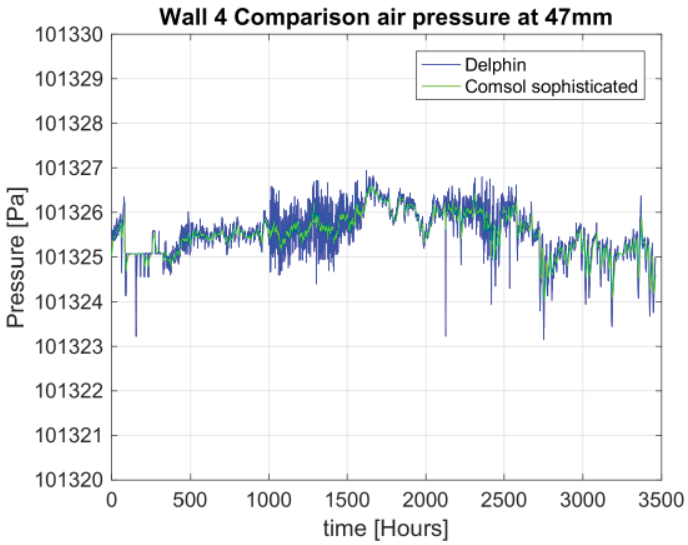

Figure 11.70 p_a at 47mm. Comparison Comsol model with seperate flux, adapted boundary conditions and Delphin.

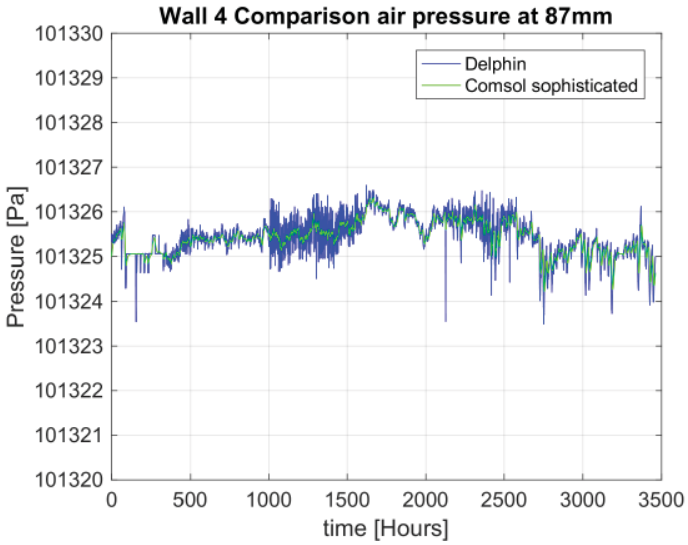

Figure 11.71 p_a at 87mm. Comparison Comsol model with seperate flux, adapted boundary conditions and Delphin.

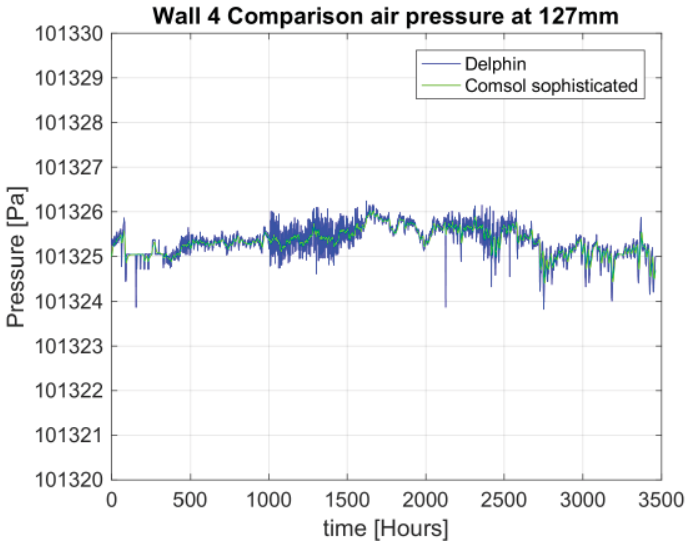

Figure 11.72 p_a at 127mm. Comparison Comsol model with seperate flux, adapted boundary conditions and Delphin.

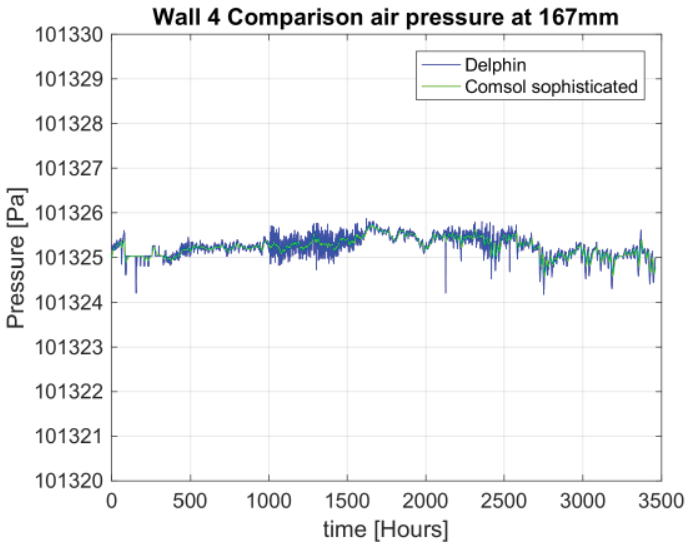

Figure 11.73 p_a at 167mm. Comparison Comsol model with seperate flux, adapted boundary conditions and Delphin.

Appendix V

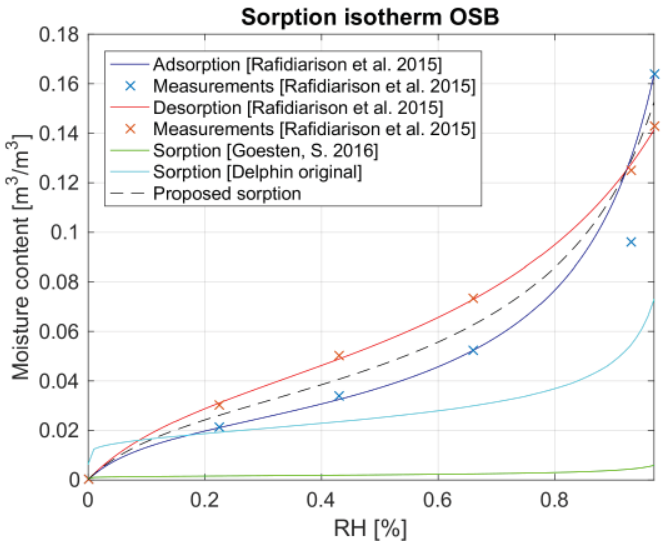

Figure 11.74 Material properties OSB. Comparison sorption isotherm $w(\varphi)$ *in hygroscopic range.*

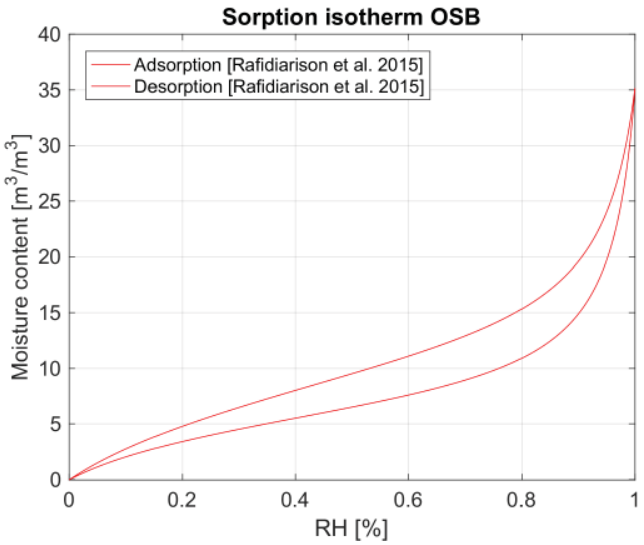

Figure 11.75 Material properties OSB. Comparison sorption isotherm $w(\varphi)$ *in whole moisture range.*

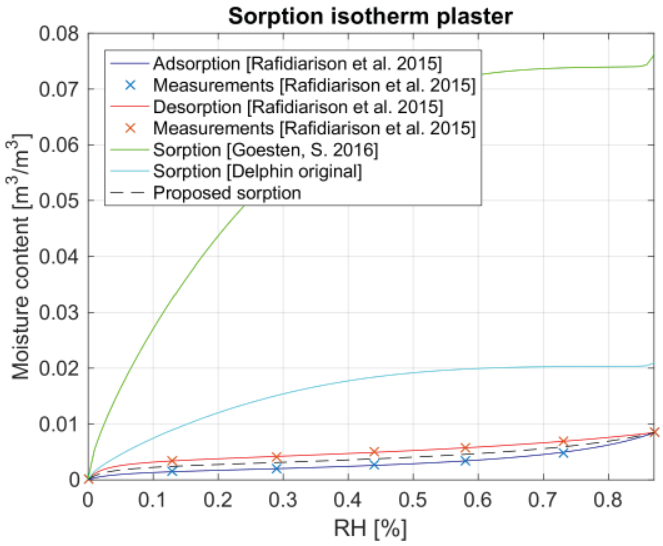

Figure 11.76 Material properties lime plaster. Comparison sorption isotherm $w(\varphi)$ *in hygroscopic range.*

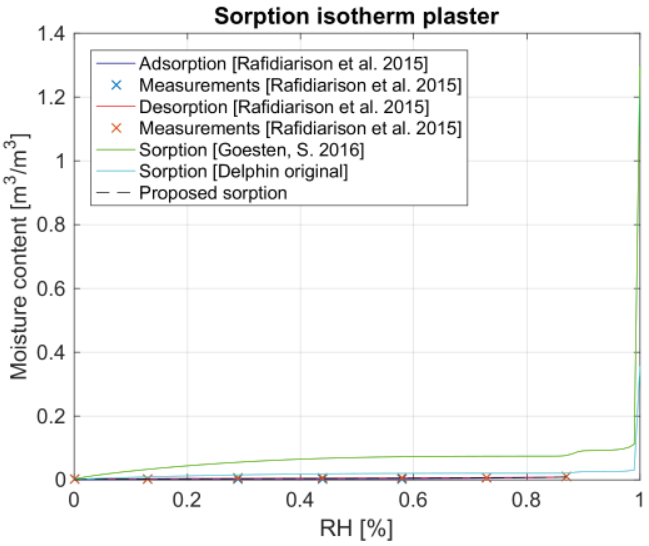

Figure 11.77 Material properties lime plaster. Comparison sorption isotherm $w(\varphi)$ *in whole moisture range.*

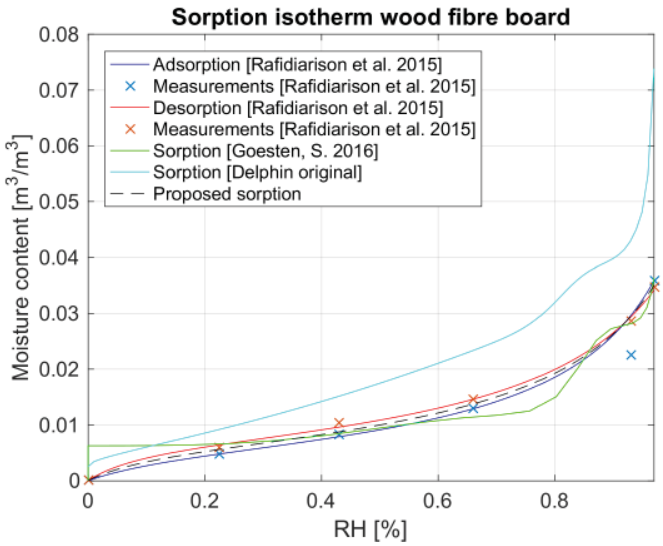

Figure 11.78 Material properties wood fibre. Comparison sorption isotherm $w(\varphi)$ *in hygroscopic range.*

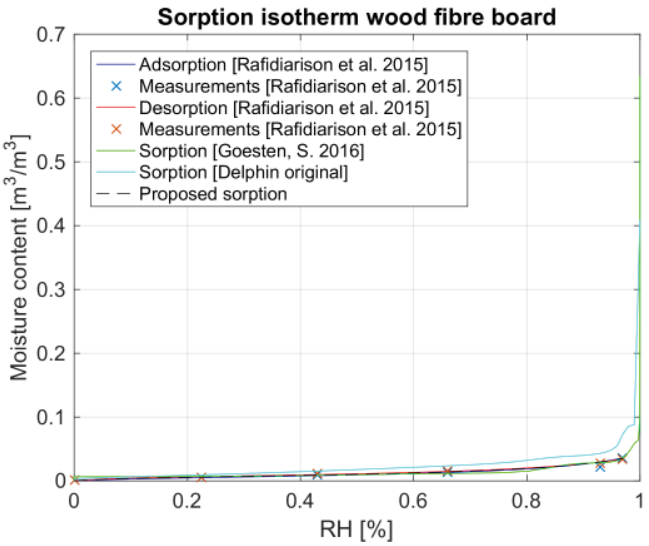

Figure 11.79 Material properties wood fibre. Comparison sorption isotherm $w(\varphi)$ *in whole moisture range.*

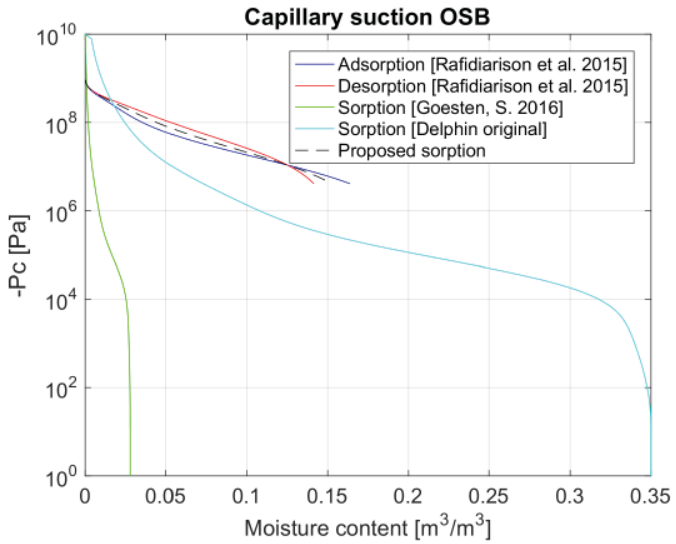

Figure 11.80 Material properties OSB. Comparison capillary suction $p_c(w)$.

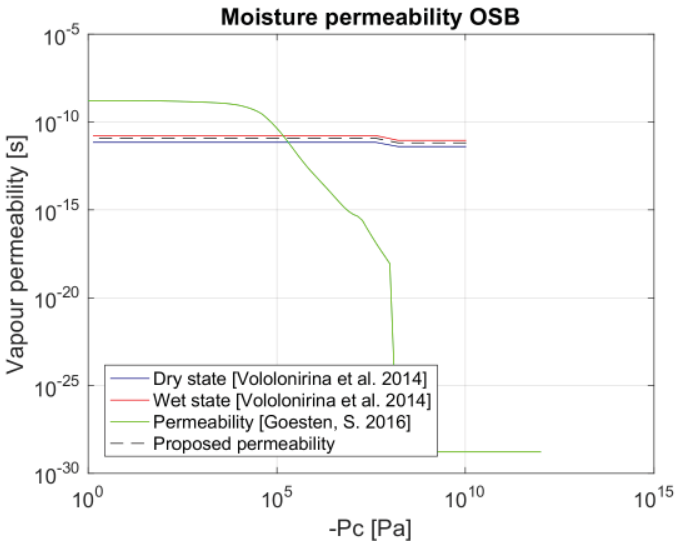

Figure 11.81 Material properties OSB. Comparison moisture permeability $k_l(p_c)$.

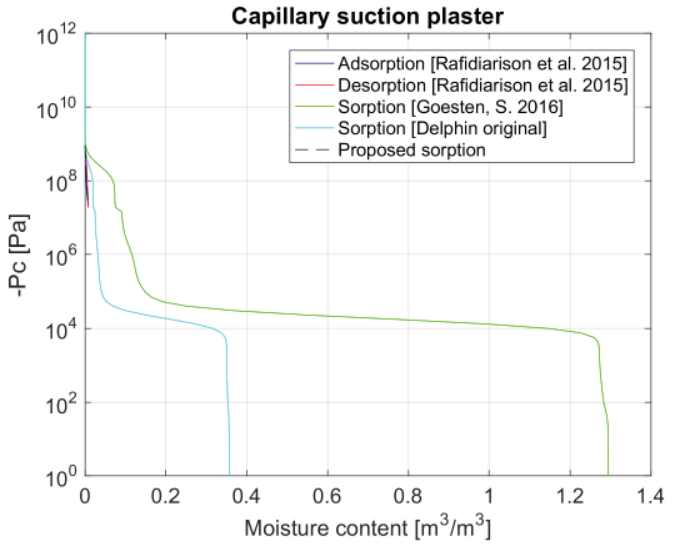

Figure 11.83 Material properties lime plaster. Comparison capillary suction $p_c(w)$.

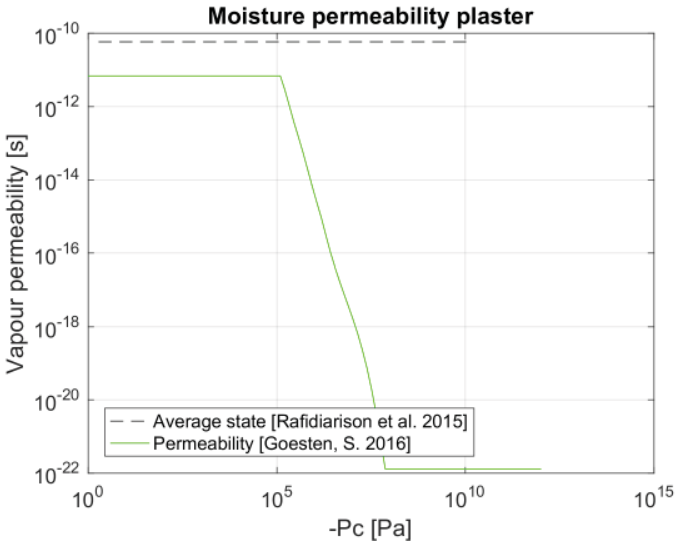

Figure 11.82 Material properties lime plaster. Comparison moisture permeability $k_l(p_c)$.

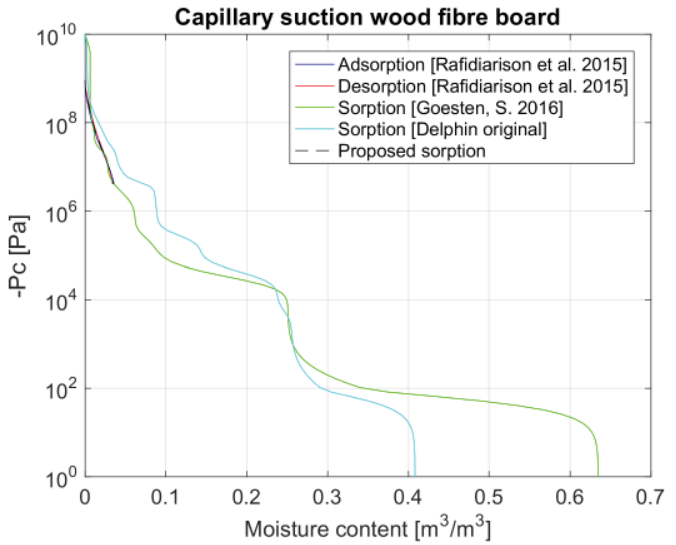

Figure 11.84 Material properties wood fibre. Comparison capillary suction $p_c(w)$.

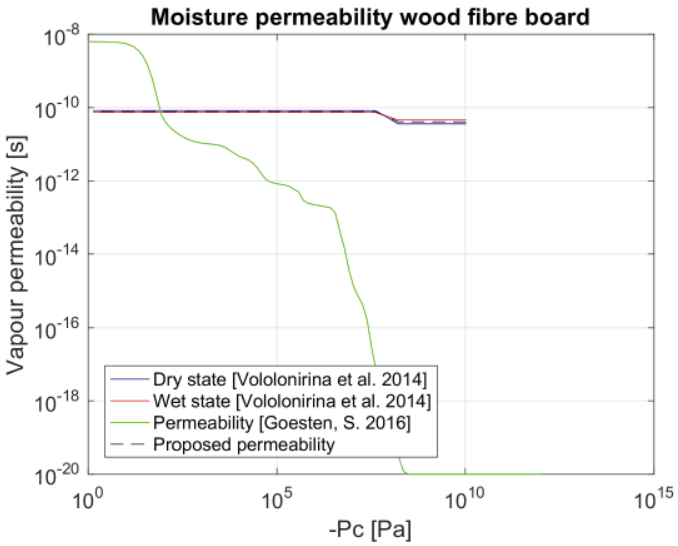

Figure 11.85 Material properties wood fibre. Comparison moisture permeability $k_l(p_c)$.

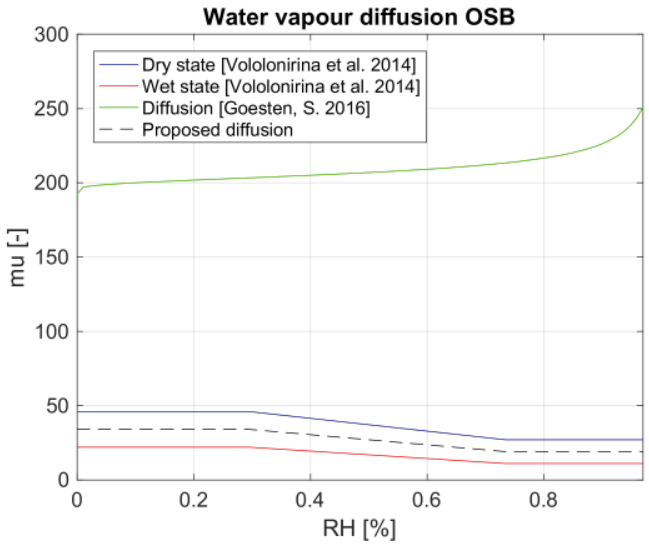

Figure 11.86 Material properties OSB. Comparison vapour diffusion $\mu(\varphi)$ in hygroscopic range.

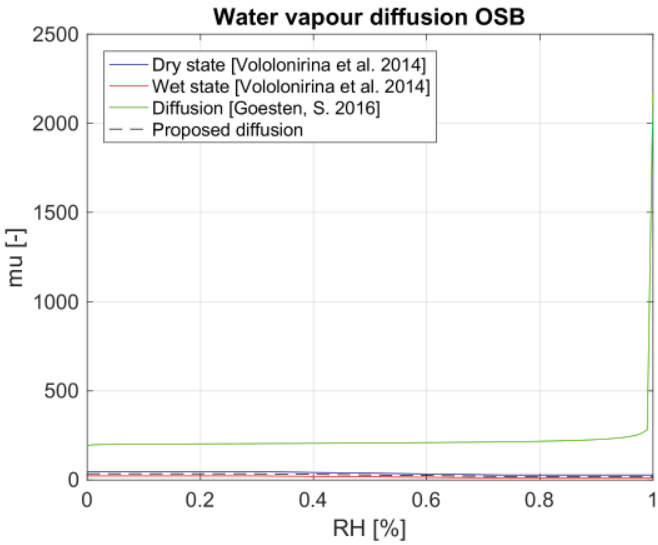

Figure 11.87 Material properties OSB. Comparison vapour diffusion $\mu(\varphi)$ in whole moisture range.

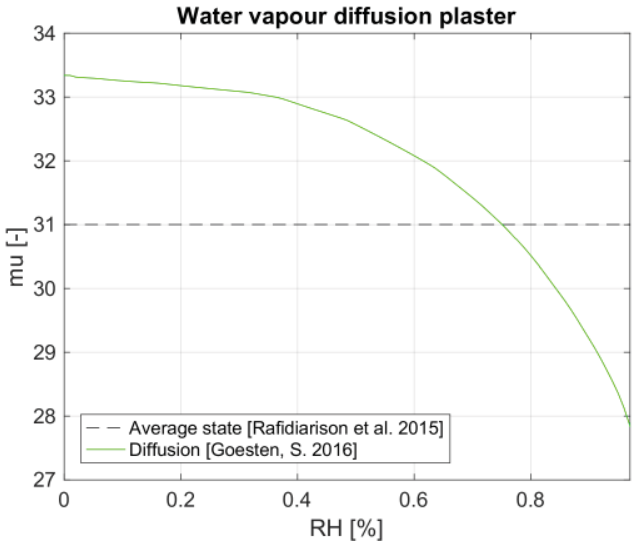

Figure 11.88 Material properties lime plaster. Comparison vapour diffusion $\mu(\varphi)$ in hygroscopic range.

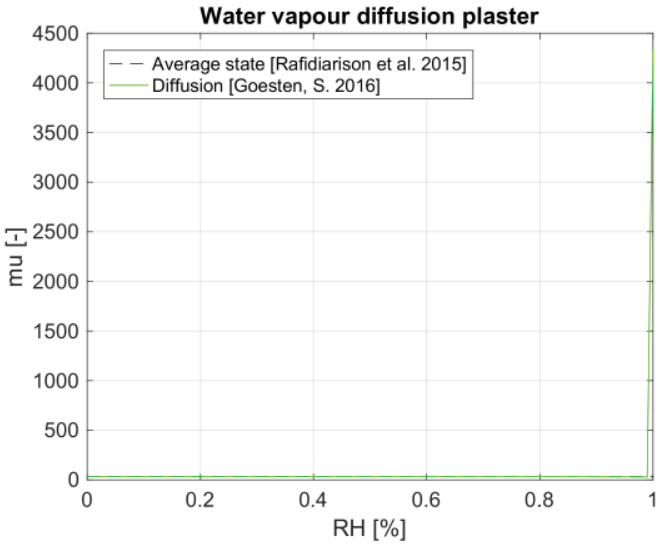

Figure 11.89 Material properties lime plaster. Comparison vapour diffusion $\mu(\varphi)$ in whole moisture range.

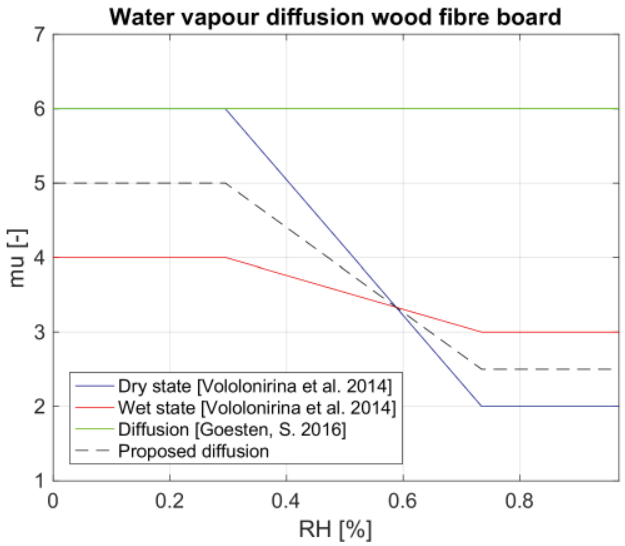

Figure 11.90 Material properties wood fibre. Comparison vapour diffusion $\mu(\varphi)$ in hygroscopic range.

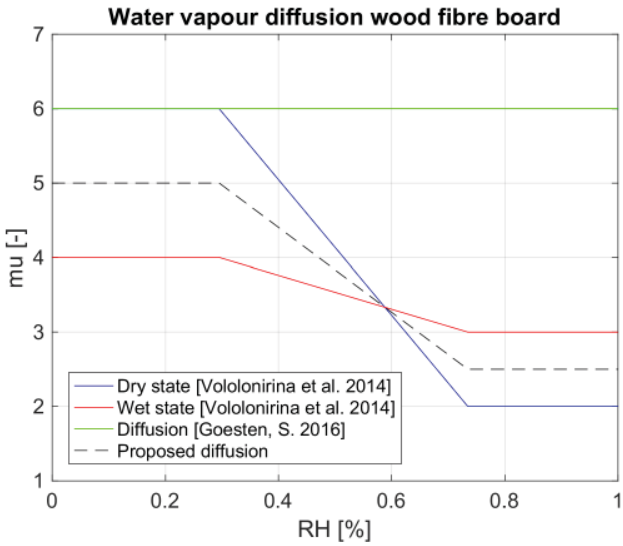

Figure 11.91 Material properties wood fibre. Comparison vapour diffusion $\mu(\varphi)$ in whole moisture range.

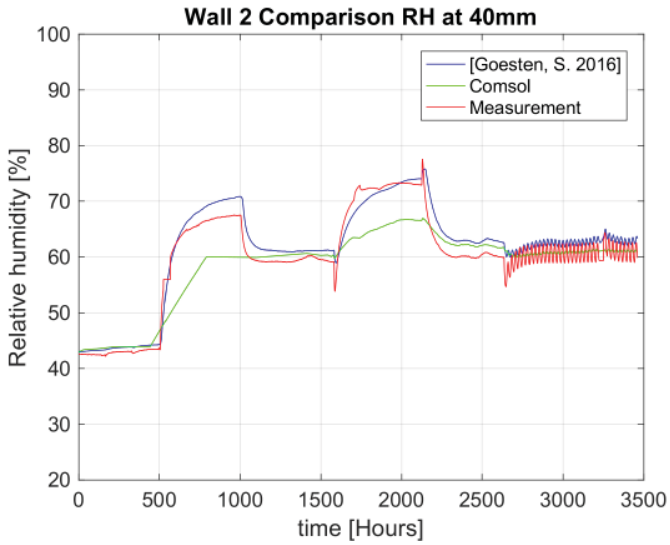

Figure 11.92 RH at 40mm. Comparison Comsol model with material data from Rafidiarison et al. [2015]; Comsol model of Goesten, S. [2016] and measurements.

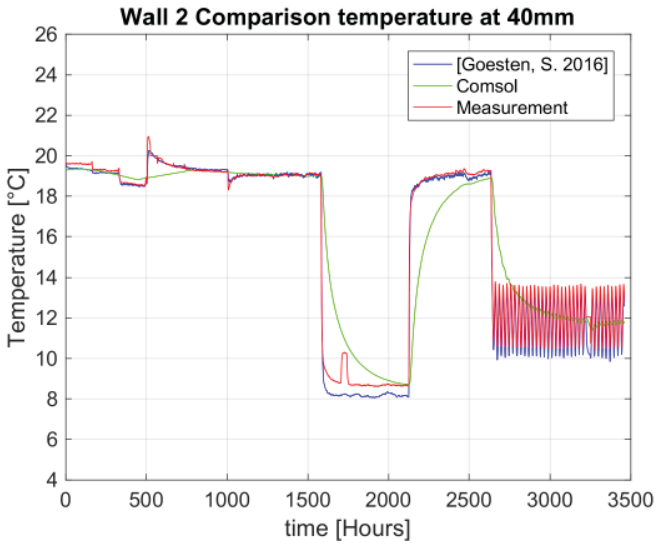

Figure 11.93 T at 40mm. Comparison Comsol model with material data from Rafidiarison et al. [2015]; Comsol model of Goesten, S. [2016] and measurements.

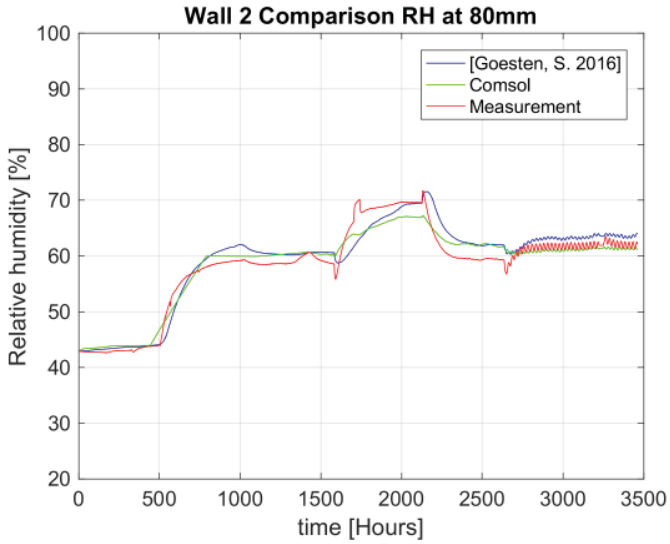

Figure 11.94 RH at 80mm. Comparison Comsol model with material data from Rafidiarison et al. [2015]; Comsol model of Goesten, S. [2016] and measurements.

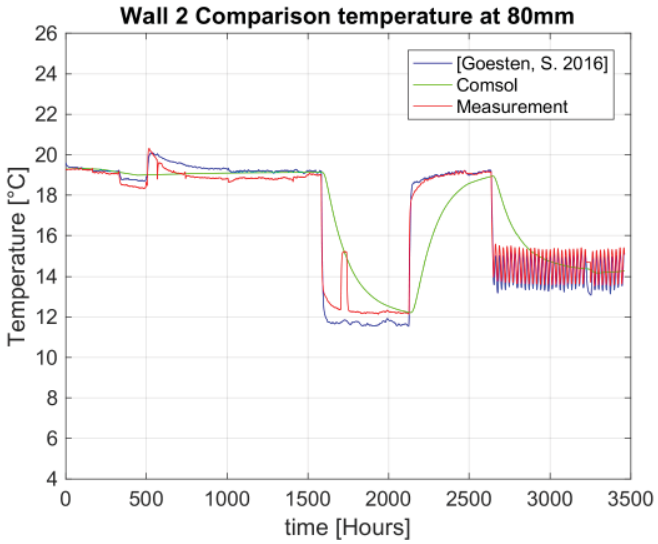

Figure 11.95 T at 80mm. Comparison Comsol model with material data from Rafidiarison et al. [2015]; Comsol model of Goesten, S. [2016] and measurements.

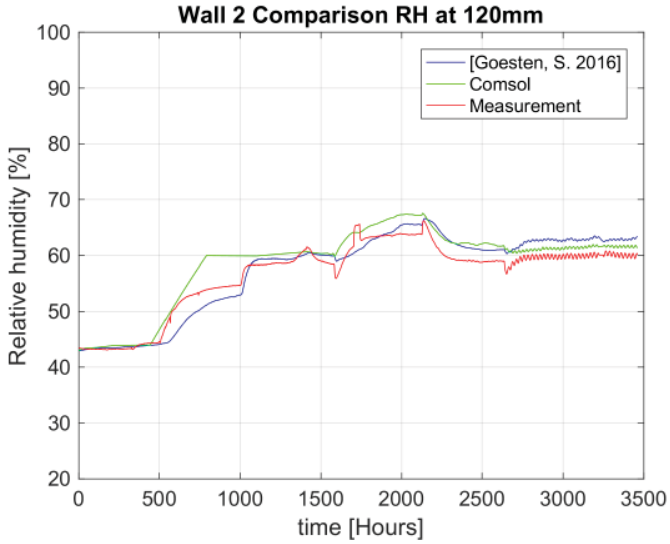

Figure 11.96 RH at 120mm. Comparison Comsol model with material data from Rafidiarison et al. [2015]; Comsol model of Goesten, S. [2016] and measurements.

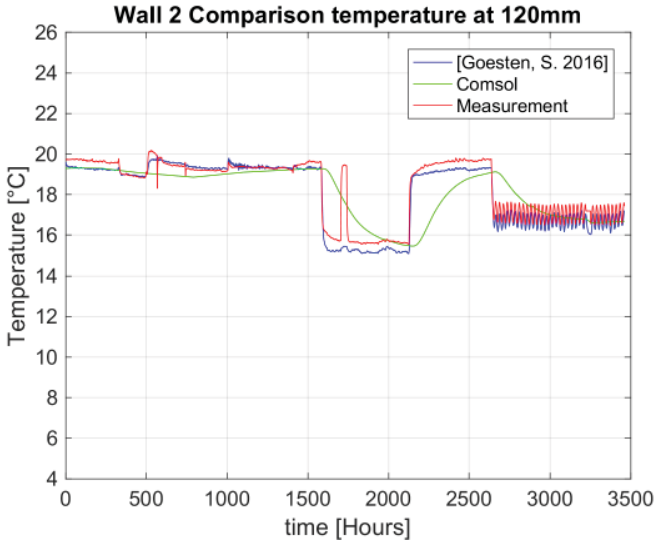

Figure 11.97 T at 120mm. Comparison Comsol model with material data from Rafidiarison et al. [2015]; Comsol model of Goesten, S. [2016] and measurements.

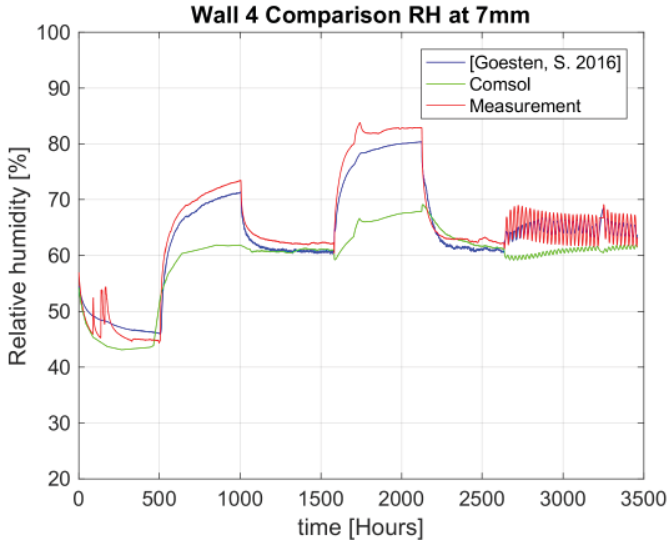

Figure 11.98 RH at 7mm. Comparison Comsol model with material data from Rafidiarison et al. [2015]; Comsol model of Goesten, S. [2016] and measurements.

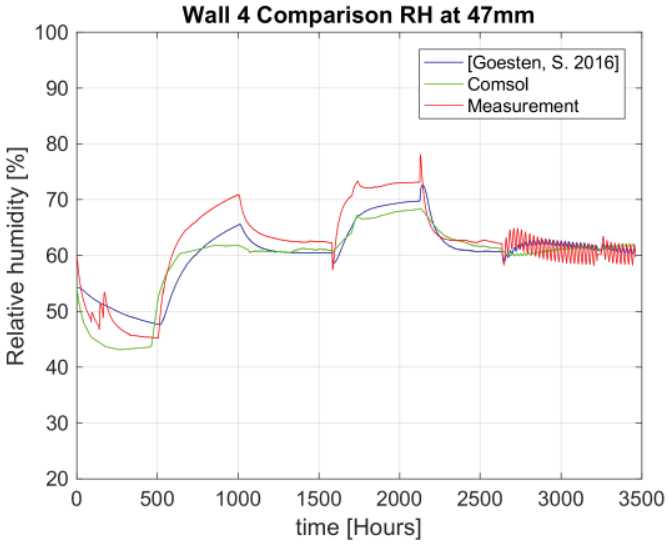

Figure 11.99 RH at 47mm. Comparison Comsol model with material data from Rafidiarison et al. [2015]; Comsol model of Goesten, S. [2016] and measurements.

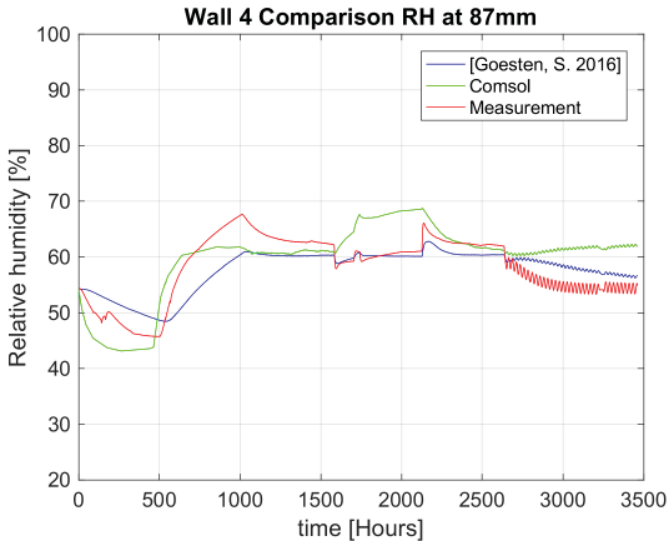

Figure 11.100 RH at 87mm. Comparison Comsol model with material data from Rafidiarison et al. [2015]; Comsol model of Goesten, S. [2016] and measurements.

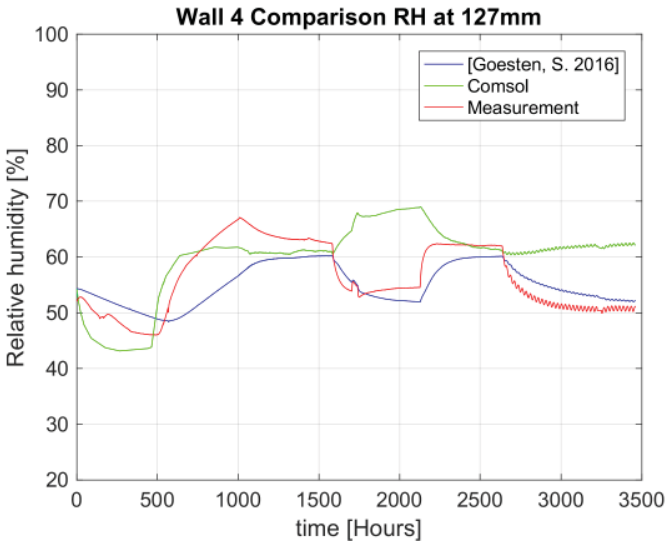

Figure 11.101 RH at 127mm. Comparison Comsol model with material data from Rafidiarison et al. [2015]; Comsol model of Goesten, S. [2016] and measurements.

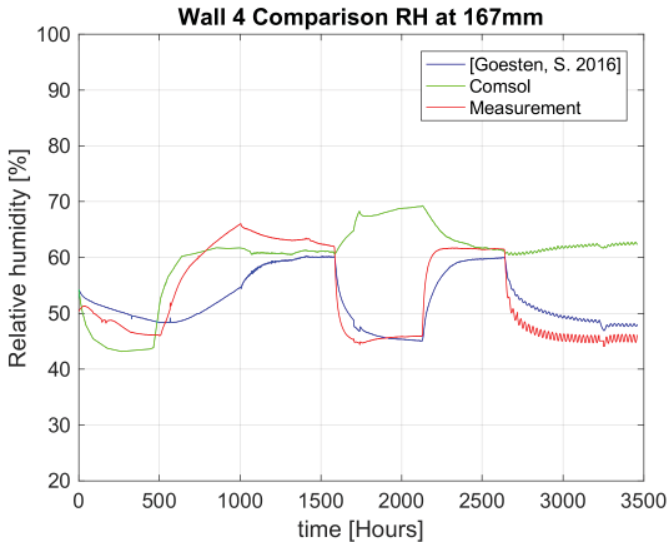

Figure 11.102 RH at 167mm. Comparison Comsol model with material data from Rafidiarison et al. [2015]; Comsol model of Goesten, S. [2016] and measurements.

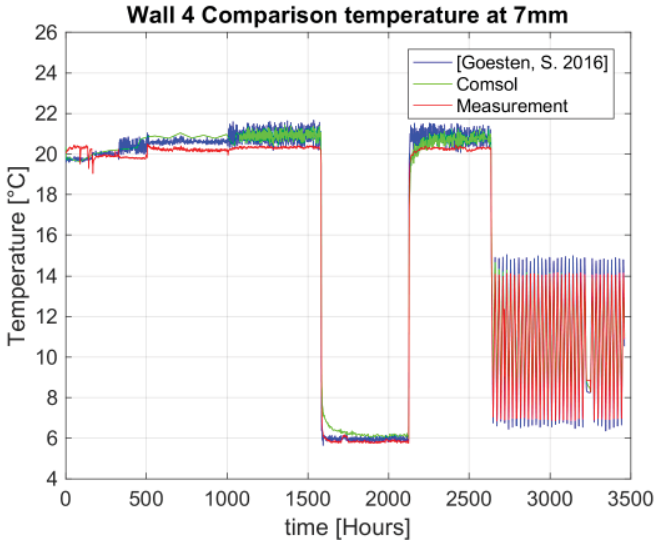

Figure 11.103 T at 7mm. Comparison Comsol model with material data from Rafidiarison et al. [2015]; Comsol model of Goesten, S. [2016] and measurements.

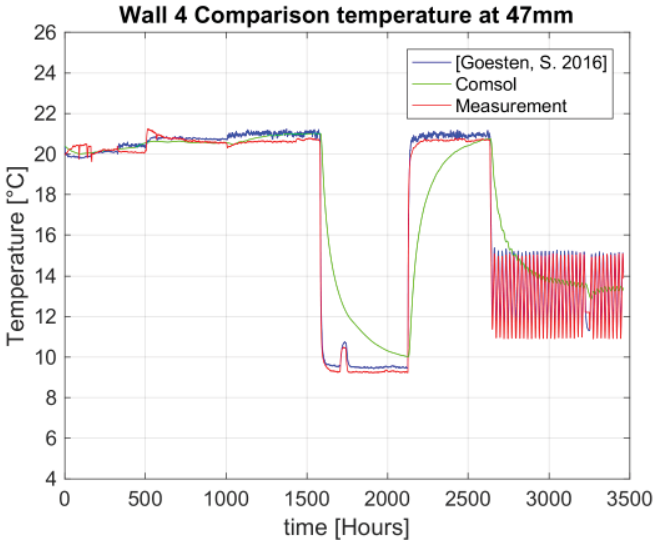

Figure 11.104 T at 47mm. Comparison Comsol model with material data from Rafidiarison et al. [2015]; Comsol model of Goesten, S. [2016] and measurements.

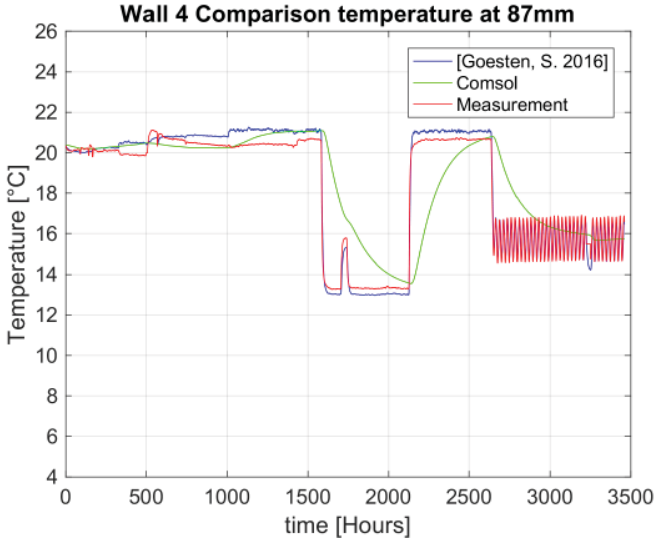

Figure 11.105 T at 87mm. Comparison Comsol model with material data from Rafidiarison et al. [2015]; Comsol model of Goesten, S. [2016] and measurements.

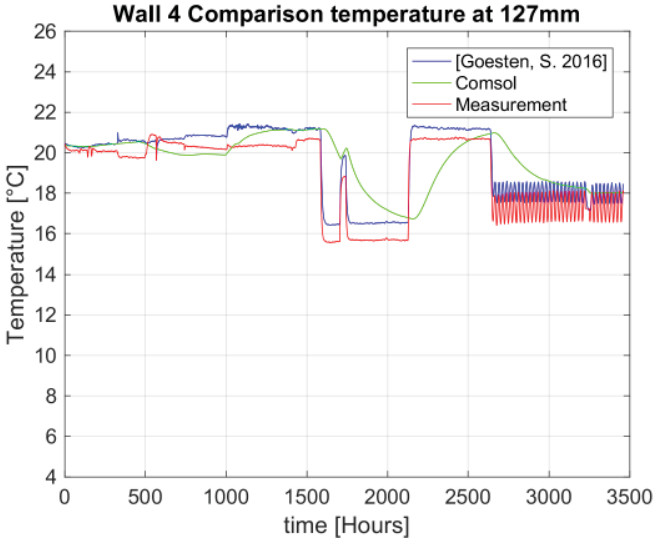

Figure 11.106 T at 127mm. Comparison Comsol model with material data from Rafidiarison et al. [2015]; Comsol model of Goesten, S. [2016] and measurements.

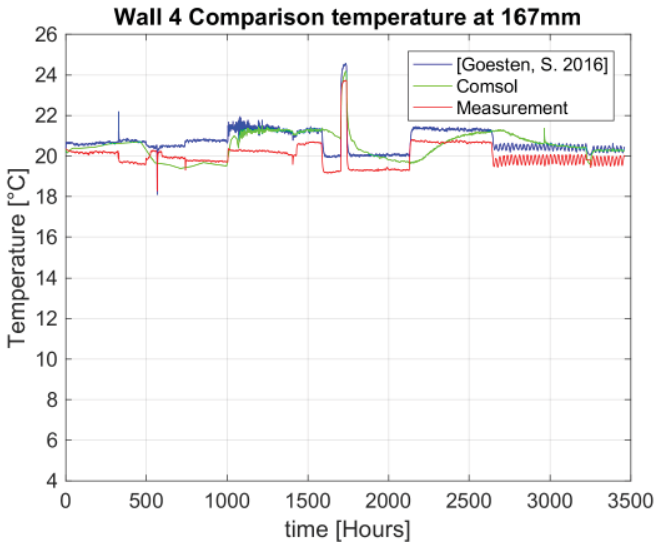

Figure 11.107 T at 167mm. Comparison Comsol model with material data from Rafidiarison et al. [2015]; Comsol model of Goesten, S. [2016] and measurements.

Appendix VII

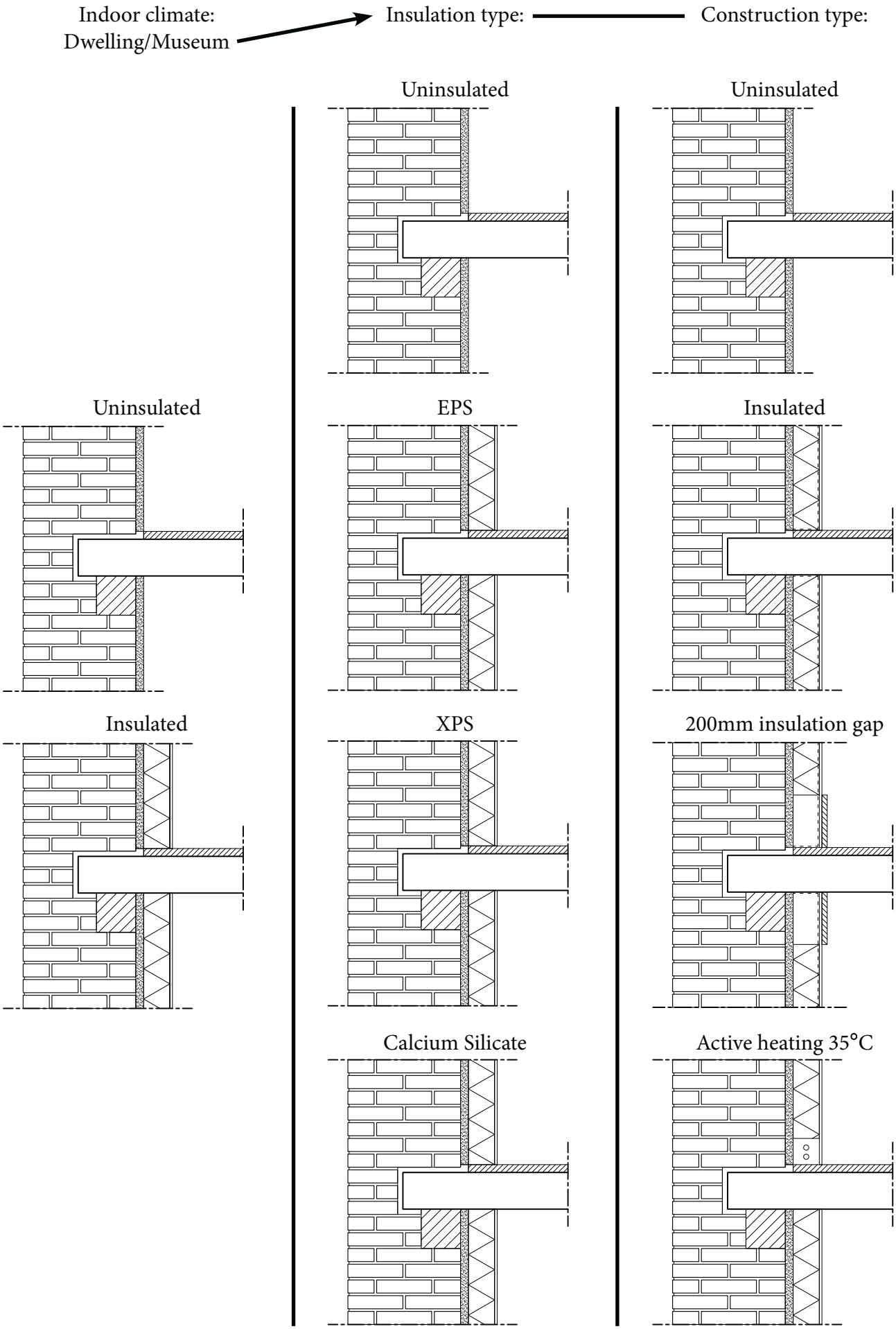

Figure 11.108 Variants of the case study that are simulated. Devided over three different categories.

Appendix VIII

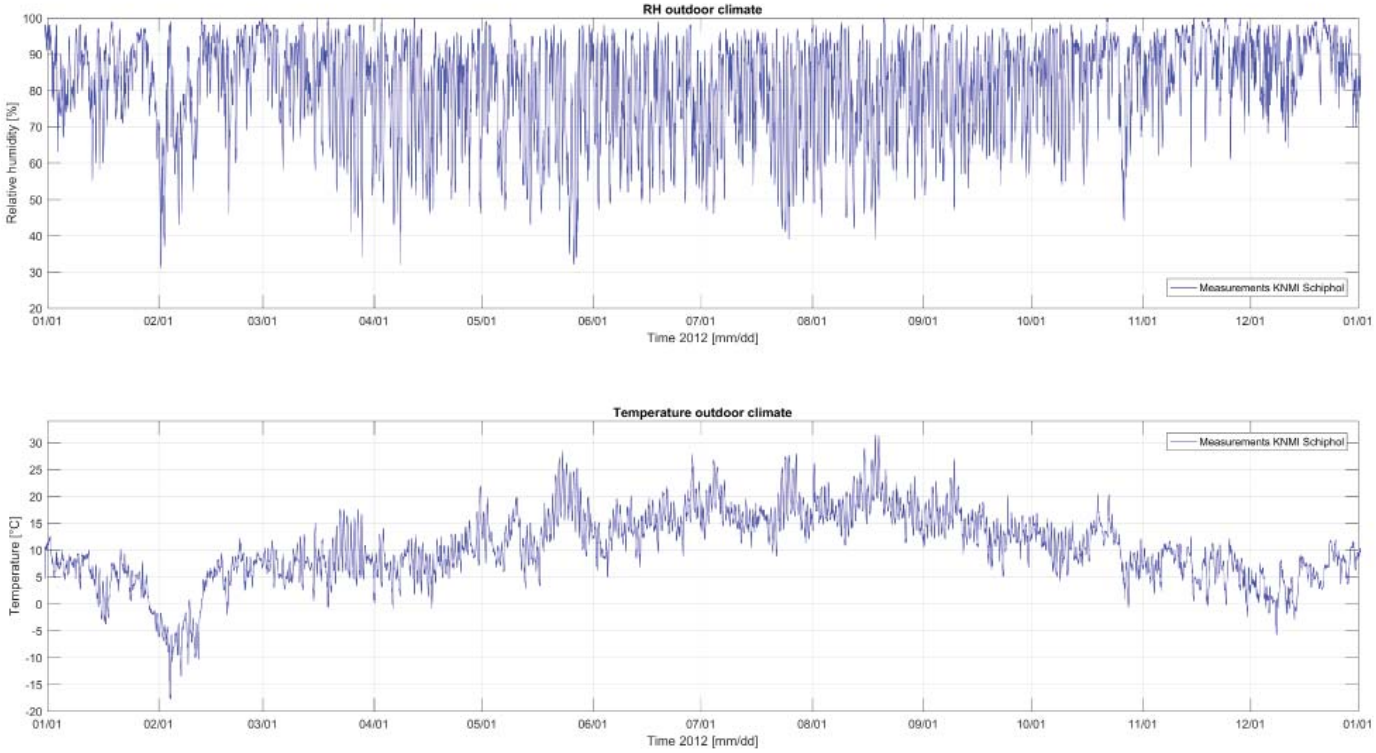

Figure 11.109 Relative humidity and temperature of the outdoor climate. Results from the meteorological station at Schiphol are extracted from measurement data provided by the KNMI.

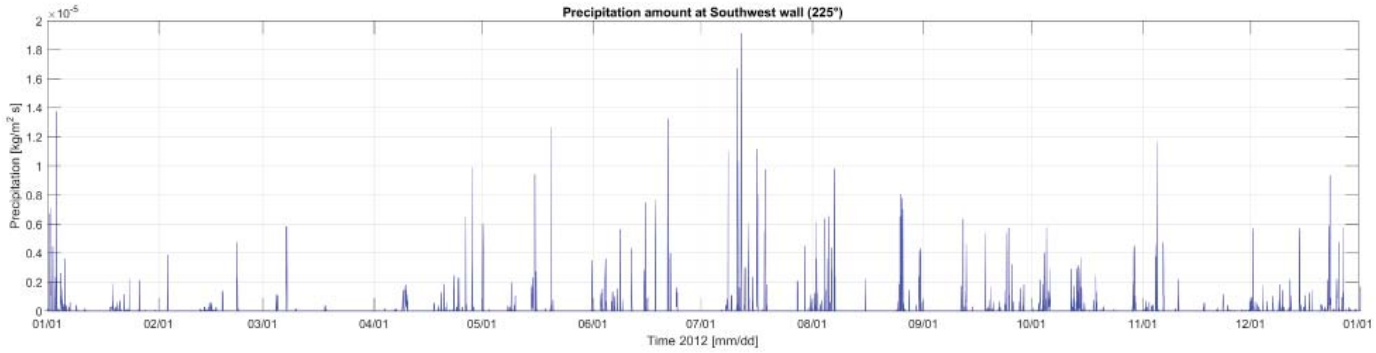

Figure 11.110 Calculated wind-driven rain at the Southwest wall. Based at wind direction and wind speed measurements from the meteorological station at Schiphol. A catch-ratio of 0,3 is also included.

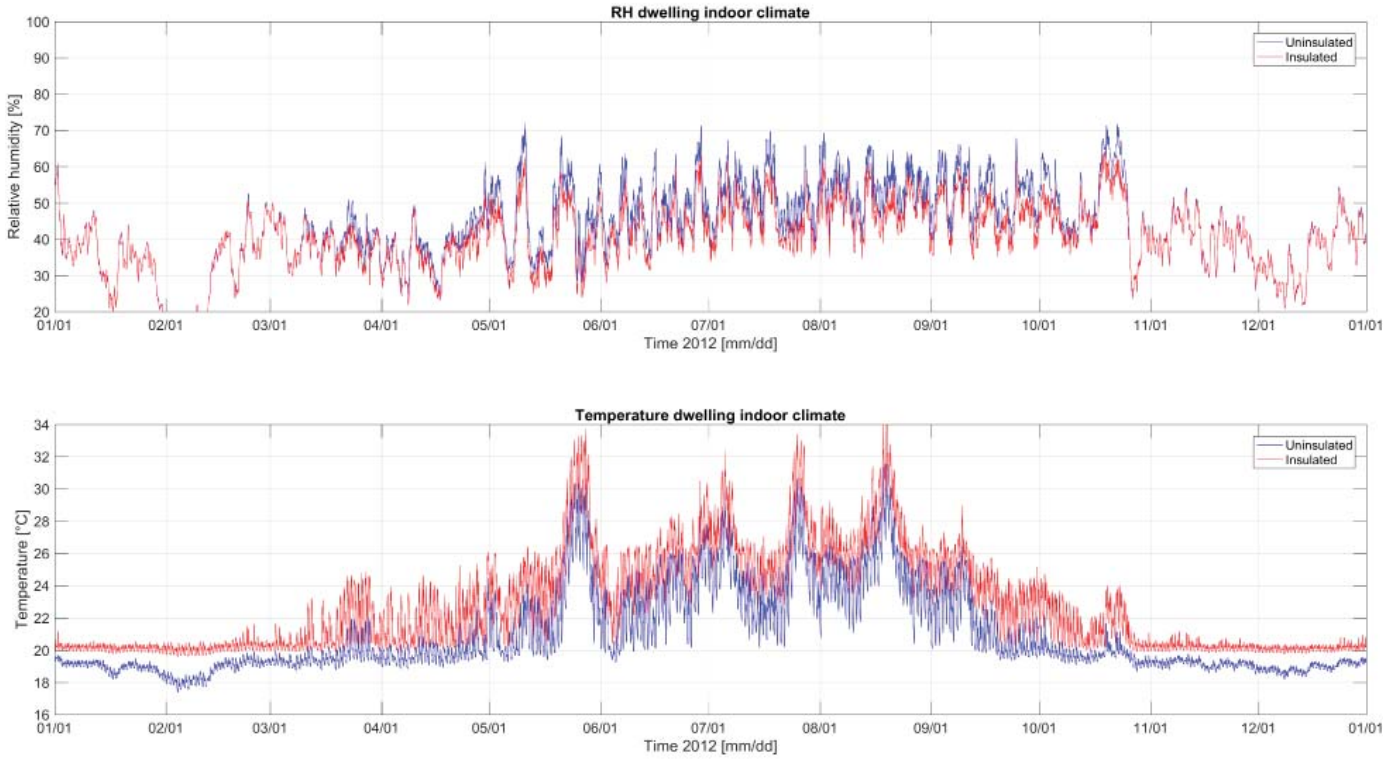

Figure 11.111 Relative humidity and temperature of the calculated indoor climate using HAMBASE. Indoor climate of the dwelling is calculated for both the uninsulated and insulated situation.

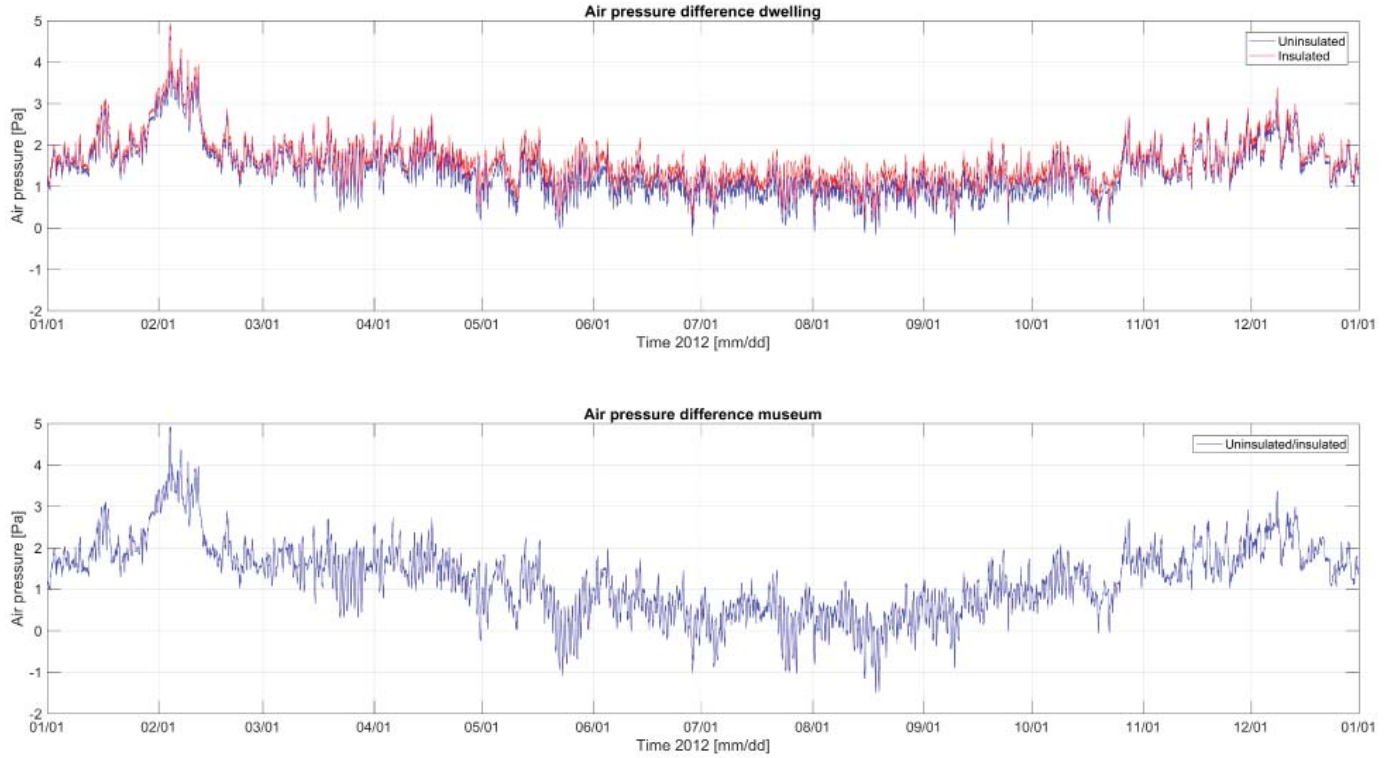

Figure 11.112 Air pressure difference between indoor and outdoor. A positive air pressure difference means that there is an overpressure situation at the interior. The air pressure depends at the temperature difference, therefore different results are used for the dwelling (uninsulated and insulated) and for the museum climate.

Appendix IX

Uninsulated indoor climate

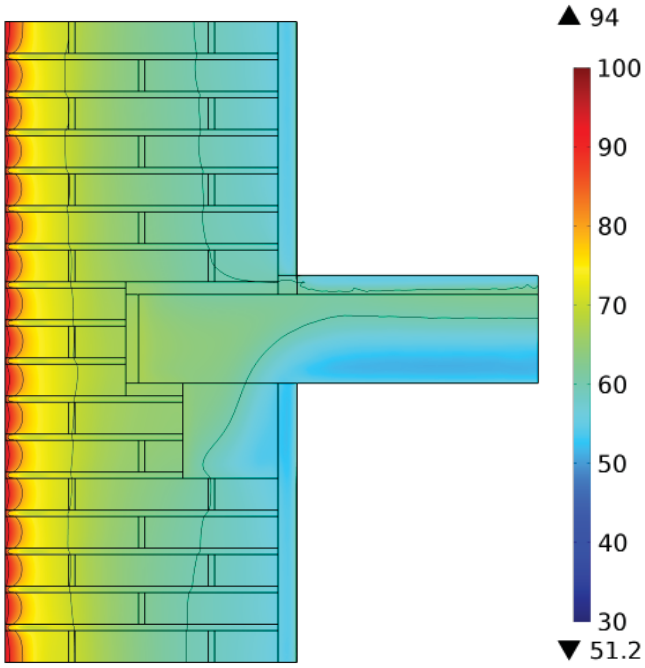

Figure 11.113 Relative humidity of an uninsulated wall with a dwelling indoor climate, at the 25th of July 2012 during a rain event. Each contour line represents a difference of 10%.

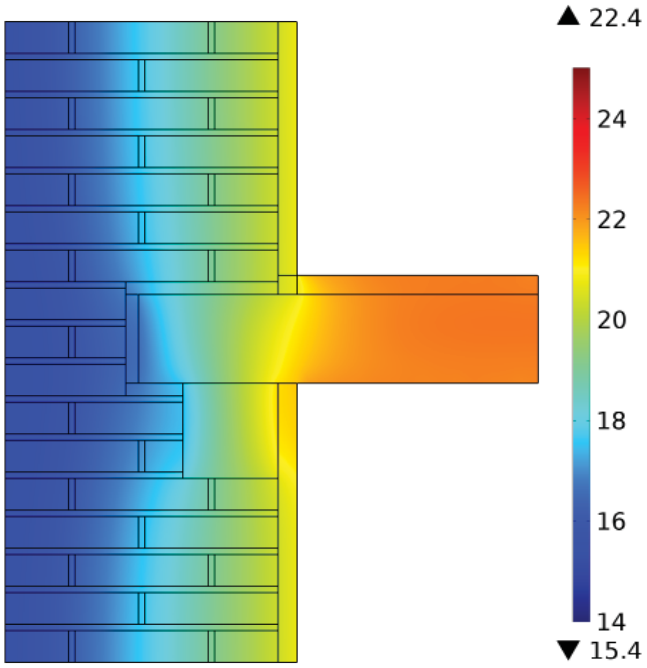

Figure 11.114 Temperature of an uninsulated wall with a dwelling indoor climate, at the 25th of July 2012 during a rain event.

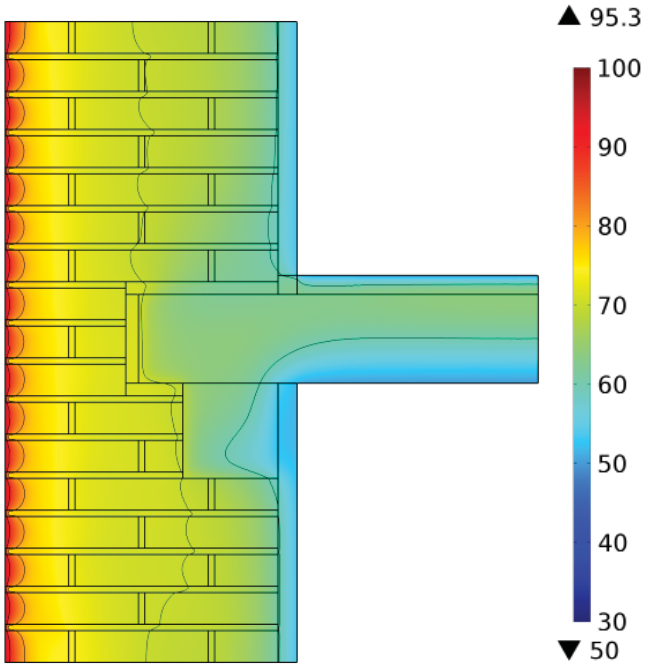

Figure 11.115 Relative humidity of an uninsulated wall with a museum indoor climate, at the 25th of July 2012 during a rain event. Each contour line represents a difference of 10%.

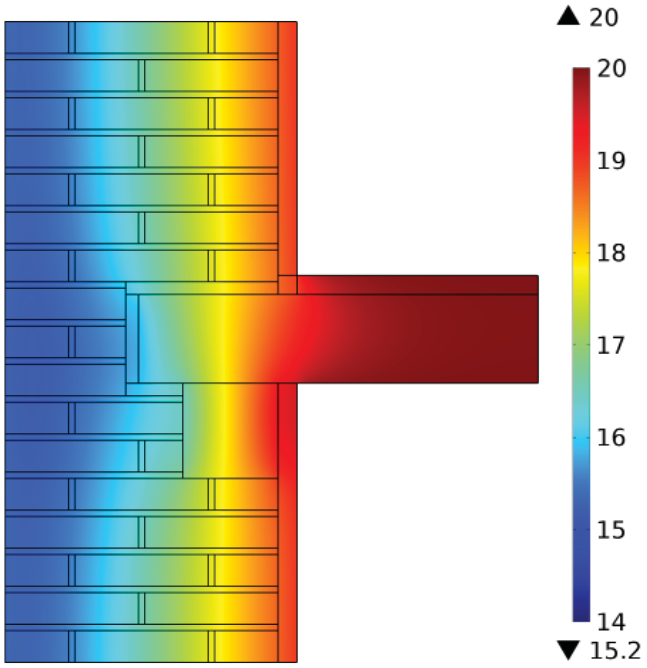

Figure 11.116 Temperature of an uninsulated wall with a museum indoor climate, at the 25th of July 2012 during a rain event.

Insulated indoor climate

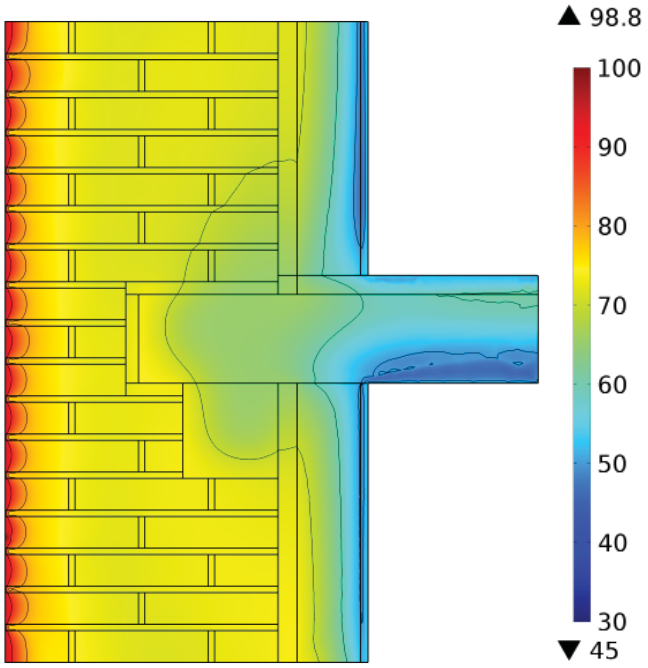

Figure 11.117 Relative humidity of an insulated wall with EPS and a dwelling indoor climate, at the 25th of July 2012 during a rain event. Each contour line represents a difference of 10%.

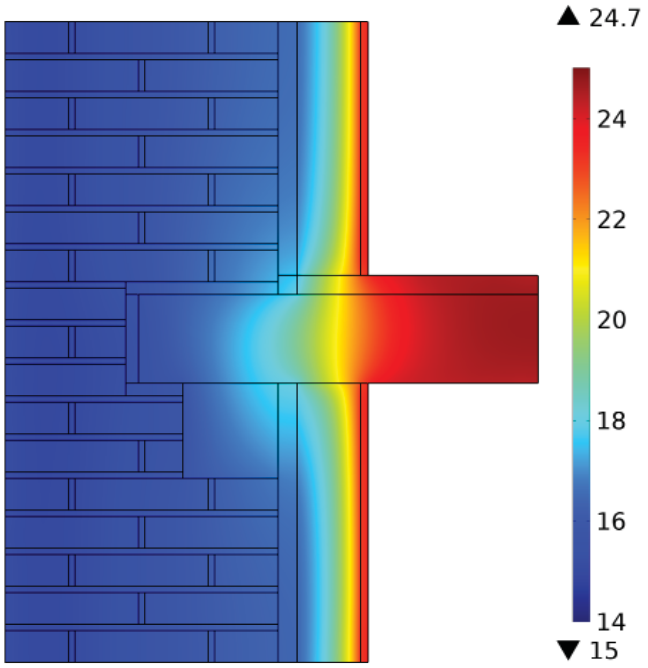

Figure 11.118 Temperature of an insulated wall with EPS and a dwelling indoor climate, at the 25th of July 2012 during a rain event.

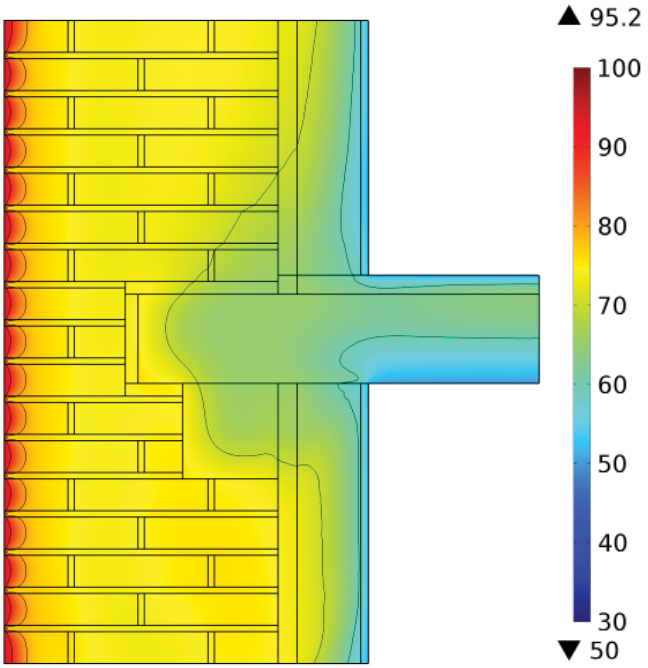

Figure 11.119 Relative humidity of an insulated wall with EPS and a museum indoor climate, at the 25th of July 2012 during a rain event. Each contour line represents a difference of 10%.

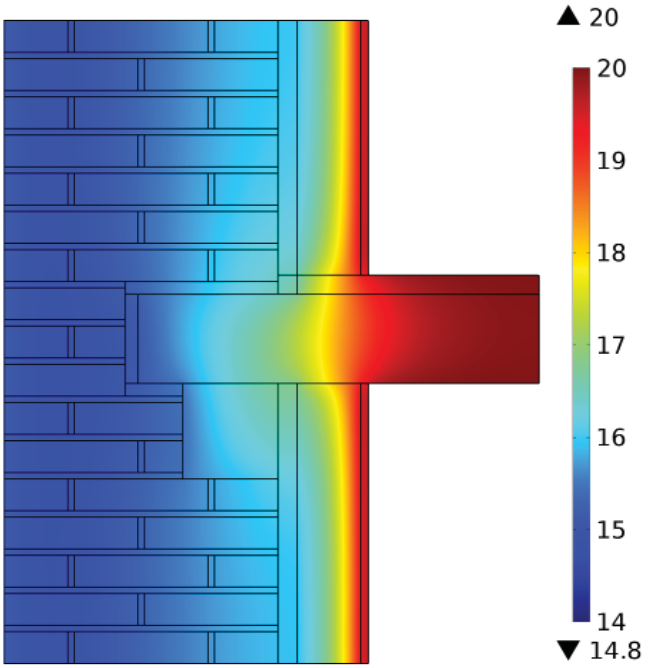

Figure 11.120 Temperature of an insulated wall with EPS and a museum indoor climate, at the 25th of July 2012 during a rain event.

Insulated indoor climate

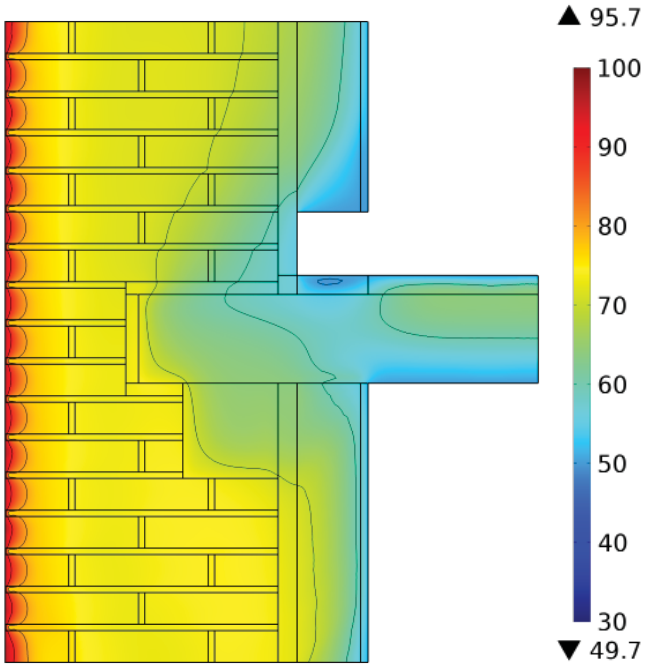

Figure 11.121 Relative humidity of an insulated wall with EPS, active heating and a museum indoor climate, at the 25th of July 2012 during a rain event. Each contour line represents a difference of 10%.

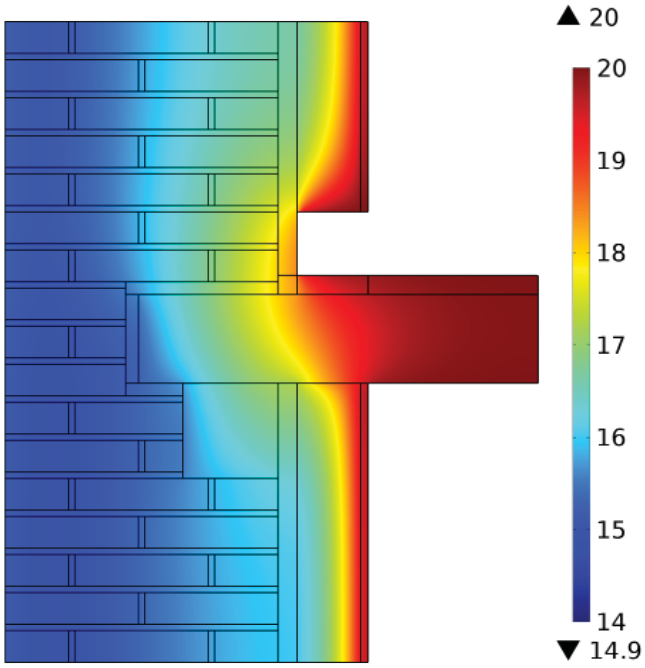

Figure 11.122 Temperature of an insulated wall with EPS, active heating and a museum indoor climate, at the 25th of July 2012 during a rain event.

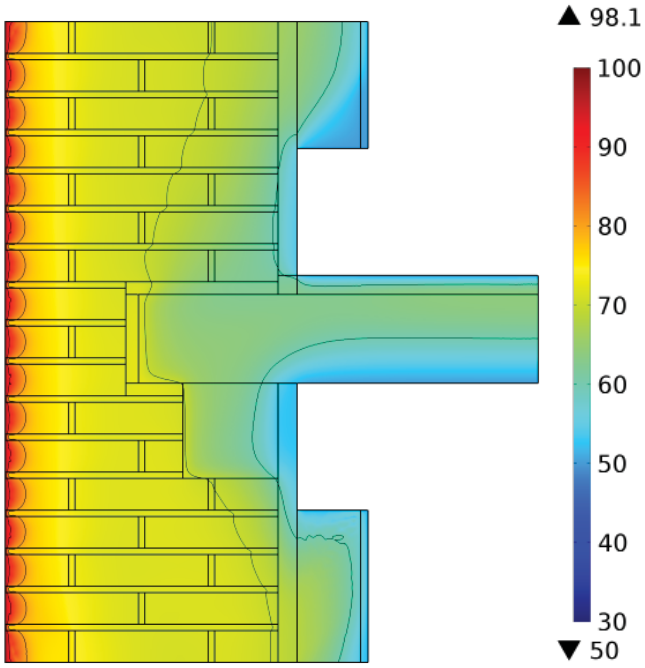

Figure 11.123 Relative humidity of an insulated wall with EPS, a 200mm insulation gap around the wooden beam, and a museum indoor climate, at the 25th of July 2012 during a rain event. Each contour line represents a difference of 10%.

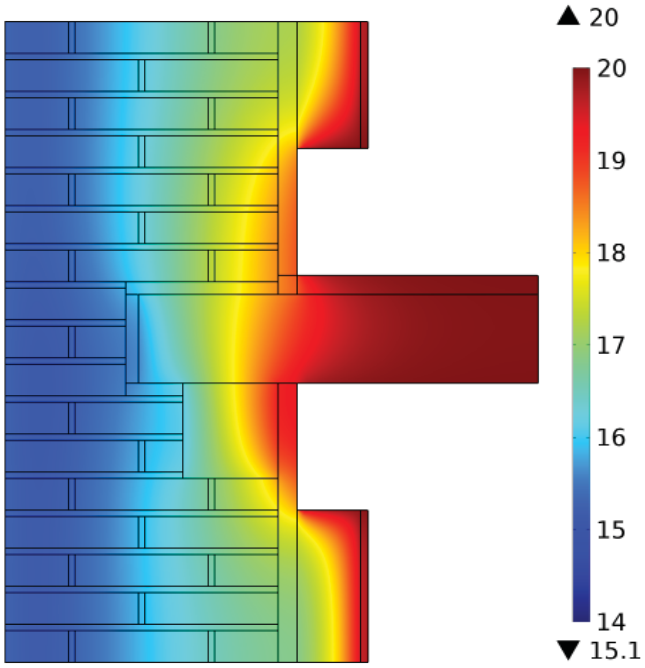

Figure 11.124 Temperature of an insulated wall with EPS, a 200mm insulation gap around the wooden beam and a museum indoor climate, at the 25th of July 2012 during a rain event.